PRECISION ENGINEERING CENTER

2006 INTERIM REPORT
September 2006

Sponsors:

3M Corporation
Electro-Optics Center at Pennsylvania State University
Lexmark International, Inc.
Missile Defense Agency
National Science Foundation
Optical Research Associates
Sandia National Laboratory
Vistakon, Johnson & Johnson Vision Care Inc.

Faculty:

Thomas Dow, Editor
Greg Buckner
Jeffrey Eischen
Dieter Grifis
Paul Ro
Ronald Scattergood
David Youden

Graduate Students:

Qunyi Chen
David Brehl
Karalyn Folkert
Timothy Kennedy
D. Lucas Lamonds
Arun Veeramani
Nadim Wanna
Robert Woodside
Yanbo Yin

Staff:

Kenneth Garrard
Karl Falter
Donna Irwin
Alexander Sohn

TABLE OF CONTENTS

1 DESIGN TOOLS FOR FREEFORM OPTICS

Kenneth Garrard
Precision Engineering Center Staff

1.1 INTRODUCTION

Software tools for the efficient design, fabrication and metrology of freeform optics have been constructed. Last year a project with Optical Research Associates integrated both a freeform fabrication cost metric and a fabrication error simulation into CODE V [1]. Recent work has concentrated on four additional areas: surface tolerance specification, analysis of surface metrology data, enhancements to the ASG 2500 DTM control system and a comprehensive solution to the motion planning problem for non-rotationally symmetric (NRS) surfaces. The first three of these are discussed in detail in [2]. NRS motion planning is the subject of the remainder of this report.

1.2 NRS MOTION PLANNING

A new technique has been developed for fabrication of non-rotationally symmetric or freeform optical surfaces on a diamond turning machine. This technique involves mounting a mirror blank on-axis and programming the DTM to follow a best-fit rotationally symmetric (RS) cross-section (spherical, conic or aspheric) while an auxiliary axis such as a fast tool servo (FTS) rapidly moves the tool to alter the shape of the resulting surface. By synchronizing the axes, spindle and FTS motions the desired non-rotationally symmetric surface is efficiently produced.

Surfaces of revolution are succinctly represented as a two dimensional cross sectional path in any plane that includes the axis of rotation. These representations include RS-274 G-codes, functional representations in Cartesian or polar coordinates and parametric representations. Freeform surfaces and symmetric surfaces rotated about a machine axis that is not coincident with their axis of symmetry (e.g., an off-axis conic segment rotated about the center of its aperture) require a complete three dimensional description rather than a cross-sectional path.

In the past, freeform surfaces were dealt with on an ad hoc basis and a specific solution was produced for each machining operation that depended on a variety of parameters such as the part fixture and part location on the fixture; machine geometry; tool geometry; fast axis orientation, bandwidth and range; and the original specification of the surface to be produced as illustrated in Figure 1 with an off-axis biconic mirror. Currently there is no standard way to decompose an

arbitrary freeform surface into motion commands for the axes of a machining center. The surface may be expressed as an explicit or implicit 3D function in one of several coordinate systems or as a collection of vectors (i.e., data points and direction cosines). It is apparent that any of the functional forms can be used to generate such a point cloud in any coordinate system desired and at the density necessary to accurately represent the surface.

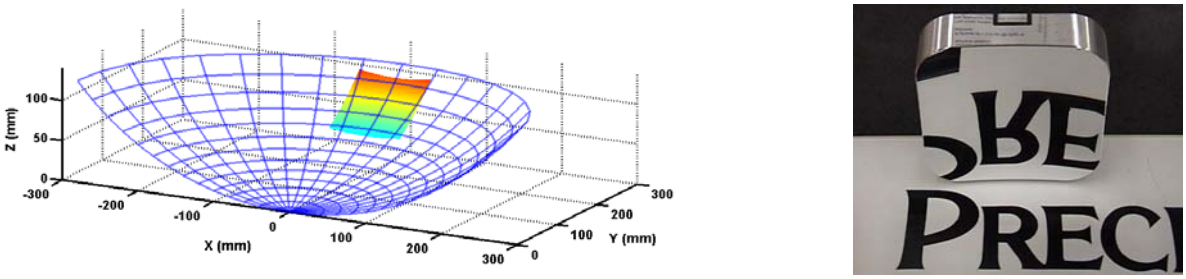

a) Off-axis biconic mirror segment

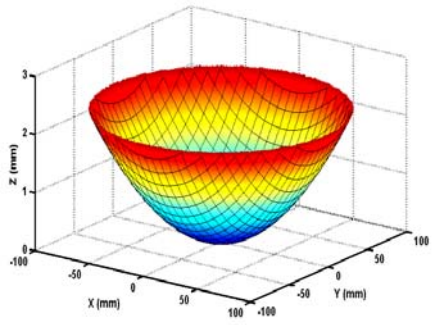

b) Rotationally symmetric component of mirror

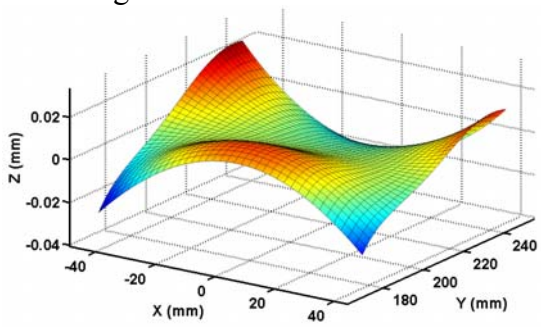

c) NRS component of the mirror

Figure 1. Decomposition of a biconic mirror surface (a) into symmetric (b) and non-symmetric (c) components for on-axis fabrication.

Motion planning for fabrication of a freeform or non-rotationally symmetric surface with diamond turning consists of four steps. Each of these steps is discussed in the following sections.

1) Decomposition of the surface shape into rotationally symmetric (X, Z DTM axes) and non-rotationally symmetric (FTS) components.
2) Description of the RS and NRS motion paths. This could be a functional description, but a 3D sag table over a polar grid (R,θ,z) is needed for the NRS path and 2D half-meridian cross-section (R,z) RS path is needed.
3) Compensation of the motion commands for the tool shape and radius.
4) Deconvolution of the NRS tool path to pre-compensate FTS actuator dynamics.

1.2.1 DECOMPOSITION OF FREEFORM SURFACES

Off-axis Conics

An analytic solution for the optimal decomposition of an off-axis segment of a conic surface into a rotationally symmetric component and a non-rotationally symmetric residual was developed for the Oak Ridge Y-12 Optics Modil in the early 1990s [3]. The algorithm was optimized for execution speed and coded in C for real-time generation of the command signals needed to drive a diamond turning machine and a fast tool servo to fabricate an NRS optical surface. The result is a functional description of the conic surface translated on axis and tilted, along with coefficients to a radial polynomial that is the "best-fit" asphere minimizing the NRS sag.

The NRS component is the difference between this function and the asphere. A C decomposition program, **nrsgen**, creates a sag table for the entire surface, the asphere or the NRS component over the specified aperture in either cylindrical or Cartesian coordinates. The aperture can be circular or square and the distribution of data points over the aperture can be evenly spaced in X and Y (plaid), spaced at equal angles on concentric radii (polar) or at equal angles and linearly decreasing radii (spiral). This program can be used to generate sag tables describing mirror surfaces for non-rotationally symmetric machining. Table 1 shows the decomposition parameters and results for the off-axis conic three mirror anastigmat (TMA) described in [2]. Note that the best-fit asphere is almost a parabola for all three mirrors (i.e., the quadratic radial coefficient, A2, is at least five orders of magnitude larger than the other coefficients). The NRS shape is described in cylindrical coordinates by substituting the NRS coefficients from Table 1 into Equation (1).

$$z(\rho,\theta)_{NRS} = d_1 + d_2\rho\cos(\theta) - \sqrt{d_3 + d_4\rho\cos(\theta) + d_5\rho^2 + d_6\cos^2(\theta)} \quad (1)$$

The difference between Equation (1) and the best-fit asphere is the required fast tool servo motion for any given ρ and θ. The asphere error values in Table 1 give an estimate of the maximum sag difference between the true best-fit asphere and the surface generated by connecting the points of the asphere grid sag table with straight lines. It can be used as a guide to generating a table dense enough to meet error tolerances. The table was generated using a 400 x 400 square grid enclosing the circular aperture of each mirror.

The shapes of the NRS components of the primary (M1) and secondary (M2) are shown in Figure 2 (the tertiary (M3) is similar to M1 with 1/8 the sag). For all three mirrors the FTS will reverse directions twice per spindle revolution. The maximum velocity of the Variform FTS is 140 mm/sec. By calculating the maximum slope in the circumferential direction along each

surface and dividing these quantities into 140, the maximum rotational speed for machining can be determined. For all three mirrors the slopes are less than 2 mm/sec. So the Variform velocity limit is not reached until the spindle speed exceeds 4200 rpm (140/2*60), which is more than twice as fast as the maximum ASG 2500 spindle speed.

Table 1. Off-axis conic TMA decomposition.

	Off-Axis Conic TMA		
	M1	**M2**	**M3**
R (1/curvature)	-1000.000000	-587.151127	-939.432788
K (conic constant)	-1.754657	-5.801289	-5.197043
Aperture Radius	70.000000	38.500000	35.000000
Decenter (Y)	220.242790	105.991898	79.181555
NRS Sag	0.186543	0.183477	0.023528
Tilt (YZ)	0.212285	-0.164886	0.082592
Decenter (Z)	24.035459	-9.219260	3.312460
Asphere Sag	2.350159	-1.152737	0.639387
Asphere Error	0.000004	0.000002	0.000001
Asphere Coefficients			
A2	4.800E-04	-7.809E-04	5.227E-04
A4	-7.484E-11	2.212E-09	-5.942E-10
A6	2.334E-17	-1.253E-14	1.351E-15
A8 (A10 to A16 omitted)	-9.097E-24	8.877E-20	-3.841E-21
NRS Coefficients			
D1	-1.539E+03	1.378E+02	-2.299E+02
D2	-5.340E-01	2.022E-01	-1.027E-01
D3	2.369E+06	1.900E+04	5.284E+04
D4	1.646E+03	5.614E+01	4.733E+01
D5	1.478E+00	2.153E-01	2.403E-01
D6	1.701E-01	7.244E-03	2.042E-03

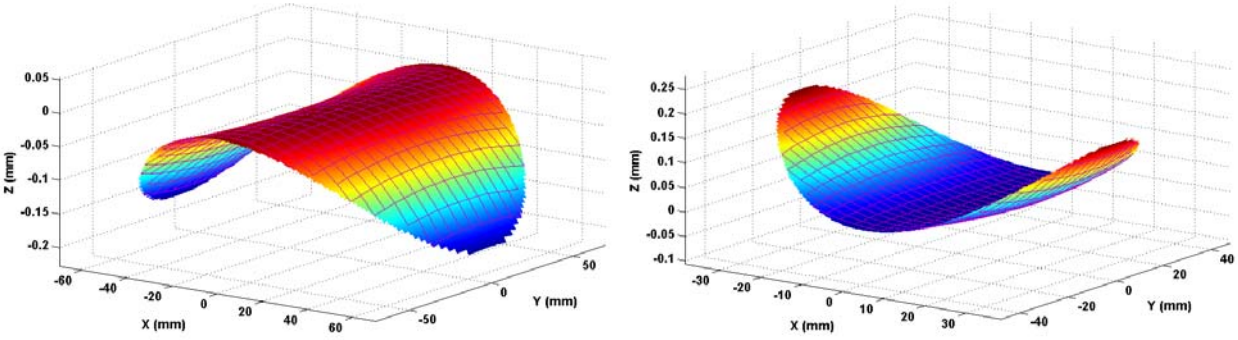

Figure 2. NRS component of off-axis conic TMA mirrors M1 (left) and M2 (right).

On-axis Zernike Polynomials

An on-axis Zernike polynomial TMA, also described in [2] was analyzed using two methods. Examination of the fabrication table output of CODE V revealed a maximum sag difference from a base radius sphere and for each mirror surface of no more than 184 μm. One option would be to machine this base radius sphere into each mirror while simultaneously moving the FTS to

make up the sag difference. However smaller servo excursions generally produce better surface finishes so the mirror shapes were studied in more detail. The shape and location parameters of the three mirrors are given in Table 2. Each mirror is a hyperboloid deformed by Zernike coefficients 4 through 26. The "Tilt (YZ)" angle specifies the pointing angle of the normal vector from the vertex of each mirror surface in the YZ plane.

Table 2. Zernike polynomial TMA decomposition.

	Zernike Polynomial [ORA]		
	M1	**M2**	**M3**
R (1/curvature)	-946.952538	-489.108365	-875.359850
K (conic constant)	-1.679276	-5.703053	-3.850754
Aperture Radius	72.510880	32.581828	34.824238
Decenter (Y)	121.059700	145.843230	225.663140
Zernike Coefficients			
Z4 (Z1=Z2=Z3=0)	-1.065E-005	-1.323E-005	8.162E-006
Z5	8.564E-007	-8.314E-005	-6.505E-005
Z6	1.087E-008	5.704E-008	-1.152E-008
Z7	-4.661E-012	-8.385E-011	-4.515E-011
Z8	-1.244E-012	-1.742E-011	2.274E-012
Z9	4.151E-008	2.352E-007	-3.270E-008
Z10 (Z11 to Z26 omitted)	-7.659E-009	-1.696E-007	-7.481E-008
NRS Sag	0.152000	0.184000	0.164000
Tilt (YZ)	0.221632	-0.266386	0.177875
Sphere Radius	-946.952538	-489.108365	-875.359850
NRS Sag (optimized)	0.138000	0.048000	0.020000

Fitting an asphere (radial polynomial) to each surface reduces the NRS sag to a maximum of 138 µm for M1. Figures 3 and 4 show the NRS component remaining after removal of the best-fit asphere from each surface. Additional tilt of the mirrors may further reduce the NRS sag (especially for M2). This would change the mounting plane angle with respect to the optical housing by an equal amount.

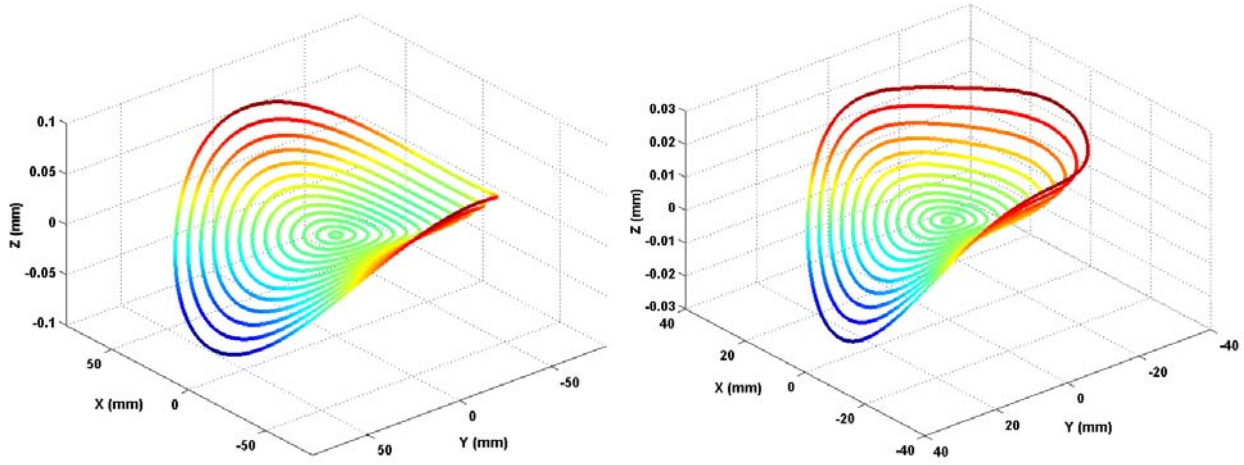

Figure 3. NRS component of Zernike polynomial TMA mirrors M1 (left) and M2 (right).

Generalized NRS Decomposition Algorithm

The technique used to generate the optimized NRS sag values for the Zernike polynomial TMA mirrors by fitting an asphere is quite simple and can be applied to any surface described by a function or a grid sag table that is to be machined about the center of its aperture.

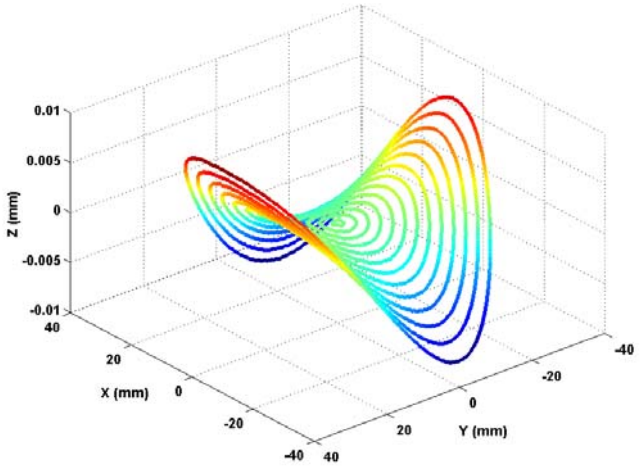

Figure 4. NRS component of Zernike polynomial TMA mirror M3.

1) Generate sag values along concentric radii about the center of rotation either by direct evaluation of the surface function or interpolation of a sag table.
2) Fit a least squares plane to the sag data.
3) Rotate the data to remove this plane. Note the XY and YZ tilt angles of this plane for design of a mounting surface.
4) At each radius,
   a) Find the mean sag value.
   b) The "best-fit" asphere at this radius must pass through the mean sag.
   c) For each angular location at this radius, the residual sag is the NRS surface.

In this way, both the best-fit asphere (ρ,z) and the NRS surface (ρ,θ,z) can quickly be constructed point-by-point as a 1D table (step 4b) and a 2D table (step 4c), respectively. The procedure is optimal in that it minimizes the NRS sag. Steps 2 and 3 can be skipped if a compound tilt in the mounting surface is undesirable. A sphere instead of an asphere may be easily fit to the data so that the rough machined surfaces will be easier to evaluate. In this case a least squares sphere with its center constrained to lie along the spindle centerline is fit to the 3D sag table data. It is also possible to fit a circle to the (ρ,z) columns of the 3D sag table (ignoring θ). If the circle center is constrained to the spindle centerline the results will be identical to the spherical fit. All three methods have been coded in Matlab. If the sag table is arranged such that each row is a concentric ring (or equivalently each column is a meridian), then the asphere fit and tool radius compensation operations described below can be fully vectorized in Matlab.

1.2.2 Real-time Motion Path

The rotationally symmetric component of the surface is described to the DTM controller as a (ρ,z) toolpath, usually from the edge of the part to the center for on-axis turning of a circular aperture. The exact command format depends on the controller, but usually follows the RS-274

G-code format. For an asphere the path consists of closely spaced points and an interpolation method for moving between points. The **nrsgen** program or the point-by-point algorithm discussed above can be used to generate the asphere and estimate the error due to linear interpolation, which should yield a worst case result.

To find the FTS locations at each point on the mirror surface during machining a bilinear interpolation algorithm over a grid of (ρ,θ,z) machine axis locations is used. The interpolation is expressed in polar coordinates since the DTM cross-feed axis (X) and spindle (θ) define a cylindrical coordinate system. The interpolation table is easily managed by the FTS control system and can yield a toolpath with residual errors smaller than the positioning accuracy of the actuator if the tabulated values are closely spaced relative to the surface curvature. The basic idea of multi-dimensional interpolation is to find the neighborhood of an un-tabulated value in the table and construct a weighted average of the values of nearby points as an estimate of the unknown value. For a two dimensional table, there are four nearest points to consider. A linear estimator uses the product of the distance ratios from the un-tabulated point to the grid lines intersecting each neighbor point in each dimension as the weighting factor for that tabulated neighbor point. Higher order estimators that use cubic functions, splines or a table of derivatives can produce smoother, more accurate interpolators; all at the cost of longer computation time and more memory.

1.2.3 TOOL RADIUS COMPENSATION

Since the tool has a finite shape (usually a circular radius) in the XZ plane of motion, the contact point between the tool edge and the work surface changes as a function of the slope of that surface. For RS machining with circular tools the required compensation is easily implemented by offsetting the tool path by the radius of the tool in a direction normal to the surface.

For example, a circular segment of a concave sphere of radius R_S can be machined with a tool of radius R_T by moving the tool through a path from the edge to the center of the aperture along a circular path of radius $(R_S - R_T)$. For other shapes the change in slope is not constant, requiring computation of the gradient of the surface either analytically or numerically. For a surface normal angle, φ, measured with respect to a vector from the center to the apex of the tool the corrections are,

$$x_{delta} = R_T \sin(\varphi) \qquad \text{and} \qquad z_{delta} = R_T \cos(\varphi) \tag{2}$$

For a non-rotationally symmetric surface, the normal angle, φ, is dependent on both the radial and angular location of a point on the surface (i.e., the surface is three dimensional). Thus the

normal vector cannot be found from a single cross-section nor is the normal always in the plane of the cutting tool.

Normal Vectors

If the surface is described by parameters to a function (e.g., a biconic or polynomial expansion), then it may be convenient to generate tool radius compensation values analytically. For any continuous, differentiable surface a normal line is perpendicular to any two tangent lines that intersect at a right angle. In particular, the tangent lines that lie in the XZ and YZ planes define a plane tangent to the surface and can be used to find the normal at any point. A parametric expression for these two tangent lines and their cross product is easily expressed in Maple [4]. The orthographic projection of the normal vector from a point into the cutting plane (typically XZ) gives an expression for the tool center location that places the tool edge exactly tangent to the desired surface at that point. This operation is also easily expressed in Maple for an arbitrary continuous surface $F(x,y)$ if the partial derivatives $\partial F/\partial x$ and $\partial F/\partial y$ exist.

3D Radius Compensation

For tool radius compensation of an NRS surface, the normal vectors can be determined analytically or estimated numerically from a grid sag table, but they must be projected into the plane of the tool (XZ). The tool offsets for a given point are then the x and z components of that projected vector. If the radial spacing of the original tool path is to be retained, then the x correction must be zero and the z correction is adjusted proportional to the cosine of the projected normal vector.

The tool compensation procedure described is straightforward to implement with an algebraic programming language such as Maple, but is difficult to implement in a procedural programming language such as C or Matlab. As an alternative, consider the 3D radius compensation problem as a series of 2D problems; one for each angular position of the spindle. If the surface data is expressed in cylindrical coordinates, a collection of half-meridian paths (radial lines from edge to part center) can be individually corrected for tool radius giving a corrected path for each spindle angle. A complete cylindrical 3D grid sag table for the NRS surface can be built in this way with any angular resolution. This is equivalent to the vector projection technique discussed above but is much simpler to implement. For large apertures the number of meridians needed to adequately describe the surface may be large since the surface area represented by each point on an equiangular gird increases with radius. Matlab code has been developed that implements this 3D tool radius compensation algorithm. The half-meridians are extended a short distance past the center and outer edge of the aperture since slope estimation using finite differences is inaccurate at the endpoints of a curve. The redundant data points are discarded after compensation.

1.2.4 DECONVOLUTION OF ACTUATOR DYNAMICS

Synchronization between the DTM axes and the FTS is critical if the correct NRS shape is to be produced. While the machine axes follow a low frequency trajectory to create a rotationally symmetric (RS) component, the FTS moves at high temporal and spatial frequency to produce an NRS feature within one revolution of the part. An example is the fabrication of a toric lens, which has two different radii of curvature in orthogonal directions. There is an average radius that can be cut by the slow speed machine axes, but an FTS is needed to add features twice per revolution to create the smaller radius at one location and the larger radius 90 degrees later. The synchronized motions of the machine axes and the FTS combine to create the desired geometric surface. However, the dynamic behavior of the axes, particularly the FTS, can influence the commands, delaying the motion of the tool and creating errors in the resulting surface. The phase errors of the base machine axes can usually be ignored as the axis accelerations are moderate and velocity is low. However, even a small lag time associated with a FTS will result in poor form fidelity and improper placement of NRS surface features with respect to the base surface and any fiducials on the part. The errors caused by the FTS dynamics can be corrected if they are known, repeatable and used to modify the input command to the actuator.

Actuator Phase Lag

Figure 5 illustrates the delayed and attenuated response of the Variform FTS. In this example, the phase angle is less than one degree; however the effect of phase lag scales with radius and results in significant form error (6.28 mm at 600 rpm and 100 mm radius) unless the actuator is operated at a frequency substantially below its bandwidth (by a factor of 100 or at about 3 Hz).

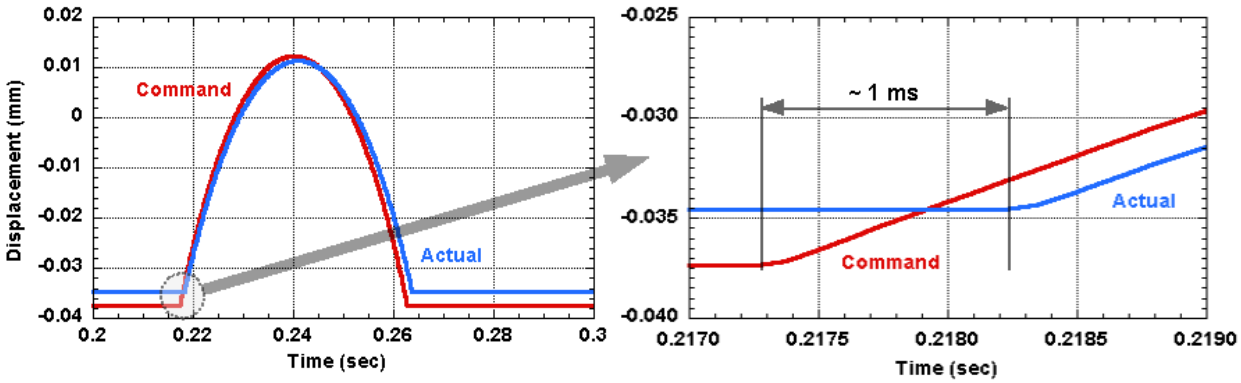

Figure 5. Response of the Variform to an input command. Actuator motion is delayed about 1 msec and attenuated by about 8%.

Convolution

The response of a dynamic system to an applied signal is a function of the frequency of that signal. In general, the response results in an attenuated and delayed motion of the output with respect to the input signal. When the system is a fast tool servo and the dynamic input signal is made up of a variety of frequencies, the result is form error in the machined surface. If the input contains multiple frequencies, the corresponding output can be determined using the *principle of superposition*; that is, the input signal can be uniquely decomposed into single-frequency components each of which will be individually attenuated and delayed.

The response of the system is the sum of these frequency components. To machine a desired surface profile with high fidelity, the amplitude attenuation and phase related delay must be eliminated. To achieve this, the input signals are modified prior to applying them to the system such that the attenuation is canceled and the phase is compensated. A technique for system identification and an input signal modification algorithm have been developed and applied to the Variform FTS to produce the desired output response for high frequency inputs [5].

Deconvolution

The effect of a dynamic system on an input signal of length N can be determined by applying the convolution operation to the input *x[n]* and the impulse response *h[n]* of the system. The convolution operation describes how a linear filter (an actuator) modifies a given input signal (command) to produce an output signal (motion). Each value in the convolved output signal *y[n]* can be calculated with the summation in Equation (3), where *M* is the length of the impulse response. The length of *y[n]* is *N+M-1*. Convolution is mathematically equivalent to polynomial multiplication and can be directly (and inefficiently) calculated from Equation (3) in the time domain. If the discretely sampled input and impulse response signals are transformed to the frequency domain, convolution becomes a straightforward element-by-element, complex multiplication of two vectors. The discrete Fourier transform (DFT) is commonly implemented by the fast Fourier transform (FFT) algorithm which exploits the symmetries in Equation (3) to accelerate this calculation. Equation (3) can thus be restated in the frequency domain using an FFT operator as shown in Equation (4). The inverse FFT operation can then be used to find *y[n]*.

$$y[k] = \sum_{m=0}^{M-1} h[m] \times x[k-m] \tag{3}$$

$$\mathbf{FFT}(x[n]) \times \mathbf{FFT}(h[n]) = \mathbf{FFT}(y[n]) \tag{4}$$

Deconvolution is the inverse of convolution and can thus be used to find *x[n]*, given an actuator impulse response *h[n]* and a desired motion $y_d[n]$. Rearranging Equation (4) gives Equation (5).

$$x[n] = \mathbf{FFT}^{-1}\left(\frac{\mathbf{FFT}(y_d[n])}{\mathbf{FFT}(h[n])}\right) \tag{5}$$

Application of the inverse FFT operation then yields a signal that should exactly counteract the actuator dynamics so that it follows the desired trajectory, eliminating steady-state following error. This technique critically depends on knowledge of the actuator dynamics as embodied in the impulse response and requires the complete desired motion profile.

Experimental Verification

The algorithm has been validated for the Variform FTS. The response of this actuator is predominately second order although nonlinearities are present for large amplitude command signals. Figure 6 shows the path error associated with a 160 μm command signal that is the sum of 100 Hz and 300 Hz sine waves. The response of the actuator to the 300 Hz sinusoid is 140 degrees out of phase and attenuated 2.5 dB resulting in a very large (200 μm PV) error. The deconvolution algorithm calculates a new command signal that effectively pre-compensates for these effects individually at each constituent frequency. The following (or tracking) error is reduced by about 3 orders of magnitude. The response shows virtually no delay from the desired excursion after a startup interval lasting approximately 4 ms. In practice, this startup period will occur before machining begins and thus will not affect the fidelity of a surface.

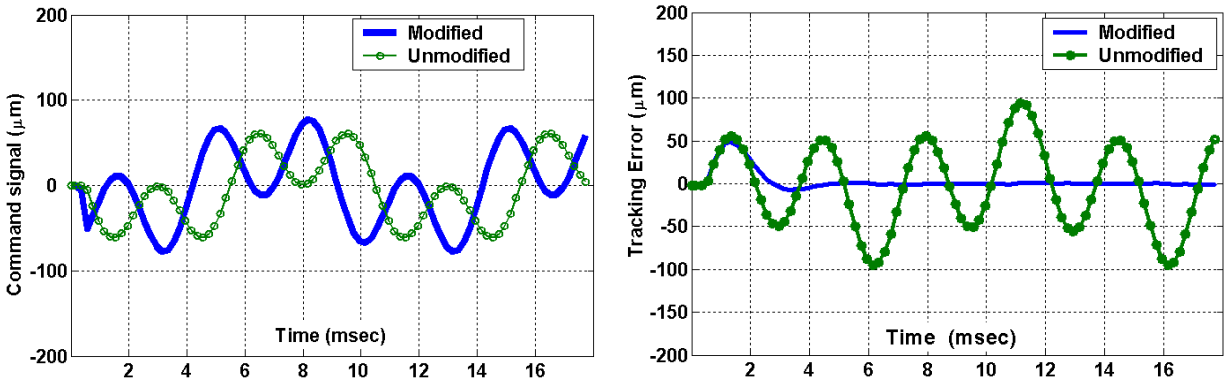

(a) Command signals (b) Acutator tracking error

Figure 6. Deconvolution experiment for a high frequency command signal.

Implementation

The deconvolution algorithm described by Equation (5) has been coded in Matlab and generalized for use with any surface described as a time-based path. A direct implementation of this equation encounters several obstacles. These include sampling frequency and sampling duration mismatch in $h[n]$ and $y_d[n]$, noise amplification by the vector division operation,

frequency bin leakage due to imperfect sampling of *h[n]* and computational round-off from the FFT operations. These problems were overcome with two innovations to the standard frequency domain deconvolution technique. First, by inverting *h[n]* and re-sampling the result so that its resolution and duration match $y_d[n]$ an overlap-add block convolution algorithm can be used. In other words, the deconvolution operation is replaced with convolution of the command signal with the inverse dynamic response of the actuator. It is also possible to measure the inverse dynamics directly with a spectrum analyzer by reversing the roles of the input (or excitation) signal and the output (or actuator response) signal. Frequency leakage from the dynamic response causes the inverse FFT to produce a complex result. Clearly the time-domain trajectory command sent to the actuator cannot be complex. Simply discarding the imaginary part of each value or taking the absolute value is incorrect. The second innovation was the implementation of an inverse FFT algorithm that always returns a correct real result.

To pre-compensate a fast tool servo shape for diamond turning, the spindle speed must be selected so that a time-based spiral path can be generated that represents the FTS actuator motion. Then deconvolution in the frequency domain can generate a compensated tool path (also a spiral). Finally the spiral data can be transformed back into the time domain and overlaid into a polar grid for the FTS controller bilinear interpolation routine. This process has been automated for several types of freeform surface descriptions including those described in this report.

1.3 CONCLUSIONS AND FUTURE WORK

Matlab codes have been developed for the decomposition of an arbitrary surface into RS and NRS motion paths for fabrication via diamond turning. The RS motion path is in the form of a 2D point-to-point asphere, the coefficients of a best fit radial polynomial or a circular cross-section. The NRS motion path is a 3D cylindrical coordinate lookup table or the coefficients of a functional representation in the case of off-axis conics. A general purpose tool shape compensation algorithm for NRS surfaces has also been developed. These new functions produce output data files that are easily exported to the DTM controller (RS), the PEC deconvolution software (NRS) and the FTS controller.

Presently, the decomposition and tool shape compensation code assumes that the part will be machined with the spindle axis aligned with the z axis of the defining coordinate system. That is, the aperture is centered on the spindle and the workpiece tilted in the XZ plane. Future work will remove this limitation and allow rotation about any axis including one that may not intersect the aperture. The objective is to automatically find the optimal location and direction for the axis of rotation vector.

REFERENCES

1. K. Garrard, T. Bruegge, J. Hoffman, T. Dow and A. Sohn. Design tools for freeform optics. SPIE 5874, 95-105, (2005).
2. T. Dow, K. Garrard, A. Sohn, Final Report to the Navy ElectroOptics Center on FOCUS, Freeform Optics Center of the US, (2006).
3. W.D. Allen, R.J. Fornaro, K.P. Garrard, L.W. Taylor. A High Performance Embedded Machine Tool Controller, Microprocessors and Microprogramming, 40, 179-191, (1994).
4. K. Garrard and A. Sohn. Off-axis biconic mirror fabrication. Precision Engineering Center Annual Report, 20, 263-286, (2002).
5. W. Panusittikorn. Error Compensation Using Inverse Actuator Dynamics. PhD Dissertation, North Carolina State University, (2004).

This page intentionally left blank.

2 DESIGN OF REFLECTIVE TMA

Nadim Wanna
Graduate Student
Thomas Dow
Professor
Department of Mechanical and Aerospace Engineering

2.1 INTRODUCTION

Typical defense optical systems use reflective optical components to image light onto a detector for remote surveillance, airborne and missile systems. Three Mirror Anastigmat (TMA) has an advantage over two mirror systems, since the third mirror can be used to correct for aberrations at the image plane. Current optical systems use combinations of on-axis and off-axis segments of rotationally symmetric aspheres. Rotationally symmetric conic surfaces are common, but more degrees of freedom are necessary to meet challenging performance and packaging requirements.

Non-rotationally symmetric surfaces, or freeform surfaces, open a new window for optical design by adding degrees of freedom to the optical surface that can correct optical errors. This capability is important for optical systems with tilted and decentered components. In this case, to avoid optical aberrations at off-axis field angles locally anamorphic surface shapes that have different local base radii of curvature in the orthogonal directions [1].

2.2 OPTICAL DESIGN

Three Mirror Anastigmat (TMA) optical design is an f/6.139 with an unobstructed entrance pupil diameter of 140 mm, a 1° circular field of view, and an effective focal length of 859.5 mm. These specifications similar the 150 mm two mirror telescope designed and built at the PEC [2], except for the field of view and effective focal length. Entrance Pupil Diameter (EPD) or primary mirror aperture diameter is reduced due to the available aperture on the laser interferometer available at the PEC. The interferometer can accommodate parts with 150 mm aperture diameter. Ability to measure fiducial as well as optical surfaces is important and led to changing the EPD to accommodate for a 10 mm fiducial ring. Changing the EPD and keeping the effective focal length constant changes the f-number from 5.73 to 6.139.

2.2.1 SIZE AND SHAPE

An alternative design to the off-axis conic is a three mirror anastigmat using Zernike polynomial freeform surfaces is shown in Figure 1. The optical surfaces in this design are converted to on-axis Zernike polynomial surface types. This design maintains the f-number, field of view, entrance pupil diameter, and focal length of an off-axis conic TMA design. The off-axis conic design is an improvement from the two mirror telescope and is used as a baseline for the on-axis Zernike polynomial design [3].

Using the TMA off-axis conic design as a baseline, surface properties of the three mirrors are changed from conical surfaces to Zernike polynomials keeping the same radius of curvatures and conic constant values. Zernike polynomial coefficients, 4^{th} to 26^{th} terms, are allowed to vary in the optimization without changing their initial values. Primary and secondary mirror radius of curvature is set as variable, while the tertiary mirror's radius of curvature is solved for by paraxial marginal exit angle.

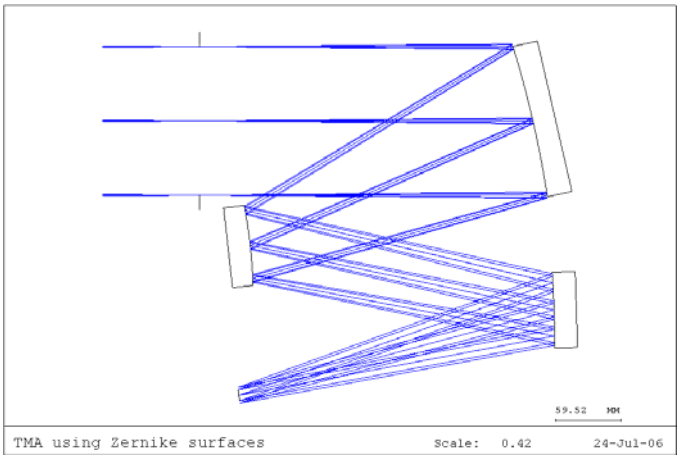

Figure 1. TMA using on-axis Zernike surfaces

To realize an unobstructed telescope design, the mirrors are tilted about the optical axis. Components are tilted about the optical axis, and then the new optical axis follows the chief ray or normal [4]. Positive α-tilt is rotation about the x-axis in the counter-clockwise direction. First, the primary mirror is tilted by 12.7°, placing the secondary mirror below the entrance pupil. Next, the secondary mirror is titled by -15.3°, placing the tertiary mirror below the primary mirror. Finally, the tertiary mirror is tilted by 10.2°, placing the image below the secondary mirror. The image plane α-tilt is varied to accommodate for errors in the optimization. Distance between primary-secondary and secondary-tertiary mirrors is set to 280 mm. Distance between tertiary mirror and image is varied.

2.2.2 OPTIMIZATION

The starting point of any optical design is to set the design goals and initial specifications before running an optimization routine that leads to a finalized system. Using the enhanced off-axis conic TMA described above as a baseline for optimization of the Zernike polynomial TMA. Of the four error function types provided by Code V for optimization, wavefront error variance is chosen since the system will be measured using dual pass interferometry.

Initially, the system is optimized by minimizing the wavefront error and geometrically constraining the vertical distance between the secondary mirror and the entrance pupil diameter to be at least 10 mm. Field map option, in Code V, is used to evaluate the system at the image plane. The wavefront polynomial fit for spherical aberration displays the node located on the horizontal axis. The fit for coma has a node located below the axis at (-0.1°, 0.2°) field angle. Polynomial fit for astigmatism displays two nodes, as proven by Thompson [5], for non-rotationally symmetric systems. The two nodes are in the field of view and are located on the horizontal axis at (±0.2°, 0°). To minimize these optical aberrations thus wavefront error, further optimization is executed with added constraints to the system.

More constrains are added to the optimization routine to further improve the performance of the TMA. To minimize the coma and spherical aberration over the field of view, the coma node is constraint to be at the origin of the circular field of view. This automatically constrains the spherical aberration node to be at the center of field also. Astigmatic nodes are shifted from their original place to (±0.35°, 0°) on the horizontal axis, minimizing astigmatism over the circular field of view. After the optimization routine is executed, the wavefront error is further minimized with the optical aberration nodes of interest at the locations specified.

Optical specifications of the system are tabulated in Table 1. Zernike mirror surfaces are defined as base conics deformed by Zernike coefficients 4 through 26. Primary and secondary mirror surfaces are hyperboloids while the tertiary mirror surface is an ellipsoid. Distance between tertiary mirror and on-axis focus at the image plane is 294.453 mm. The best focus of the system is 0.143 mm in a direction away from the tertiary mirror. The mirror tilts are also shown, the image is tilted by -9.574° to compensate for optical aberrations, placing the detector at an angle with respect to the vertical y-axis.

Table 1. TMA optical system specifications

	Radius of curvature (mm)	**Conic Constant**	**Aperture Diameter (mm)**	**Distance to next surface (mm)**	**α-tilt (°)**
Primary	-1003.328	-1.613	140	280	12.374
Secondary	-556.276	-5.769	72	280	-18.646
Tertiary	-865.999	1.399	68	294.453	14.184

The on-axis Zernike polynomial TMA mirrors are analyzed using the fabrication table output of Code V. The data output reveals a maximum sag difference from a base radius sphere. The machining process of the mirrors would be to machine this base radius sphere into each mirror

while simultaneously moving the FTS to make up the sag difference. Primary and secondary mirrors are hyperboloids while the tertiary mirror is an oblate ellipsoid deformed by Zernike coefficients 4 through 26. The tilt angle specifies the pointing angle of the normal vector from the vertex of each mirror surface in the YZ plane. Fitting a sphere to each surface reduces the NRS sag to a maximum of 109.9 μm for M2, with 84 μm for M1 and 41 μm for M3. Additional tilt of the mirrors may further reduce the NRS sag. This would change the mounting plane angle with respect to the optical housing by an equal amount.

2.2.3 THEORETICAL PERFORMANCE

After the optimization, the TMA system was evaluated in Code V to predict theoretical performance of the telescope. Helium-Neon light (λ = 632.8 nm) was used for analysis. Performance, compared to the off-axis conic system, shows at least twenty one times improvement.

Wavefront Error

Wavefront error plot for Zernike polynomial TMA over the full field of view, shown in Figure 2, gives the best description of the performance of the system. Wavefront error is a combination of the errors that accumulate through the system, shown at the image plane. Minimum error is 0.003 waves placed at (±0.4°, 0°) near the location of astigmatic nodes. Error increases from these points inward, towards the center of the field, and outwards away from both field points. The error at the worst point in the field is 0.011 waves at the center of the field, with an average of 0.0063 waves over the field of view. The average error is 21 times smaller than the off-axis conic TMA design.

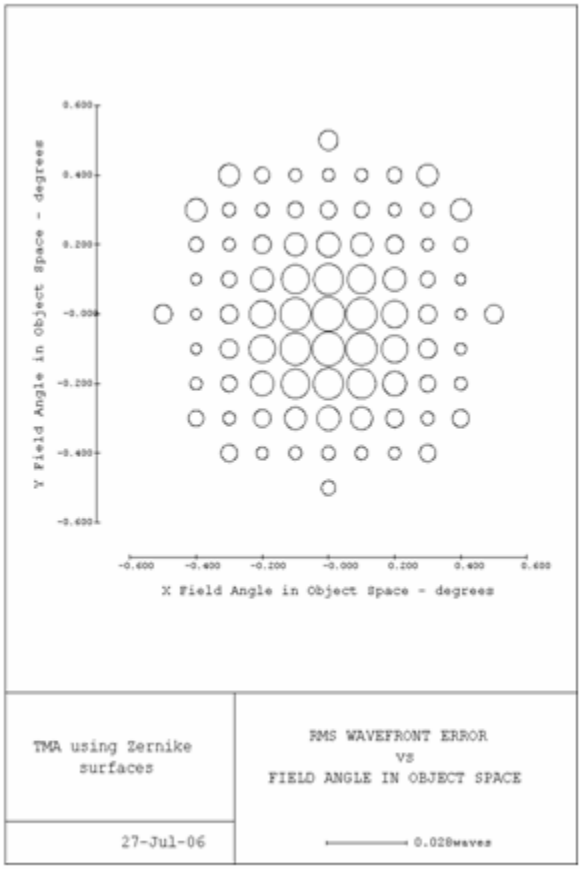

Figure 2: RMS wavefront error for Zernike TMA across the field of view

Modulation Transfer Function

The on-axis Zernike polynomial system MTF plot is shown in Figure 3. Performance is essentially perfect, even at the worst location in the field it is diffraction limited. At 50% modulation, system frequency varies between 99 – 104 cycles/mm. At the detector's Nyquist frequency or 68 cycles/mm, modulation varies from 0.68 to 0.69.

Compared to the off-axis conic system, the on-axis Zernike MTF shows an impressive improvement in overall system performance.

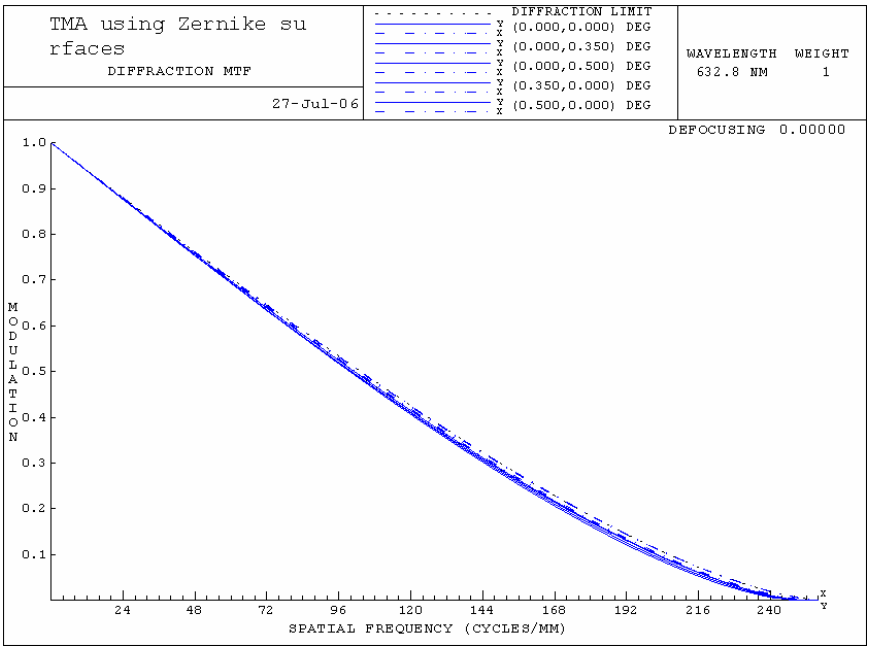

Figure 3. MTF for the on-axis Zernike polynomial TMA

2.3 OPTO-MECHANICAL DESIGN

The opto-mechanical design concept for the three mirror telescope is "bolt and go" with diamond machined optical and fiducial surfaces. The opto-mechanical design specifications are based a missile application and must withstand vibration and high acceleration loading. The goal is to package the optical elements such that the appropriate degrees of freedom are constrained but the elements are not over constrained and thus prone to distortion. The following section addresses the issues of material, fiducial surface, mounting features and telescope frame design.

2.3.1 MATERIAL

Components of the TMA system are to be machined from aluminum 6061-T6 alloys. This material presents a balanced compromise between material strength necessary for structural rigidity and material properties to create surface finishes adequate for infrared imaging. Optical and fiducial surfaces are machined utilizing diamond turning process capable of producing high fidelity optical surfaces in many non-ferrous materials. The potential surface finish of 6061 aluminum is not as good as plated surfaces but is sufficient for the infrared needs of this telescope. Fabrication of mirrors and telescope housing frame from 6061-T6 aluminum allows

system expansion and contraction proportionally with a temperature gradient. Thus, the system is unaffected due to any thermal instability.

2.3.2 MIRROR STRUCTURE

Lightweight Design

The design of the mirror structure is crucial in achieving a bolt-and-go telescope. The three mirrors are designed to integrate the same fiducial and mounting features. Minimum thickness of each mirror structure is based on the aspect ratio; that is, the ratio of the mirror diameter to the thickness. Distortions of the optical surfaces can occur when the part is mounted on the vacuum chuck for machining. An aspect ratio between 3 and 4 provides minimal distortion values.

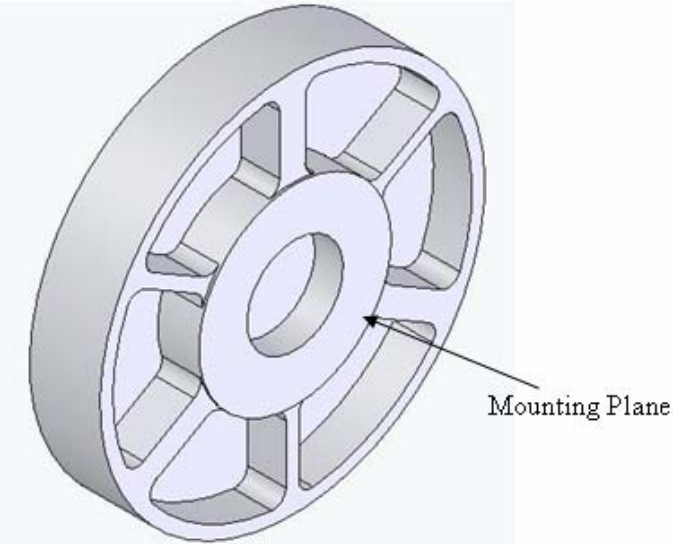

Figure 4. Lightweight primary mirror

Figure 4 shows the primary mirror structural design. Utilizing part of the aperture to mount the structure onto the vacuum chuck reduces the aspect ratio from 6 to 3 for a 25 mm thick part. The mounting plane, shown in Figure 4, has a 75 mm aperture diameter. Then, the rest of the aperture is light-weighted to reduce the part mass and deflection. The inner mounting plane and the outside ring are attached with ribs. Inside of the mounting plane is also machined for further mass reduction. The mass of the primary mirror is reduced from 1.27 kg to 0.85 kg, or 33 percent weigh reduction. Cutting force, a maximum of 10 N, and vacuum pressure, 10 psi, is modeled in SolidWorks/Cosmos and result in optical surface deflection less than 80 nm.

Fiducialization Technique

For the optical design of the TMA using Zernike polynomial surfaces described in the previous section, the optical axis of each mirror is normal to the surface along the z-direction shown in Figure 5. The fiducial ring creates a plane that mates to the plane created on the telescope housing through contact with three pads. The fiducial plane will constrain the optical component in three degrees of freedom but will allow translation in the x and y directions and rotation about the z-axis. These degrees of freedom are constrained by the pair of pins protruding from the fiducial plane on the mirror that mate with a hole and a slot in the housing. Orientation of each

optical surface depends on the orientation of the fiducial plane on the housing and the location of the hole and slot in the contact pads.

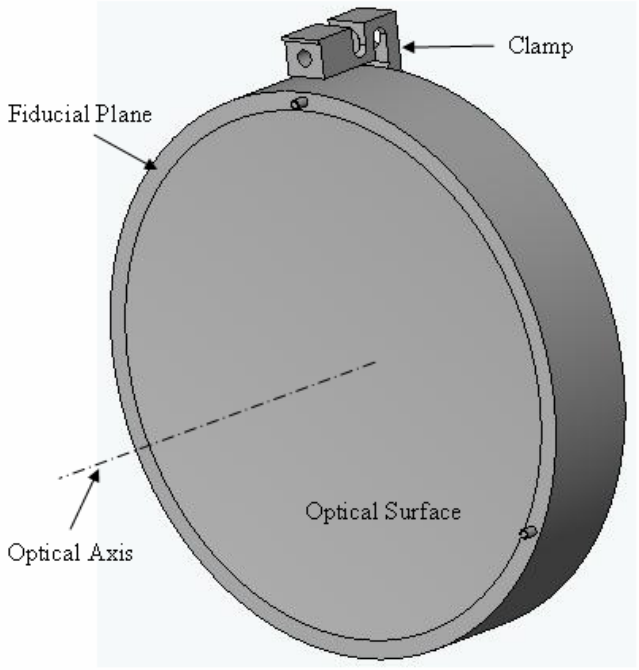

Figure 5. Mirror structure with pins in the fiducial plane and mounting clamp

Mounting Features

The mirrors will be located on the telescope housing frame using the locational fiducials. Each mirror is held in place using three clamps to minimize optical surface distortions, shown in Figure 5. Clamps, shown in Figure 6, apply mounting force along the three fiducial contact lengths. Application of clamping force collinear to the fiducial contact eliminates the moment force created from displacement between the two forces. Sustaining ten times gravitational loading is required from clamping force, which differs for each mirror depending on its weight. Simulating the effects of the clamping forces on the optical surfaces using SolidWorks/Cosmos shows less than 100 nm optical surface deflection.

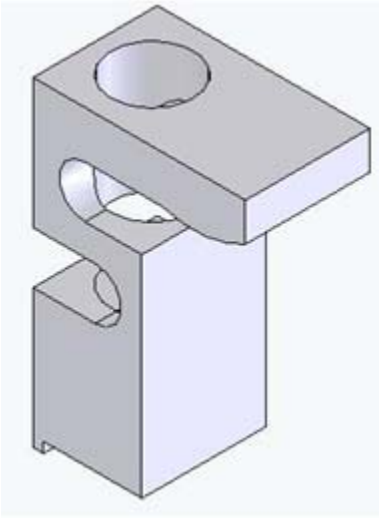

Figure 6. Clamp used to hold mirror in place

2.3.3 TELESCOPE FRAME

The telescope housing frame creates the global coordinate system used to locate each mirror in space and thus locate each mirror with respect to each other and the detector. The frame is a lightweight aluminum structure with mounting surfaces for the three mirrors and the detector. The design for the telescope housing frame with overall dimensions (mm) is shown in Figure 7.

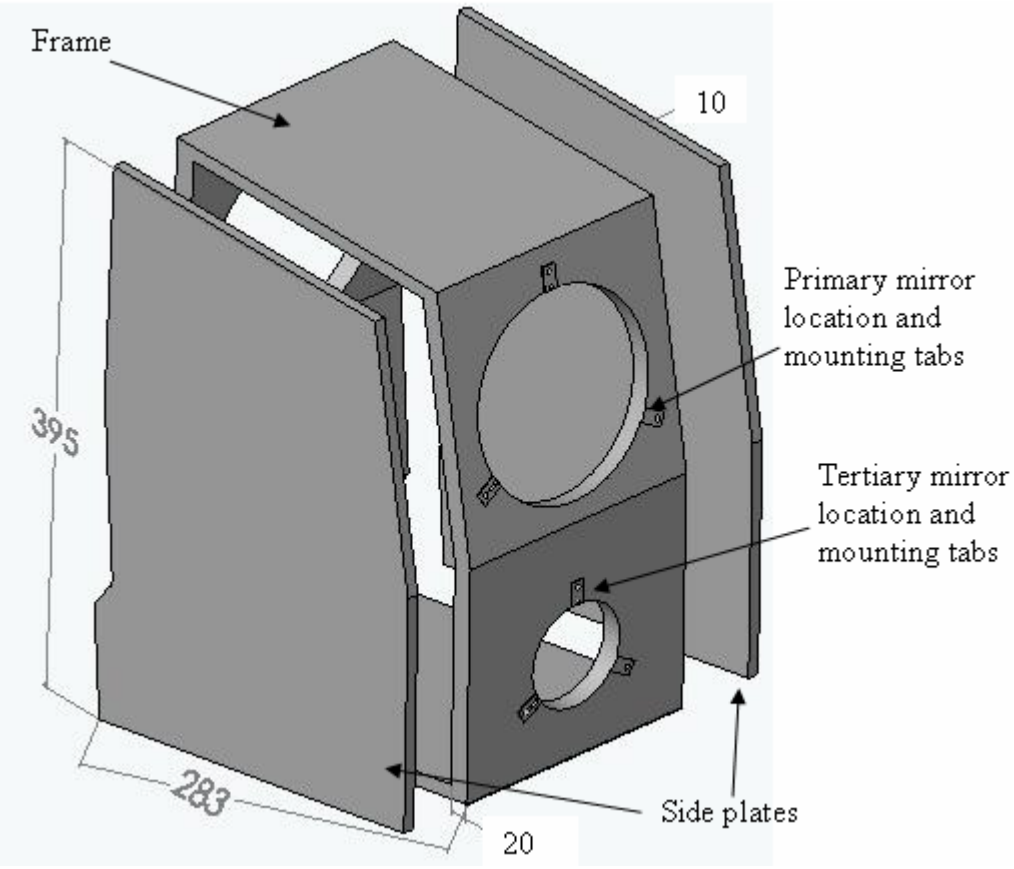

Figure 7. Telescope housing frame for the TMA

The depth of the frame is 196 mm with 10 mm thick side plates bolted on both sides. The wall thickness of the mirror mounting planes is at least 20 mm while the supporting sides are 10 mm thick. The frame is modeled in SolidWorks/Cosmos to optimize the wall thickness. Initial values of wall thickness are chosen and through various iterations optimal results that minimize the distortion of the frame to below 1 μm is achieved.

The frame is machined from a solid aluminum block using wire EDM. Then, two side plates are pinned and bolted onto the base frame. The overall weight of the structure is 8 kg, including the frame and side plates. Mirror mounting pads incorporate tilt angles with respect to the image

plane. The mirror mounting surfaces consist of a plane with a hole and slot to sufficiently constrain the location of each mirror, described earlier. Three threaded mounting holes in each plane are used to hold the mirror in position.

2.4 CONCLUSIONS AND FUTURE WORK

Rotationally symmetric and three mirror anastigmat optical systems using a combination of on and off-axis rotationally symmetric surfaces suffer from optical aberrations that affect the image quality. An unobstructed three mirror telescope has been designed using non-rotationally symmetric or freeform surfaces. Addition of a third mirror to two mirror optical systems and optical surface variables reduces optical aberrations and improves the image quality. The opto-mechanical design of the TMA utilizes conventional fiducialization technique for location and clamps for mounting to minimize optical distortions. Further research includes fabrication and testing of the optical system, and performance testing under high gravitational loading required during launch.

REFERENCES

1. Rogers, M. and Thompson, K. Benefits of Freeform Mirror Surfaces in Optical Design. Proceedings of the ASPE Winter Tropical Meeting on Freeform Optics, Chapel Hill, NC, 73-79, (2004).
2. Lamonds, L., Wanna, N., Woodside, R., Dow, T., Garrard, K., Sohn, A. Design and Fabrication of a Two-Mirror Diamond Turned Telescope, Progress Report #1. Navy Electro-Optics Center, (2005)
3. Wanna, N., Dow, T. Design of Reflective Optical Systems. Precision Engineering Center Annual Report, (2006).
4. Irving, B. Code V Introductory User's Guide. ORA, 44, (2004).
5. Thompson, K. Description of the Third-Order Optical Aberrations of Near-Circular Pupil Optical Systems without Symmetry. Optical Society of America, 1389-1401, (2005).

This page intentionally left blank.

3 MODELING OF VIBRATION AND DITHERING IN SPDT

D. Lucas Lamonds
Graduate Student
Thomas Dow
Professor
Department of Mechanical and Aerospace Engineering
Kenneth Garrard and Alexander Sohn
Precision Engineering Center Staff

3.1 INTRODUCTION

The objective of this work is to develop a model to simulate the effects of vibration disturbances as well as intentional cross-feed tool dithering on the surface finish of single-point diamond turned parts. This model can be used to optimize cutting conditions to create the best surface finish.

Surface finish in single-point diamond turning is primarily influenced by four factors: Geometry, vibration, material properties, and tool edge quality. The first-order geometric model using the parabolic approximation for the tool radius gives the peak-to-valley roughness

$$PV = \frac{f^2}{8R} \tag{1}$$

defined by the cross feed (f), and the tool radius (R). This approximation is often used to tool radius and feed rate to create a desired surface finish. However, for large tool radii and small feed rates, the predicted finish is not achievable.

The precisely controlled cross feed rate of the tool during diamond turning produces a surface that has periodic cusps. These cusps can also have a significant impact on the performance of optical surfaces that operate in the visible range by introducing coherent scatter that produces the familiar “rainbow” appearance of diamond turned surfaces in white light. Diffraction effects have traditionally limited diamond turned optics to infrared and near infrared wavelengths [1]. By dithering the tool in the cross feed direction, the regular spacing of the cusps can be randomized and this may reduce the diffraction effects.

3.2 MACHINE VIBRATION

Assuming suitable materials are selected and the tool edge quality is high, vibration is typically the next largest factor in determining surface finish. The origin of this vibration can be from a number of sources, although the axes of the machine or the spindle are the most likely candidates. The ASG 2500 Diamond Turning Machine at the Precision Engineering Center suffers mainly from a 64 Hz vibration of the Z-axis, which has a magnitude of about 20 nm. This amplitude can vary slightly depending on spindle rpm and balance. Either of these can increase this vibration. For the purposes of the following discussions and examples, the vibration of the ASG 2500 Z-slide will be used as the source of the vibration [2], though the technique can be applied to any source.

The impact of vibration on a diamond-turned surface is generally to degrade the surface finish. In its simplest form, a sinusoidal vibration in the normal direction would leave an RMS surface finish of 0.707 times the amplitude of the vibration. It would seem that the surface finish could never be improved beyond this value and there would be no point in slowing the feed rate or using a larger radius tool. This assumption is, however, incorrect due to interaction between neighboring grooves at small feed rates. By modeling the surface produced by a vibrating tool, it can be shown that the surface finish is no longer limited by the vibration amplitude but can be improved by moving to finer feed rates.

3.3 Z-AXIS VIBRATION MODEL

The tool edges are formed by calculating a vector of z-positions for each cross feed X-coordinate and each depth of cut Z-coordinate for a surface profile vector of x-positions with even spacing. The vector of z-positions is calculated with the Cartesian formula of a circle:

$$(x - x_0)^2 + (z - z_{0)})^2 = R^2 \tag{2}$$

where x is the vector of x-positions for the profile, x_0 is the cross feed X-coordinate, z is the vector of z-positions for the surface profile, z_0 is the depth of cut Z-coordinate, and R is the tool nose radius. Only the minimum z-position is kept for each x-position in the surface profile vector. The final product is a surface profile that only displays that passes of the tool the will leave a residual cusp. Also, this gives a final surface trace with constant sample density in the x direction.

The depth of cut changes around the periphery of the part with the vibration environment:

$$depth = A \sin\left(\frac{\omega x}{\Omega f}\right) \tag{3}$$

where A is the vibration amplitude, ω is the vibration frequency of the tool, x is the radial position of the tool and Ω is the vibration frequency of the spindle.

As shown in Figure 1 where multiple traces have been generated, the redundant points in the overlapping regions do not appear in the final surface contour. Individual cross-traces at different rotational positions of the spindle can then also be assembled into 3D profiles as shown in Figure 2. When creating the 3D profile, the number of traces in the Y direction is equal to the number of points per trace in the X direction allowing a sample with a uniformly spaced grid of samples.

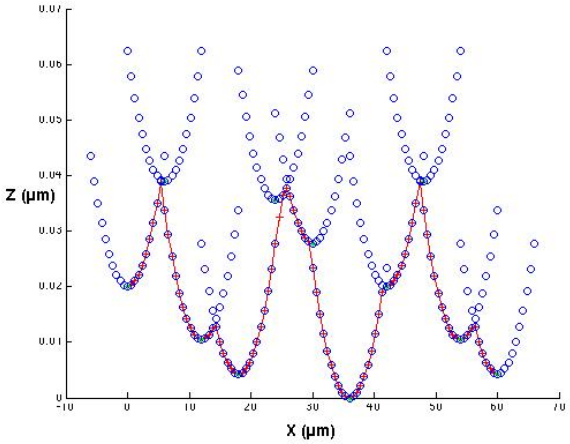

Figure 1. Points along multiple tool profiles, at varying depths due to vibration, produce a finished surface contour.

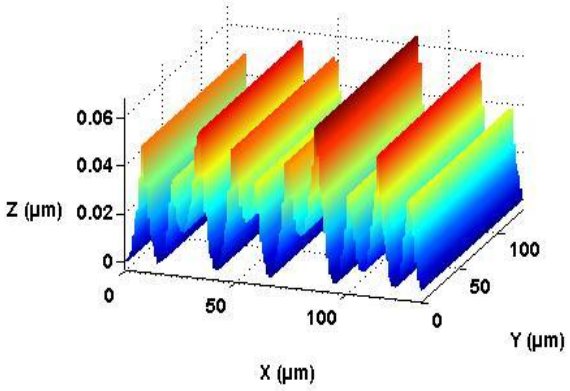

Figure 2. Multiple simulated surface profiles assembled into a 3-D surface.

It is at lower feed rates that the effects of tool vibration on a diamond-turned surface become interesting as illustrated in Figure 3. The illustration shows the surface left at small feed rates where the crosshairs show the tool location at each pass in the profile. A number of passes are not represented at all in the finished surface, leaving only the most extreme passes and, hence, a smoother surface than would be expected with machine vibration. Figure 4 shows that as the theoretical RMS surface finish calculated with the parabolic approximation decreases the effects

of machine vibration on RMS roughness are reduced. The roughness data in Figure 4 are reduced by using finer cross feed rates while holding the tool radius constant.

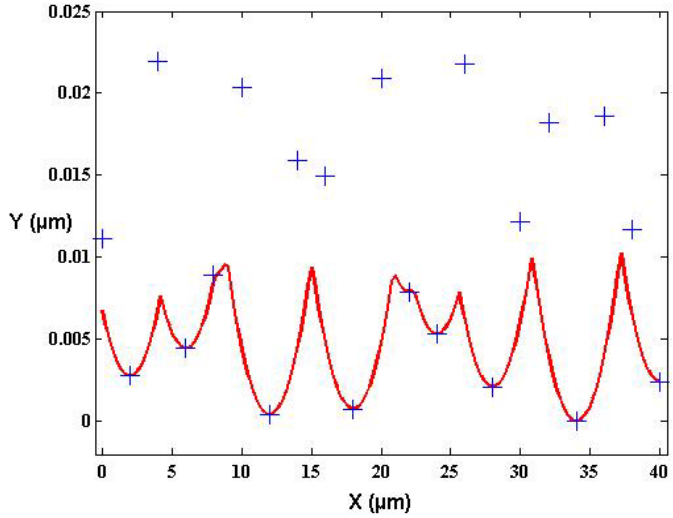

Figure 3. At fine cross-feed rates, some passes of the tool (+) are not represented in the finished surface. This produces a better finish than would be expected from the RMS of the vibration alone.

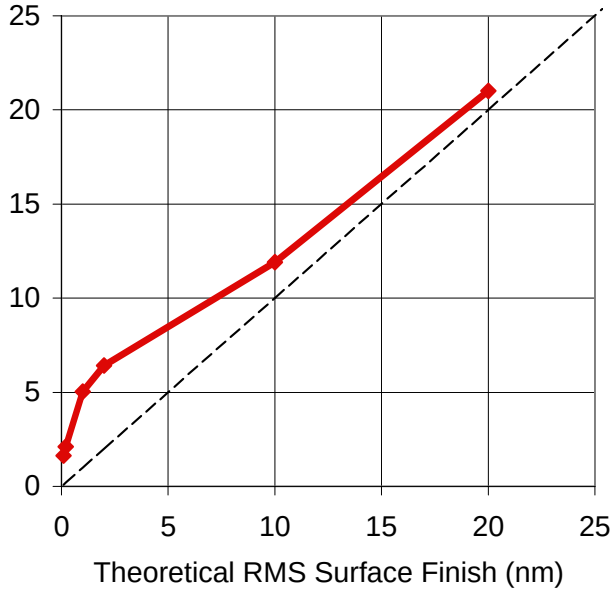

Figure 4. As theoretical surface finish decreases the effects of machine vibration on surface finished are reduced.

3.4 MACHINE VIBRATION EXPERIMENT

To verify the simulations, a plated copper sample was machined with the same feed rates used in the simulations. Machining experiments were performed on an ASG 2500 DTM using a 505 rpm spindle speed and a 0.5 mm radius, zero rake natural diamond tool. The laboratory temperature was controlled to 20 ±0.05°C. Petroleum oil cutting fluid (Mobilmet Omicron®) was used for lubrication and chip removal.

Eight 2 mm wide bands were machined on the 50 mm diameter sample with cross feeds of 0.6, 0.9, 1.9, 2.7, 6.1, 8.6 and 19.1 µm/rev. The surface was ultrasonically cleaned and then measured on a Zygo NewView 5000 Scanning White-Light Interferometer (SWLI) using 50X magnification. The measurement area is 108 µm X 144 µm. Figures 5 and 6 show the typical profile measurement result. The effects of vibration on groove depth can clearly be seen in the profile at this large feed rate. The depth varies randomly as the tool traverses the part. Note a small chip is visible in the tool edge as a repeatable defect from each pass. At finer feed rates, this portion of the tool does not, however, have an effect.

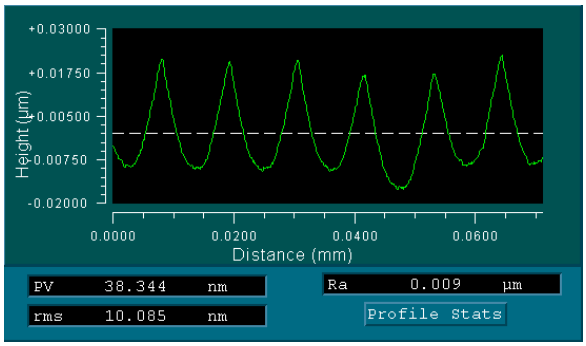

Figure 5. Typical surface profile measurement illustrating the depth change as a result of vibration with large feed rate of 11.3 µm/rev.

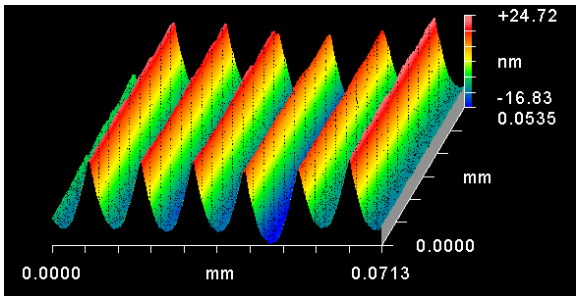

Figure 6. A typical measurement result in oblique plot form. This is the same machined surface shown in Figure 5.

The results for a series of simulations and cuts performed to verify the model are shown in Figure 7. The plot also shows the line that represents the theoretical finish approximation for a parabolic surface:

$$RMS = \frac{f^2}{26.6R} \tag{4}$$

where f is the cross-feed rate in µm/rev and R is the tool radius (500 µm). Clearly, the surface finish can improve significantly beyond the RMS 7.7 nm limit of a simple sinusoidal vibration. The finish also continues to improve with finer feed rates between 2 and 5 µm, when they already deviate significantly from the theoretical parabolic approximation.

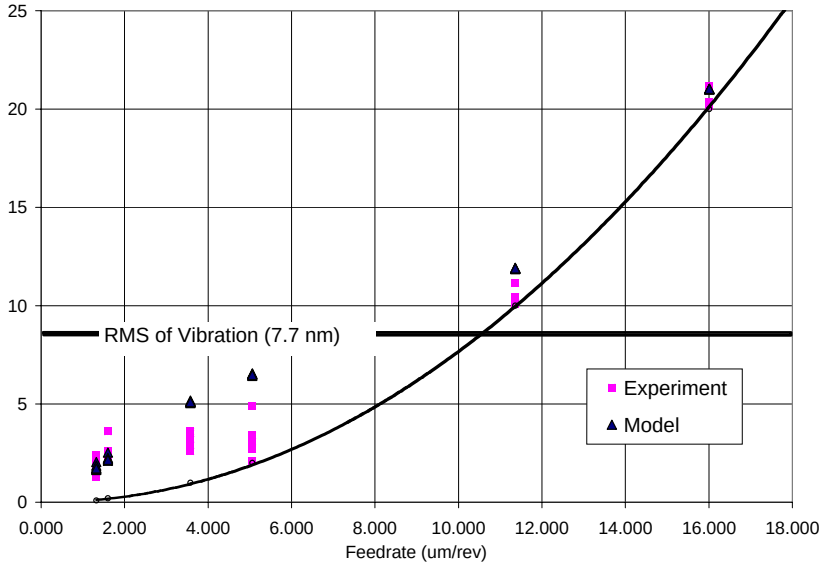

Figure 7. Results from experimental and model data with threshold of RMS Z-axis vibration and a curve to represent the theoretical parabolic RMS surface roughness.

3.4.1 ENVIRONMENT

As the results displayed in Figure 7 show, at theoretical finishes below 2 nm RMS, the model does not predict the surface finish. At these extremely fine finishes, other factors begin to take effect such as environmental effects and material anisotropies. While the temperature variation in the laboratory is controlled to less than 0.1°C, even such small temperature fluctuation can have an impact on the surface finish.

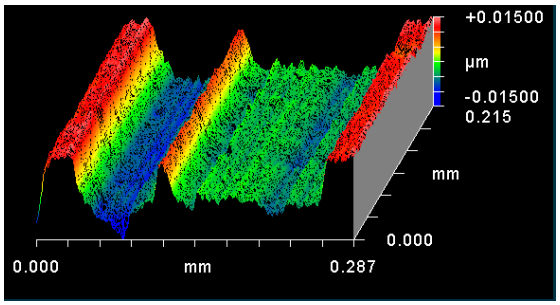

Figure 8. Surface finish degradation can occur due to temperature variations in the laser interferometer deadpath.

At small feed rates (less than 1 µm/rev), small room temperature changes over several minutes can impact the surface finish. For example, Figure 8 shows a 30 nm change in surface height that is similar in magnitude to the change in measured position resulting from a refractive index change over the 250 mm deadpath of the laser interferometer. Given a maximum temperature variation of 0.1º C, the calculated resultant deadpath error using the Edlén equation [3] is 25 nm. This limitation reflects the need to reduce deadpath, compensate for environmental fluctuations with a refractometer, operate in a vacuum, or use another means of position feedback such as a linear encoder. While linear encoders do not eliminate errors due to thermal fluctuations, expansion of the scale due to temperature changes tends to have a much longer period, so errors move into the figure error regime rather than roughness.

3.4.2 MATERIALS

Material effects, such as inclusions or grain boundaries have a much larger impact in materials such as 6061 Aluminum [4], though apparently there are defects even in the fine-grained, plated copper used as shown in Figure 9.

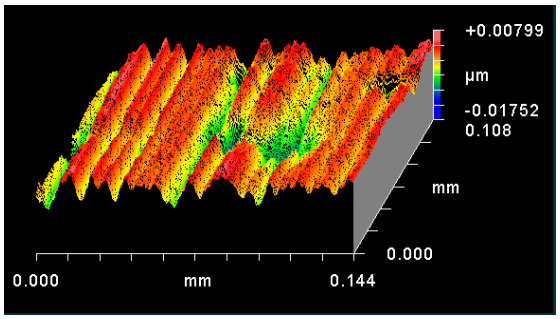

Figure 9. 3D surface profile of a plated copper surface machined at fine feed rates showing local defects that could be caused by material defects.

3.4.3 CONTROLLER TRACKING ERROR

The final contribution to a degraded surface finish is from errors in the control of the axes. In the case of the ASG 2500 DTM, controller tracking error was measured to be less than 10 nm Peak-to-Valley [4]. While of some significance, the effects of this tracking error are still not as significant as those due to temperature variations and material defects.

3.5 CROSS-FEED DITHER MODEL

The Z-axis vibration model was expanded to accommodate intentional movement of the tool in the X (cross feed) direction. The goal was to subtly change the spacing of the grooves to improve the optical performance but without a major change in the surface roughness. The spacing of each cross feed was moved from its original X coordinate in either a positive or negative direction. Figure 10 shows the center of each cross feed with a crosshair and resultant surface trace without the effects of Z-axis vibration. The cross feed is no longer periodic and the residual cusps are no longer uniform depths and widths. Figure 10 also demonstrates that any deviation from perfectly periodic cusps will increase the surface roughness from the theoretical PV without dither of 5.5 nm (1.6 nm RMS) to 10 nm (2.4 nm RMS).

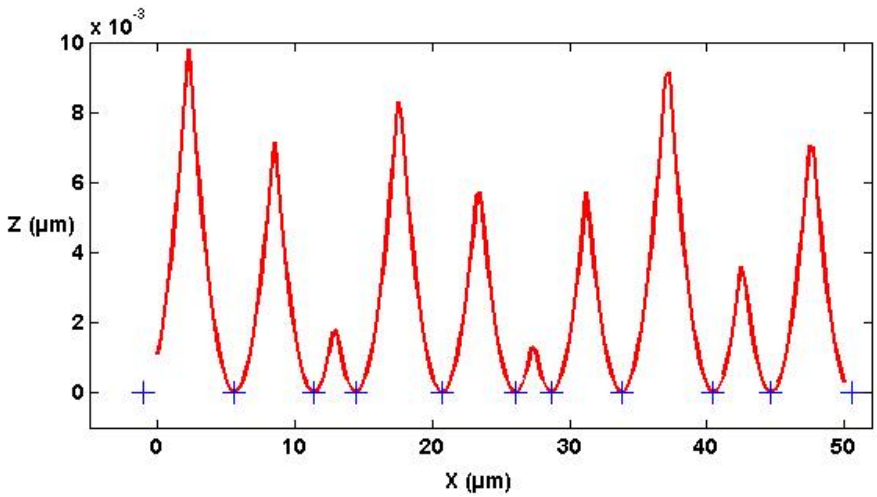

Figure 10. Dither Concept showing cross feed centers (+) and resultant profile. A 570 µm nose radius tool was used with a 5 µm/rev cross feed. *PV* = 10 nm and *RMS* = 2.4 nm.

A Gaussian distribution was selected for generating the cross-feed variations. Several standard deviations (σ) and cross-feed rates were modeled. Standard deviation was calculated using +/- 3σ distributions with a spreads equal to 0.5x, 1x and 2x the cross feed rate. Because cross-feed dithering has a negative effect on finish quality, dithering frequencies were kept low enough such that, for a typical surface finish profile size, up feed changes were negligible. A 3D profile with dithering and machine vibration is shown in Figure 11.

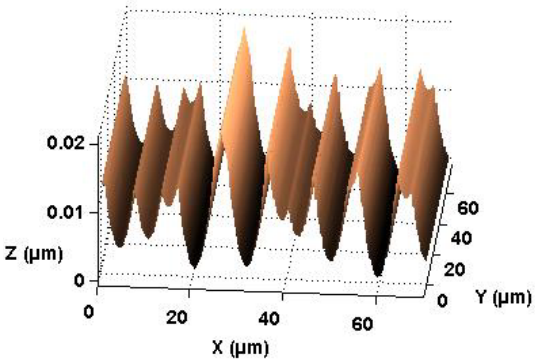

Figure 11. Sample 3D surface profile with cross feed dithering (motion along the X-axis) and Z-axis machine vibration.

To evaluate the spatial repetitiveness of the surface, the autocovariance function [5] was applied to each trace generated by the model. The autocovariance function is the product of two copies of the same surface contour as one is shifted (lag length) relative to the other. The function has units of height squared and the first value, where the lag length equals zero, is the square of RMS roughness. One copy is moved with respect to the other in increments of sample spacing. A peak at a certain lag length indicates that the surface has repetitive features at that spacing. A surface with perfect cusps will alternate between positive (agreement) and negative (disagreement) when evaluated with the autocovariance function as shown in Figure 12. A random surface with the same surface roughness will start at the same value for zero lag length but will drop quickly to zero with no oscillations. Future experiments will be used to evaluate horizontal dither (using a fast tool servo) to see if it can be used to extend the capability of diamond turning.

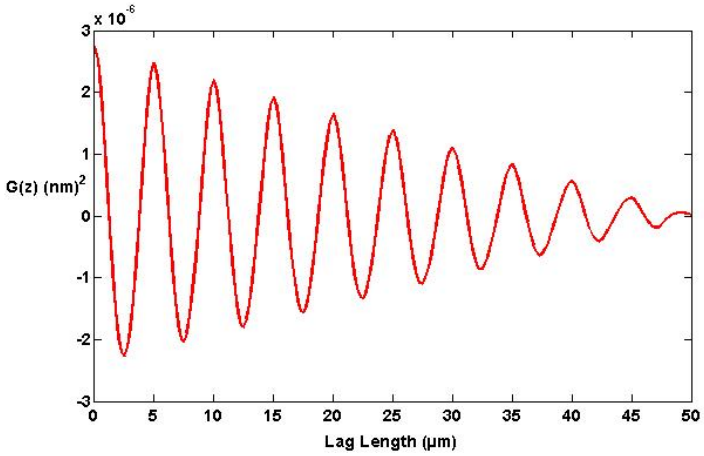

Figure 12. Autocovariance of theoretical profile. f =5 µm/rev, R = 570 µm, PV =5.5 nm, RMS = 1.6 nm.

3.6 CONCLUSIONS

Understanding the source of the features on a diamond turned surface will lead to the evaluation of techniques to reduce their amplitude. Two issues have been addressed here; 1) vertical machine vibration and the resulting change in depth of cut and 2) the concept of horizontal motion to reduce the coherence of the grooves.

MACHINE VIBRATION

The conventional wisdom that there is little point in machining at lower feed rates beyond the point where the measured surface finish is worse than the theoretical finish (obtained from the parabolic approximation) simply does not hold. Finer feed rates continue to reduce the impact of vibration to a point where it does not impact the surface finish any more and material or environmental effects take over. In the particular case of the PEC's ASG 2500 DTM, feed rates lower than 2 µm using a 0.5 mm radius tool do not improve the surface finish. Factors other than vibration dominate below this feed rate. Until these the impact of these factors is reduced, smaller feed rates simply add time to the machining effort with little gain.

CROSS-FEED TOOL DITHERING

It has been proposed that cross feed tool dithering can subtly randomize the regularly spaced grooves formed in diamond turning that cause the surface to act like a diffraction grating. This could reduce coherent scattering that produces undesirable structure in the optical output that often makes diamond-turned optics unsuitable for visible applications. By careful selection of motion parameters, spatial periodicity observed in the surface profile was reduced without a significant change in the RMS roughness was affected minimally. RMS roughness of finer feed rates was less affected by dithering because many tool passes were not represented in the final surface contour thus are the fine feedrates are the best candidates for dithering. An experiment that validates the horizontal dithering model is needed. Challenges in this experiment are mainly associated with having the experimental tool motion duplicate the modeled tool motion such that groove spacing is truly random and there is little up feed variation for any given 3D surface profile.

REFERENCES

1. Schaefer, J.P. Progress in Precision – Single Point Diamond Turning (SPDT) of Optical Components. ASPE Proceedings, Spring Topical Meeting Presentations DVD, (2001).
2. Slocum, A.H. Precision Machine Design. John Wiley, New York, (1994).
3. Abler, J.A. Process Modeling and Correction of Dynamic Errors in Diamond Turning. PhD Thesis, North Carolina State University, (1994).

4. Dow, T.A., Lamonds, L. Fabrication of Optical Surfaces and Fiducials, PEC Annual Report, (2005).
5. Bennett, J.M., L. Mattsson. Introduction to Surface Roughness and Scattering. Optical Society of America, Washington, D.C., 44-47, (1989).

This page intentionally left blank.

4 LONG RANGE SERVO

Qunyi Chen and Arun Veeramani
Graduate Students
Thomas Dow and Gregory Buckner
Professors
Department of Mechanical and Aerospace Engineering
Kenneth Garrard and Alexander Sohn
Precision Engineering Staff

4.1 INTRODUCTION

Diamond turning (DT) has revolutionized the fabrication of lightweight optical surfaces for consumer, defense and science applications such as contact lenses, forward-looking infrared radar and infrared spectrometers. It has made this impact not only because it can accurately and rapidly fabricate diffractive, refractive and reflective optical surfaces, but also because it can create reference features tied to the optical surfaces to guarantee optical alignment.

An emerging trend in optical design is the use of Non-Rotational Symmetric (NRS) surfaces to reduce complexity, bulk and weight while improving optical performance. To create these so-called freeform surfaces, DT machines have been operated at very slow spindle speeds or modified with a piezoelectric Fast Tool Servo (FTS) or a flycutter. Unfortunately, the FTS offers a limited stroke and the other alternatives are plagued by thermal drift during extremely long fabrication times. The proposed Long Range Servo (LRS) integrates existing technologies (air bearings, linear motors, high-resolution encoders and real-time control) into a lightweight, moving tool holder that can be retrofitted onto a conventional DT machine. The result is a high-bandwidth, high-resolution, long-stroke machine tool that can increase production and reduce cost for freeform surfaces.

4.2 TECHNICAL CHALLENGES

The goal of the LRS is to create optical quality surfaces while moving the tool over a range of ± 2 mm at a frequency of 20 Hz. To achieve this goal, a number of technical challenges must be overcome.

Form Error Diamond turning machines can create excellent form fidelity because of their stiff, straight, slow linear slides and accurate air-bearing spindles. This process is ideally suited (and was developed) for rotationally symmetric surfaces such as spheres or rotationally-symmetric

aspheres. Moving the tool to create NRS surfaces at typical spindle speeds would be well beyond the bandwidth limits of the large, heavy axes. The spindle speed could be reduced but this would lead to long fabrication times and potential for thermal drift. Reducing the mass of the slide to improve its bandwidth is the aim of the LRS but this makes it more susceptible to disturbances from vibration or cutting force variations.

Surface Finish Simple theoretical relationships between machining parameters (spindle speed, axis velocity) and tool geometry can be used to predict surface finish. Tool waviness, tool wear and material properties can degrade the surface finish but for the dynamic conditions envisioned for the LRS, machine vibrations and dynamic forces will be more significant factors.

Motion Planning Advanced algorithms must be developed to decompose the freeform surface geometry into the synchronized, relative motion commands for the machine axes.

The goal of this project is to address these technical challenges. The result will be an Ultra-precision servo drive and control systems that will quickly create optical quality freeform surfaces.

4.3 SYSTEM DEVELOPMENT

A prototype LRS was built during 2004 in a collaborative project with Precitech that was supported by NASA. NSF recently funded a project to continue the development of this concept. The LRS takes advantage of air-bearing slide design, linear motor technology, high-resolution encoders and control algorithms to increase the velocity and range to 4 mm at 20 Hz. The lightweight aluminum-honeycomb piston has a triangular cross-section with a mass of 650 gm with motor. The diamond tool is attached to the front of the piston and the linear motor to the back.

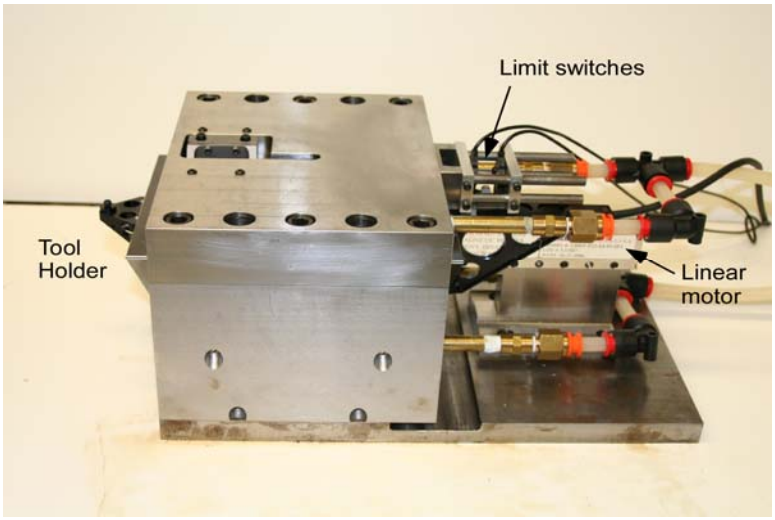

Figure 1. Photograph of the LRS system

The surface finish and figure error for this actuator were not acceptable for optical surfaces due to system deficiencies discussed below.

- Encoder noise and resolution – The long-range, high speed axis is a challenge for a linear encoder because the data rate cannot exceed the clock of the encoder electronics. The 20

μm period of the Renishaw steel tape is relatively long and, coupled with noise on the sine waves, reduces the resolution to approximately 50 nm. A glass scale Heidenhain encoder will be installed with 10 nm resolution and a 0.25 nm Sony scale is on order.

- Vibration of machine axis – When operating at maximum speed, the mass of the LRS excited the natural frequency of the Z slide of the DTM. For the initial experiments, the LRS will be mounted on a separate base and the motion of the slide will be measured without the complication of the DTM slide stiffness.
- Noise in PWM amplifier – The Pulsed Width Modulated power supply for the LAT motor created significant noise which excited the slide and degrade the surface finish. A linear amplifier has been substituted.
- Control system – The LRS operated as one axis within the DTM control system on the Nanoform 600 (DeltaTau UMAC). This controller was neither flexible nor fast. A dedicated, high-speed control computer is being installed to address control issues. A xPC Target virtual DSP will be used initially and then switched to a DSP system.
- Non-linear slide motion – A non-linear effect has been identified in the slide motion. The phase angle between the commanded and actual position is a function of the frequency and amplitude of the motion. Additional experiments are planned to understand the source of this non-linearity .

The short term goal is to address these issues by modifying the current prototype as described above before a total redesign is undertaken. These experiments should provide baseline data to plan changes in the mechanical design and control system.

Safety System One of the deficiencies in the first design is the lack of a safety system to control the operation of the LRS. The safety system must remove power to the motor if a number of conditions occur such as limits of travel, loss of air pressure, motor overheating or amplifier problems. Figure 2 shows the schematic of the system implemented for the LRS. If any of the anticipated faults occur, the amplifier will remove power from the motor.

4.4 LRS MOTION CONTROL

4.4.1 SYSTEM MODEL

Baseline simulations of the LRS motion were made to investigate the impact of physical parameters (piston mass and motor force) and control system design (algorithm and update time). This single DOF system shown in Figure 3 consists of an undamped mass m, a force disturbance $F_d(t)$ (representing cutting forces at the tool/workpiece interface), and displacement feedback $Z(t)$. The piston position is controlled by manipulating voltage $V(t)$ to a linear actuator, providing the

actuation force $F_a(t)$, in response to a position error between the commanded position $Z_{ref}(t)$ and the feedback $Z(t)$.

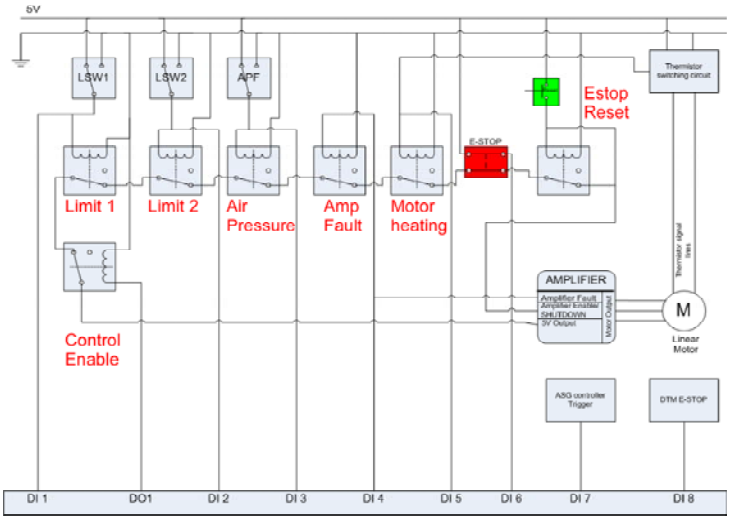

Figure 2. Safety system for LRS control

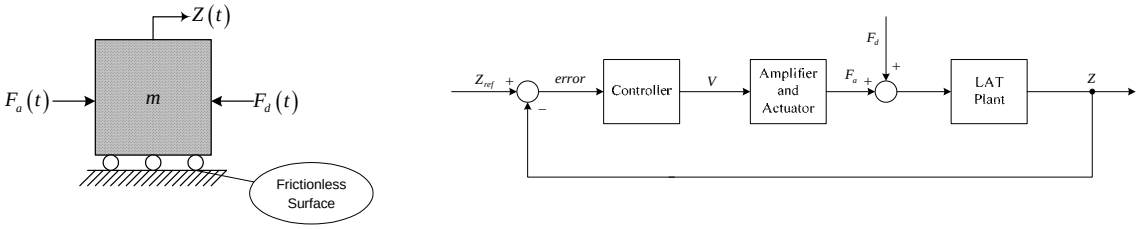

Figure 3. Model of LRS dynamics, with feedback control diagram

Figure 4 provides a more complete representation of LRS motion axis. The major components of physical dynamics are the linear motor (Airex P12-1) and power amplifier (Aerotech BL10-80A).

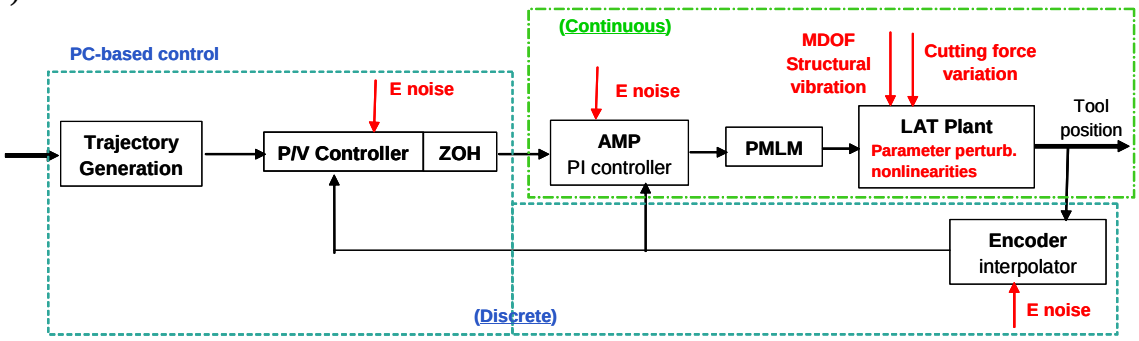

Figure 4. Representation of LRS motion axis

4.4.2 CONTROL SYSTEM PERFORMANCE

The functional requirement for the LRS is to track a commanded trajectory while confronted by disturbances, measurement noise, plant uncertainty, actuator saturation and bandwidth limitations. From the motion system response, the control performance can be assessed based on stiffness, sensitivity, responsiveness, overshoot, accuracy, stability and robustness. Among these performance criteria, commanded profile tracking error and disturbance rejection are most powerful tools to evaluate the selection of physical parameters.

Tracking Error, E_R One common test performed with a fast tool servo is to create a tilted flat. If done correctly, a flat surface will be created by driving the tool in a sine wave motion with amplitude growing as a linear function of the radius. As a result, an important modeling parameter for evaluating system performance is the tracking error; that is, the ability to follow a sine wave with minimum amplitude attenuation and phase lag. The maximum operating conditions for the LRS is a 20 Hz sine wave with amplitude of 2 mm (4 mm PV).

Disturbance Rejection, E_D During the machining operation, small changes in the depth of cut will change the force on the tool and introduce a disturbance to the positioning system. Vibration of the LRS structure can also create forces disturbances. Disturbance rejection is an important characteristic of a motion control system. The disturbance is not only from the cutting force variations but also from electrical noise in the controller and the amplifier. These disturbances result in poor surface finish.

4.4.3 LRS MODEL PERFORMANCE

To optimize the inherent performance/design tradeoff, the physical design needs to be combined with control system design to create a new LRS system. Time-domain simulations were made to illustrate the impact of key design parameters on the profile tracking (a sinusoidal trajectory with 2mm amplitude at a frequency of 20 Hz) and disturbance rejection (a sinusoidal cutting force disturbance with 0.025 N amplitude at a frequency of 54.849 Hz). The position errors resulted from PID feedback control are in Table 1. For each case, the controller gains were selected by optimizing the performance (following error) using the sine wave profile. Using this algorithm, the disturbance was introduced and the resulting positioning error was calculated.

Table 1. Simulated control performance for different selections of physical parameters

		Tracking Error Amplitude (μm)	Disturbance Induced Position Error (nm)
Case 1	Motor Power: 84N Mass: 0.5Kg Sampling rate: 2.5KHz	1.5065	7.7

Case 2	Motor Power: 336N Mass: 0.5Kg Sampling rate: 2.5KHz	1.5065	7.7

The first two cases illustrate the influence of the motor power on the low mass system at slow feedback. In these cases, the power available from the small motor is sufficient to move the piston at the desired rate and additional power does not improve either tracking error or disturbance rejection. Slow sampling rate reduces the gain for the control system and the position is more influenced by the disturbance.

		Tracking Error Amplitude (μm)	Disturbance Induced Position Error (nm)
Case 3	Motor Power: 84N Mass: 2Kg Sampling rate: 2.5KHz	2.1116	3.2
Case 4	Motor Power: 336N Mass: 2Kg Sampling rate: 2.5KHz	1.5065	2.3

Cases 3 and 4 illustrate the change in the motor power at the large piston mass and slow feedback rate. The tracking error is larger for the smaller motor but the larger motor can provide enough force to improve the tracking error over that of the first 2 cases. However, the increased mass of the piston helps to reduce the effect of the disturbance.

		Tracking Error Amplitude (μm)	Disturbance Induced Position Error (nm)
Case 5	Motor Power: 84N Mass: 0.5Kg Sampling rate: 40KHz	0.2420	1.4
Case 6	Motor Power: 336N Mass: 0.5Kg Sampling rate: 40KHz	0.2420	1.4

Cases 5 and 6 illustrate the improvement in Cases 1 and 2 if the sample time is increased by a factor of 16 from 2.5 KHz to 40 KHz. The previous experiments on the LRS used the slow feedback rate and the new system will use the faster rate. The tracking error is reduced by a factor of 6 and the disturbance position error is only about 20% of the slower system. The larger motor does not help the performance.

		Tracking Error Amplitude (μm)	Disturbance Induced Position Error (nm)
Case 7	Motor Power: 84N Mass: 2Kg	0.2419	0.6

	Sampling rate: 40KHz		
Case 8	Motor Power: 336N Mass: 2Kg Sampling rate: 40KHz	0.2420	0.6

The final two cases illustrate the faster cycle time with the larger mass. Here the tracking error is the same as the lighter mass but because of the increased inertia, the system is less influenced by the force disturbance.

Motor Power and Saturation The linear motor is normally sized by the maximum force requirement. It has been found that:

- The higher the motor power, the less the profile tracking error.
- Most of motor power is used for tracking purpose while disturbance rejection only requires small amount of control effort. Therefore, increasing motor power for small mass system (i.e. 0.5~2Kg) does not improve its disturbance rejection. Good disturbance rejection requires high controller gains and fast cycle times.

Piston Mass and Size Producing a piston for the LRS that is lighter than the current 0.65 Kg will improve the tracking performance and reduce vibration transmitted to the structure. However, the material, shape and size must be selected based on structural natural frequency and air bearing stiffness.

- Decreasing mass will improve the profile tracking performance. However, if the mass and PID gains/motor power are increased proportionally, there is no impact on profile tracking error.
- Increasing the mass will improve the disturbance rejection.

Control System Cycle Time When the mass of LRS is reduced to improve its bandwidth, its disturbance rejection capability must be maintained by setting high PID controller gains. This can only be done by using a high sampling rate. In addition, high PID gains with a fast sampling rate reduce profile tracking error. In reality, there is always a limit on how fast the digital controller can sample the system and update the output due to the availability of hardware. The current xPC Target system can operate at 33 KHz sampling rate and new hardware has been ordered to increase this rate beyond the 40 KHz used in the model.

4.4.4 DAMPING FOR SERVO SYSTEM

Controlling an undamped servo system using discrete-time algorithms can be complicated by several factors. Fixed sampling rates, bandwidth restrictions in the amplifier and actuator and computational issues limit the amount of damping that can be introduced by control. The resulting system can exhibit oscillations, overshoot and reduced stability margins. Incorporating

passive damping has been shown to improve the stability, robustness, and performance of lightly-damped servo systems. Determining the optimal damping level needed to realize the requisite bandwidth and surface finish is an area that needs investigation.

In a classical three-term position loop PID control system, the physical damping and controller damping are not equivalent. However, if a velocity PD controller is inserted inside of position loop PI controller, they become equivalent. Implementing the velocity control loop will require an accurate estimation of the velocity in real-time that may be beyond the capability of a differentiated position signal.

4.5 REAL-TIME CONTROL SYSTEM IMPLEMENTATION

The initial deployment of real-time system for LRS will be implemented using the MATLAB xPC Target development environment. In this environment, a desktop PC is used as the host running MATLAB, Simulink, Stateflow and Real Time Workshop to create and simulate a control algorithm via Simulink block diagrams. Once the simulation is complete and the results are acceptable, executable code is created and downloaded to a second "target" PC running the xPC Target real-time kernel. After the downloading, the target application can be run in a stand-alone, real-time mode. The xPC Target control development and rapid prototyping system integrate the entire development cycle into a single environment so that the individual development stages between simulations and tests can be run and rerun without frequent readjustment. However, this flexibility has its cost – overhead time. Measurements of the cycle time for a simple test with one analog input and one analog output, revealed a 20 μs overhead task execution time. This time stayed constant as more complicated computational tasks were added so that for a typical control algorithm, the total execution time may be on the order of 30 μs. As a result, independent DSP controller might be adopted if the sampling rate needs to be further increased.

4.6 CONCLUSIONS AND FUTURE WORK

The goal of this project is to determine the potential of an air-bearing supported, linear motor driven, encoder scale measured long range servo to rapidly produce freeform optical surfaces. This would provide, for example, the ability to machine a biconic surface with 4 mm of sag at 600 rpm.

A prototype LRS system was fabricated in 2004 in a cooperative project with Precitech that was funded by NASA. This system is being rebuilt under a new NSF project with improved components to upgrade its performance. In addition, structural and control studies are being undertaken to evaluate the components of the prototype and lead to a 2nd generation design.

5 DESIGN AND FABRICATION OF AN OPTICAL ASSEMBLY TEST

Alexander Sohn
Precision Engineering Staff

5.1 INTRODUCTION

Following the experience gathered with the two-mirror Cassegrain system, it was decided that to clearly identify the error sources in the machining and assembly of optical systems in general, a simple test system was needed. This system could be used to test various aspects of the machining and assembly process, but through the use of simple geometries allow different error sources to be distinguished from each other. Also, different assembly techniques and their effectiveness can be explored using such a system.

5.2 SPHERICAL MIRROR EXPERIMENT

The simplest form of a lightweight alloy optical system would be one reflector attached to a support. The reflector could be a flat, sphere, off-axis sphere or conic with a matching optical surface machined into the end of the tube to test alignment. As shown in Figure 5-27, these varying configurations can be tested in an interferometer. Each component can be measured both independently and as part of the assembly so that the influence of the assembly can be tested. The plan is to start with a flat test because it is the simplest geometry to machine and measure. Tilt alignment of the flat mirror and the flat on the end of the tube can be measured as well as distortion in each surface due to mounting stresses. Once the flat has been machined and thoroughly measured, the next test is for a spherical mirror. A matching spherical surface in the end of the tube will allow the measurement of focus as determined by the length of the tube. This critical parameter is often difficult to measure in completed systems and, with multiple components placed in series, it is very difficult to distinguish error sources. The spherical mirror test will also identify translational errors in the system. Finally, upon completion of the spherical mirror test, an off-axis sphere will be machined on-axis using the Variform Fast Tool Servo. This will test the final degree of freedom necessary for accurate alignment of freeform systems: rotation about the optic axis.

5.3 COMPONENTS

For this demonstration purpose, four parts will be made: the spherical mirror, the mounting tube, two brass pins and an intermediate mounting chuck for the tube. The final assembly is shown in Figure 1.

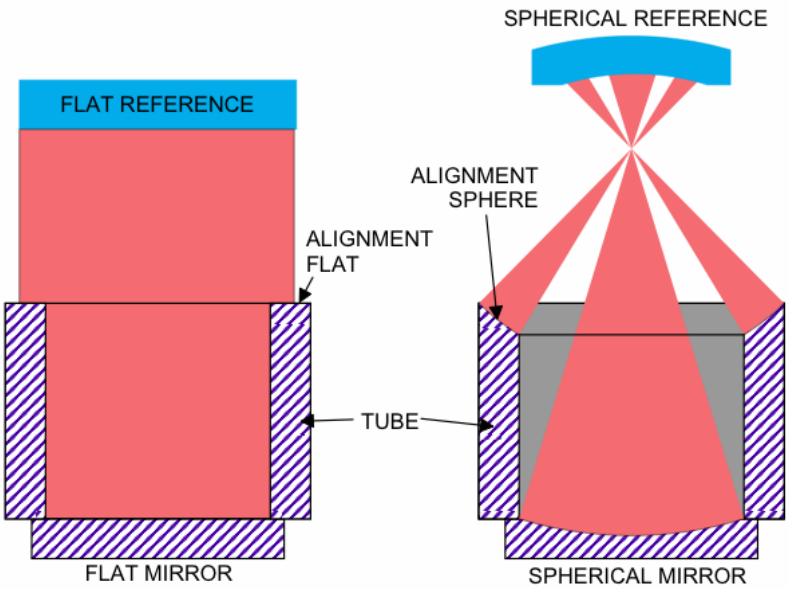

Figure 1. Two configurations of the test system. The flat mirror version is sensitive to tilt and distortion in the mirror while the spherical version tests focus and translation misalignment.

Mirror

The mirror has a flat fiducial surface surrounding the optical surface. For the flat test configuration both surfaces will be the same. The spherical mirror, also shown in Figure 2, will have a separate annular region. Only the areas around the pin holes serve as the quasi-kinematic mounting regions that line up with the mounting pads on the tube. The two pinholes, bored with a diamond flycutter/boring tool provide translation alignment as well as clocking. Also, two threaded extraction holes aid in disassembly of the system. The pins may add a small interference component, so some force may be necessary to extract the pins from their mating holes. This will be performed by threading one setscrew into each hole until they lift the mirror from the tube.

Mirror material The material for the mirror was chosen based on the generally accepted mechanical properties and the high reflectance of 6061 Aluminum. Superior thermal stability and absence of stress are achieved with a T 651 temper, so this was selected over the more common T6 temper. [1]

Fabrication mounting Given that the total vacuum force on the mirror back from 10 psi vacuum is about 300 lbs, a significant amount of distortion can be expected if both mounting surfaces are not perfectly flat. One option would be to reduce the vacuum pressure, but a better method is to simply apply the same pressure over a smaller area. This has the added benefit that

[1] http://www.nasatech.com/Briefs/Sep05/GSC147361.html

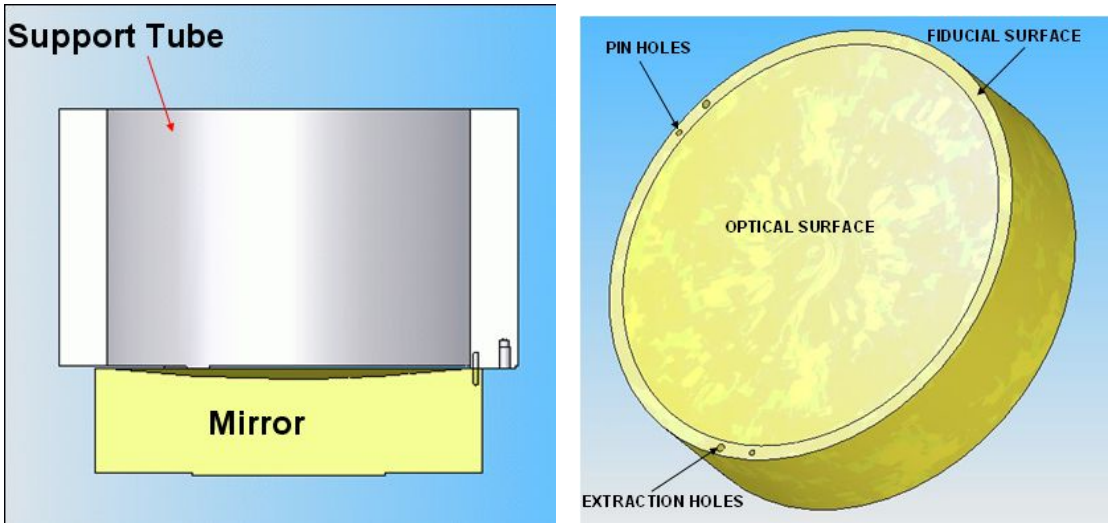

Figure 2. Assembly (left) showing mirror mounted to tube and mirror details (right).

a smaller area is statistically less likely to contain distorting imperfections than the larger area. Thus, a 3" diameter raised region on the back of the part will minimize distortion when mounted on a vacuum chuck and the spherical optical surface. As Figure 3 shows, the reduced force of the smaller area significantly reduces overall distortion from 400 nm to 40 nm.

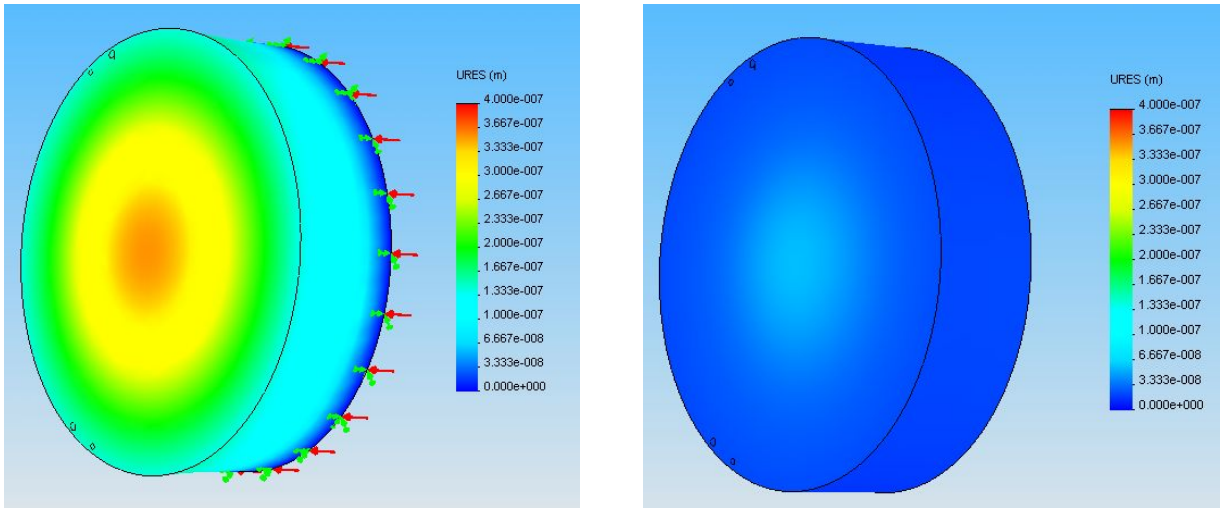

Figure 3. Distortion when the entire back surface of the mirror (150 mm) is used to vacuum the part to the chuck (left) and when only a 75 mm diameter region in is used (right).

Clocking Fiducial A fiducial will be scribed into the mirror OD to test alignment of the optical system in the clocking direction. With pins inserted into the holes, the pins will be touched on the rake face of the diamond tool to establish clocking alignment (in the rotation direction) with the spindle encoder. A scribe mark as shown in Figure 4 will then be made on the OD that will match a similar scribe mark in the tube after assembly. While clocking alignment has no impact

on the optical performance of the flat or spherical mirror system, when the off-axis system is machined, it will have a significant role.

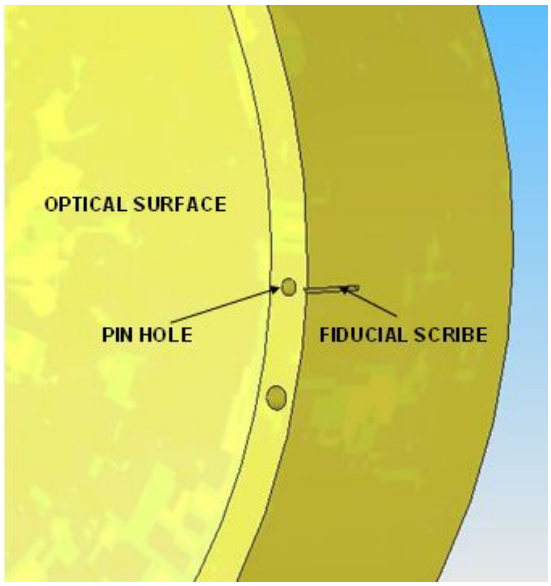

Figure 4. Clocking fiducial scribed in relation to pin hole.

Pins

The pins will be single-point diamond turned in 316 brass to reduce binding in the aluminum. The pins are toroidal, or barrel shaped as shown in exaggerated form in Figure 5. The overall diameter of approximately 2.3 mm is reduced by 20 µm at the ends of the pin. This will prevent binding due to misalignment, but still provide a positive fit when the pins are fully located in their holes. The two pins are turned with a diameter that is 3 µm smaller than the measured hole diameter at the waist, allowing for manufacturing tolerances. This allows for a 1 µm tolerance on the hole measurement and a 1 µm tolerance on the pin fabrication while still permitting a slip fit.

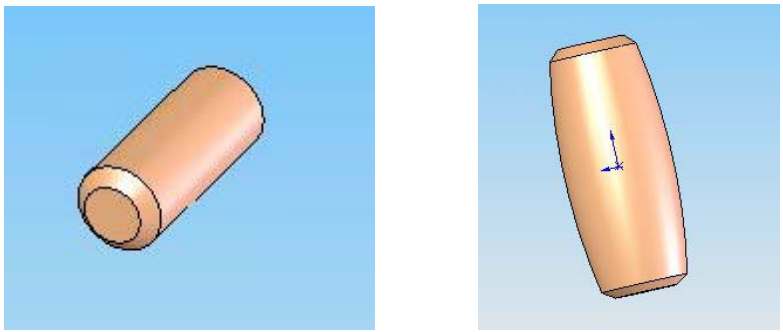

Figure 5. Locating pin for mirror-to-tube translation and clocking. Shown to scale at left and with exaggerated toroidal features at right (change in diameter is 20 µm).

Tube

The tube in Figure 6 supports the mirror and is approximately 100 mm in length and has a 178 mm OD. One end, the alignment test surface, has an optical surface machined into it to match the mirror surface: flat, spherical, or off-axis spherical. The first test will be with a flat surface.

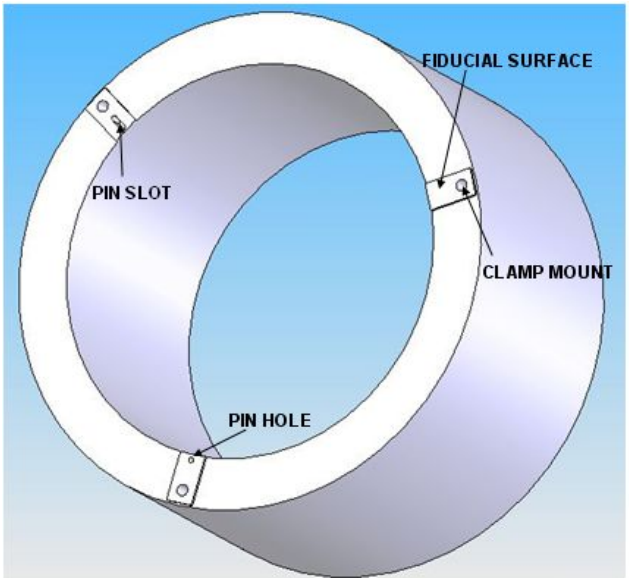

Figure 6. The mirror mounts on the end of the tube using the three fiducial surfaces. One surface has a hole and another has a slot to mate with the 2 pins in the mirror.

Figure 6 shows the mounting fiducial end of the tube. A pin hole and a slot mate with the pins inserted into the mirror without over-constraining the system. The pin hole and slot are bored and milled, respectively, with the same diamond boring tool used to put the two holes in the mirror. This ensures a uniform diameter using the same setup for both operations. Pilot holes were drilled because the boring tool will not cut to the center.

In the machining operation, one of the last steps will be to scribe a fiducial mark on the pad with the pin hole. The clocking location of the pin hole will be determined just as with the mirror, i.e. by touching the diamond tool to a pin inserted in the hole.

Clamps

A set of clamp mounting holes reside immediately outside the mirror contact area on the fiducial surfaces. Near the OD of the tube, the fiducial surfaces are squared off to mate with the clamps and prevent them from rotating. After examining a series of different clamp designs, it was decided that in the interest of flexibility, and adjustable spring plunger in an aluminum support would be appropriate for holding the mirror to the tube. Spring plungers are readily available in

a variety of force ranges and are rugged as well as inexpensive. As shown in Figure 7, the spring plunger is held by an L-shaped support that will be screwed to the tube. Using this arrangement, a variety of retaining forces can be explored as well as their impact on distortion of the system and any alignment errors they may introduce. In a complete system, these spring plungers would be replaced by wirecut EDM machined flexures to save mass and eliminate the need for adjustment.

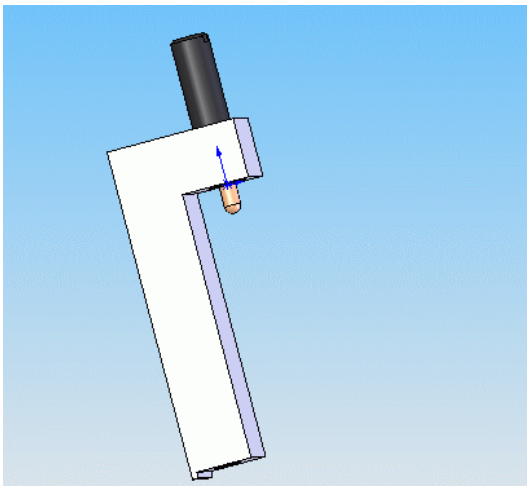

Figure 7. Spring plunger clamp used to retain mirror to tube.

5.3.1 ASSEMBLY PROCEDURE

The completed assembly is shown in Figure 8. The assembly procedure is as follows:

- Insert pins into mirror pin holes. Pins must slide completely into the holes.
- Place mirror on inverted tube and align pins in mirror with pin and slot in tube. Gentle pressure should drive the mirror home so that the fiducial surfaces on the mirror and tube mate.
- Bolt spring plunger clamps onto tube with spring plunger backed away from the mirror.
- Turn spring plungers until the make contact with the mirror, then turn to achieve the desired clamping force.

Stress Relieving was performed by Carolina Heat Treat according to the following procedure that was repeated twice.

- Cool the parts to -100°F and slowly warm to room temperature.
- Heat the parts to 300°F and slowly cool to room temperature.

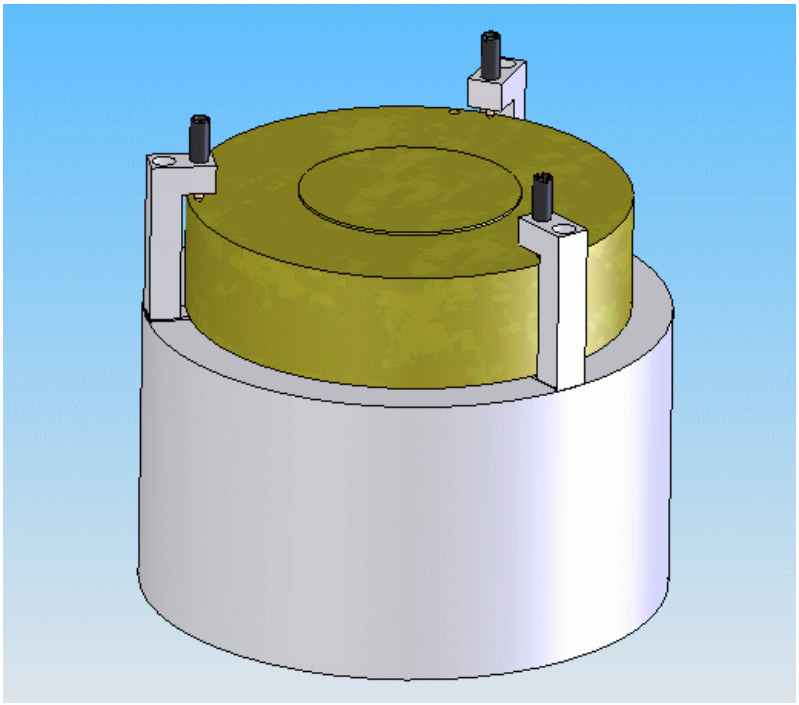

Figure 8. Completed test assembly shown from the rear. The spring clamps are bolted into their locations and the plungers can be adjusted to apply different loads to the rear of the mirror.

Flycutting tube fiducials The three fiducial pads on the tube are the first item that must be machined with a diamond tool. A .519 mm radius tool is mounted on the periphery of an aluminum plate and vacuumed onto the ASG 2500 DTM's main part spindle. The tube is held on a V-block by means of a bolt through the side of the tube. A 3/8" diameter hole was drilled through the side of the tube for this purpose. The tube was then squared by its exterior to the axes of the machine as shown in Figure 9. Variation along the tube length was less than .010 mm in both the y- and x-directions. The flycutter was then rotated at 500 rpm to make 20 passes at .025 mm each to completely machine all three pads. A finish pass at 5 mm/min should produce a 24 nm PV theoretical surface finish.

Turning mounting plate Due to the raised areas of the fiducial pads, the mounting end of the tube cannot be vacuumed onto the part spindle to machine the other end. An intermediate mounting plate must be used. With three holes to bolt the pads on the tube, the plate is simply an 8" diameter, ¾" thick flat. The back of this plate has been lapped. Prior to machining the front, the vacuum chuck was faced. Figure 10 shows the plate being faced.

Figure 9. Tube mounted on a v-block is squared to the axes using an electronic indicator. The flycutter can be seen on the part spindle behind the tube.

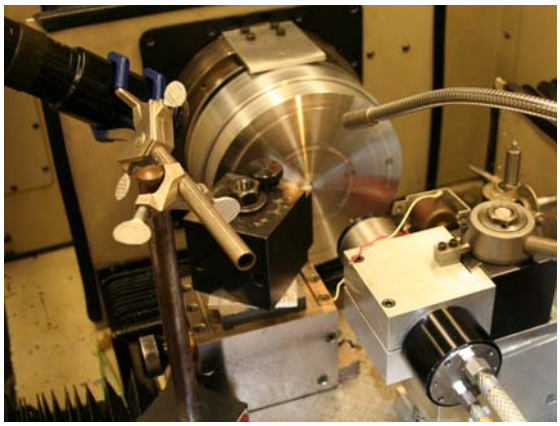

Figure 10. Tube mounting plate being faced. The plate is rotating on the spindle while material is being removed with the tool mounted on the micro-height adjuster The boring spindle is in position in the lower right.

Facing off tube The error correction for yaw of the z-slide was set to parameters of yaw = 0.70 arcsec at z = 1.2 mm. With the tube bolted to the mounting plate, the opposite end of the tube can be machined to an optical finish using a 1 mm radius tool.

Center boring spindle The pin holes are fabricated with a small-diameter diamond boring tool mounted in a Federal/Mogul Westwind high-speed grinding spindle. To find the location of the center of the boring tool with respect to the DTM coordinate system (and hence the mirror and tube) the boring spindle and the ASG 2500's part spindle must be aligned. The simplest way of achieving this goal is to bore a hole in a test part and then measure the runout of the hole with respect to the part spindle. When the two spindles are perfectly aligned, the runout is zero.

As shown in Figure 11, the boring spindle is driven by a small electric motor via an o-ring drive. This is necessary since the only tool available was made for clockwise rotation while the air turbine on the spindle rotates counterclockwise. The small DC electric motor reaches its maximum speed with 15 V. After locking the part spindle, the boring tool is plunged into a pre-drilled 1.8 mm diameter hole at 2 mm/min to a depth 3 mm. The setup is shown in Figure 11. Once the test hole is bored, an electronic indicator probe is placed inside the hole to measure the runout of the hole as a function of part spindle position. A sample plot of one of these measurements is shown in Figure 12.

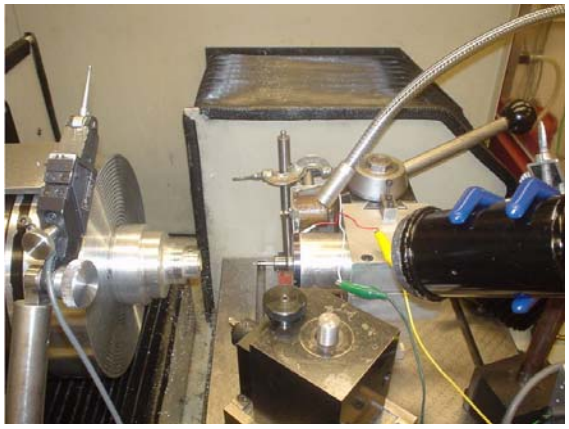

Figure 11. Boring tool mounted in high-speed spindle is used to bore a test hole in the part mounted on the spindle at left. The runout of the hole is measured with an electronic indicator.

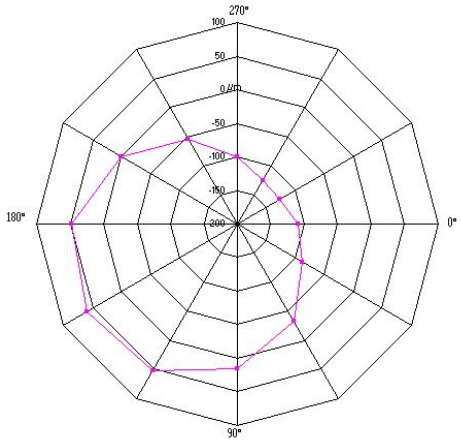

Figure 12. Boring tool centering. The measured runout from the procedure in Figure 5-41 shows that the boring tool center is 52 µm low and 80 µm left of center.

From the displacement of the probe at 0 and 180, the horizontal (x) position is obtained while from the displacements at 90 and 270 degrees, the vertical (y) error is obtained. To correct for x-error, the x-axis offset is changed. To correct for y-error, the spindle must be physically moved by the inverse of the measured error using the tool height adjuster on the toolpost. The centering process may have to be repeated to obtain minimal runout. Final runout measurement should be less than 1 µm.

The test holes bored for the centering process are also used to determine the diameter of the bored hole. As measured on the NewView 5000 Scanning White Light Interferometer, the hole diameter is 2.3587 ± 0.001 mm. This value is then used to determine the diameter of the pins. The NewView was calibrated using a reticle scale and found to be within ±.0005 mm.

Machine Pins The pins are single-point diamond turned from alloy 360 brass to reduce galling in the aluminum. A small radius tool (0.519mm) is used to turn the pins. First, a cylindrical pin is turned to accurately center the tool. The end is faced and the center feature used to adjust vertical centering. The OD of the pin is then turned and measured in the NewView 5000 SWLI, so that even if systematic error exists in the instrument, the same method for measuring pin and hole diameter should ensure that the final clearance is correct. This allows for a 1 µm tolerance on the hole measurement and a 1 µm tolerance on the pin while still allowing a slip fit. Figure 13 shows one of the pins being machined and measured.

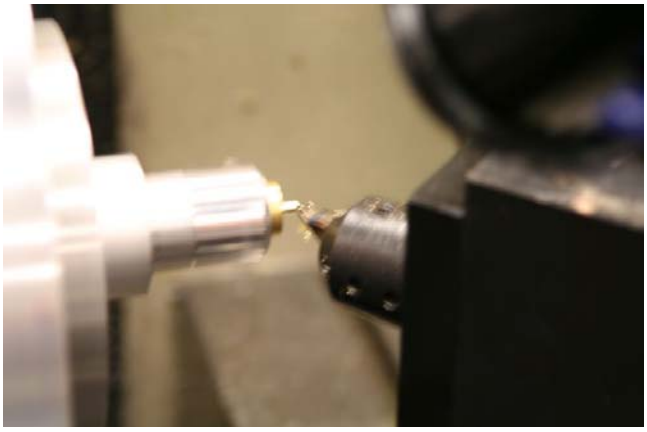

Figure 13. One of the brass pins being turned and the length measured.

Once the tool center was established, the toroidal pins could be fabricated. The diameter of the pins is reduced by 20 μm at the ends while the diameter at the center is 2.357 mm, approximately 2 μm smaller than the holes. The pins are turned while attached to a piece of brass rod about 20 mm in length. After the ends are faced, the toroidal profile is cut and a small chamfer turned at the end. The pin is then cut off in a conventional lathe using a modified box cutter blade as a cutoff tool. The pins are then approximately 0.2 mm long. After being cut off, the length is measured using a micrometer. The pins are then inserted into one of the test holes and faced to length and chamfered.

Pin hole and slot To bore the pin hole and slot, the existing rough machined hole and slot must be located. This turned out to be a particular challenge because the hole and slot did not appear to be registered to either the ID or the OD of the tube. So, to find the center of the coordinate system of the pin hole and slot, it was assumed that the spring clamp mounting holes were machined in the same setup. Hence, an 8-32 screw was threaded into each of the mounting holes and the tube, mounted on the vacuum chuck and centered on these three screws. The boring spindle was then moved to the correct radius for the pins and a machine-mounted microscope was used to align the hole in the clocking (θ) direction. Alignment with the slot was then checked at 120º from the hole and was found to fall within the existing rough slot. With the part spindle locked at 120º, the slot was then cut by plunging into the part at 1 mm/min to a depth of 3 mm and then translating 1 mm at 1 mm/min. The tool was then retracted at the opposite end of the slot. The part spindle was rotated back to 0º, locked and the pin hole bored to a depth of 3 mm. Figures 14 and 15 show the holes being bored.

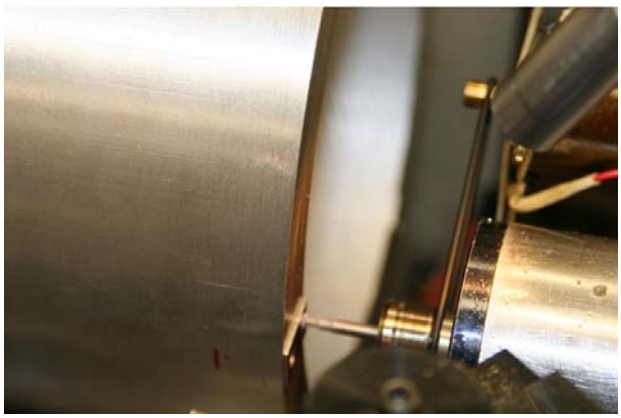

Figure 14. Pin hole being bored. Note belt drive on spindle to provide CW rotation

Figure 15. Closeup of pin hole being bored. View is through the on-machine microscope.

Center finishing tool The 1 mm finishing tool must be centered in both x and y to ensure that the contour of the spherical surface is correct and that the fiducial scribe marks are in the correct place. The tool was centered using a 12.7 mm diameter brass center plug. A centering error in the tool will produce both an ogive error (X-center) and a small feature at the center of the part (y-error). This centering technique is well established [*]

Machine mirror The mirror blank is placed on the vacuum chuck and centered as well as possible on the O.D. The mirror OD was turned with the pin tool to get a round part. Next the pin tool was used to rough cut the face of the mirror and remove most of the material. To get the best surface finish, a feedrate of 0.5 mm/min at 500 rpm and a DOC of 1 μm was used. This gives a theoretical PV surface finish of 0.1 nm. The finishing operation is shown in Figure 16.

Bore pin holes Chamfers were included at the edge of the mirror pin holes to keep burrs around the hole from preventing contact between the mirror and the tube. With the mirror chucked to the spindle and the tool centered, the part is centered using an electronic indicator. The boring spindle is then placed at the correct radius (83.5 mm) and the spindle is positioned so that, using the on-machine microscope, the boring tool will coincide with the existing hole. Alignment is then checked with the other hole by repositioning the spindle 120º. Maximum clocking accuracy on this DTM is 20000 counts per rev or 22 μm at this radius. Each hole is then bored at a feedrate of 1 mm/min in z to a depth of 3 mm.

[*] M. Gerchman. Fundamental axial spindle motions and optical tolerancing. SPIE 1573, 49-52 (1992).

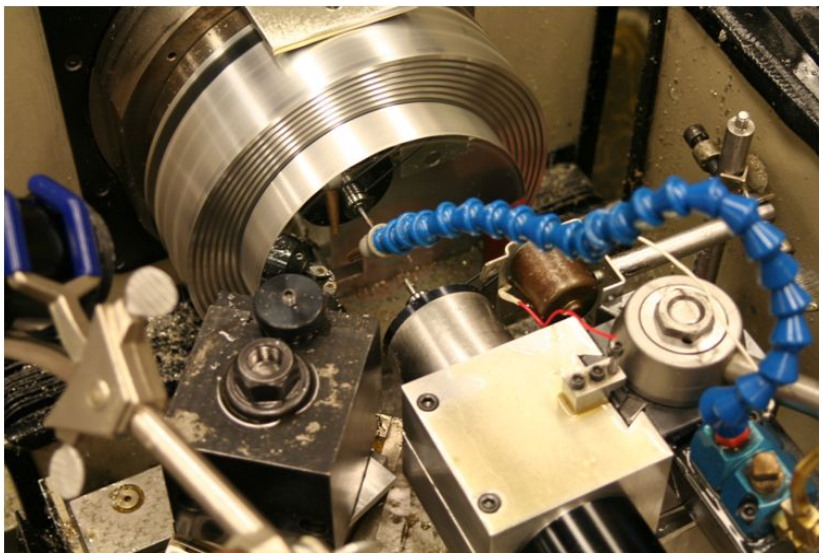

Figure 16. The finishing operation of the flat mirror.

Scribing fiducials With the part still mounted and the spindle in the +120º position, the optical figuring tool is moved to the OD of the part, brought into contact with it and dragged along the OD producing a mark. This will be the clocking fiducial that will test the clocking alignment. The tube is mounted on its face on the vacuum chuck with the straight pin that was used to center the pin tool inserted into the hole in the tube,. With the optical figuring tool positioned at 83.6 mm, the spindle is then rotated counterclockwise until the straight pin rests on the rake face of the tool. This position represents the OD of the pin. To center the tool on the pin in the θ-direction, the spindle is rotated another .808º. The face of the fiducial is then scribed with the optical figuring tool.

Assembly The toroidal pins are inserted into the mirror until they reach the bottom in their holes. Care must be taken to insert the pins straight into the holes. Thermal expansion is not a significant issue due to the small diameter of the pins. At this point, the mirror can be laid on top of the tube and, with the pins aligned with the hole and slot, gently pushed together. The spring clamps are then attached and tensioned to provide the appropriate retaining force.

5.4 METROLOGY

5.4.1 SURFACE FINISH

Preliminary measurement results for the fabricated flat show excellent surface finish results. The rms surface finish ended at 6 nm measured over a .11 X .14 mm area with the PEC's Zygo NewView 5000 white-light interferometer. Results are shown in Figure 17. Such a surface finish is quite good for 6061 aluminum as inclusions of iron and silicon preclude any improvement over this value for a diamond-turned surface.

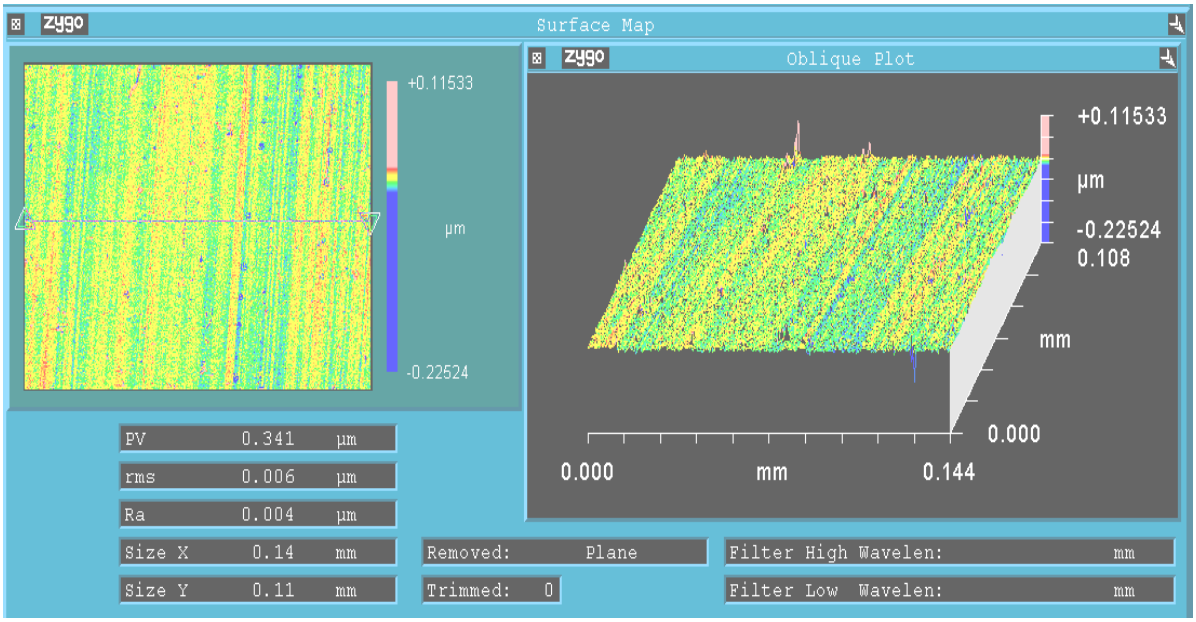

Figure 17. Surface finish measurement results from the Zygo NewView 5000 optical profilometer. While the tool marks are still apparent on the surface, the overall rms finish 6 nm is excellent for 6061 Aluminum.

The calculated surface finish for this mirror was 0.1 nm P-V, though the material effects and machine vibrations make this finish impossible to achieve under the conditions. Figure 18 shows a cross-sectional plot perpendicular to the lay of the surface. No regular tool marks can be discerned at the 1 µm theoretical crossfeed. This confirms that the range where tool geometry and machining parameters no longer determine the finish, but material effects and vibration do.

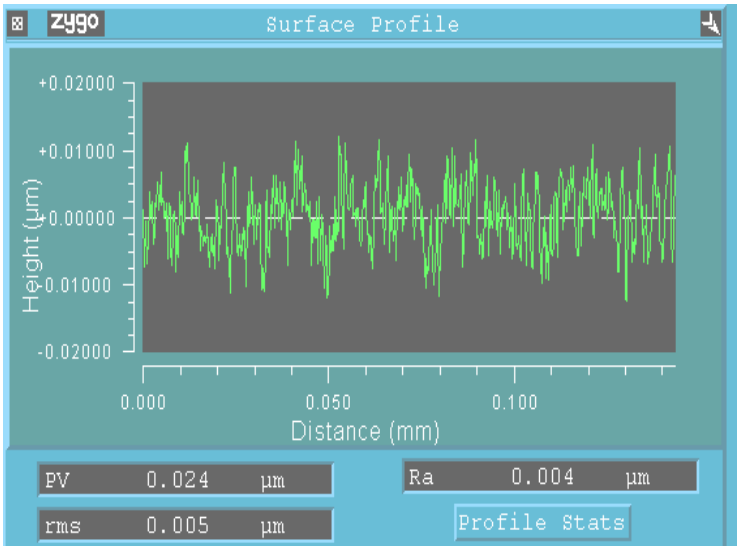

Figure 18. Cross-sectional trace of 3-D plot shown in Figure 17 shows no regular tooling marks, showing that the surface finish is dominated by material effects and machine vibrations.

5.4.2 SURFACE FIGURE

Surface figure measurements for the first cut of the flat are shown in Figure 19. The cut was made with the ASG 2500's geometric error compensation activated. This error compensation scheme compensates for errors due to X-axis straightness, Z-axis yaw and squareness between the two axes. The squareness compensation is part of the Z-axis yaw compensation and represents the intercept of the yaw curve. This value must be periodically updated if the spindle or axes have been moved on their mountings. Some residual squareness error is shown in the measurement as a conical component of the cross section. Independent measurements of the cone angle of a freshly faced vacuum chuck verified the squareness error. The cone angle was measured and found to be 2.0 arcsec. This cone angle is double the squareness error, so the current value of 0.7 arcsec squareness compensation was increased to 1.7 arcsec. A final cut of the flat surface is shown in Figure 20, showing 32 nm of RMS figure error. The residual error is possibly due to uncompensated roll or yaw errors in the x-axis.

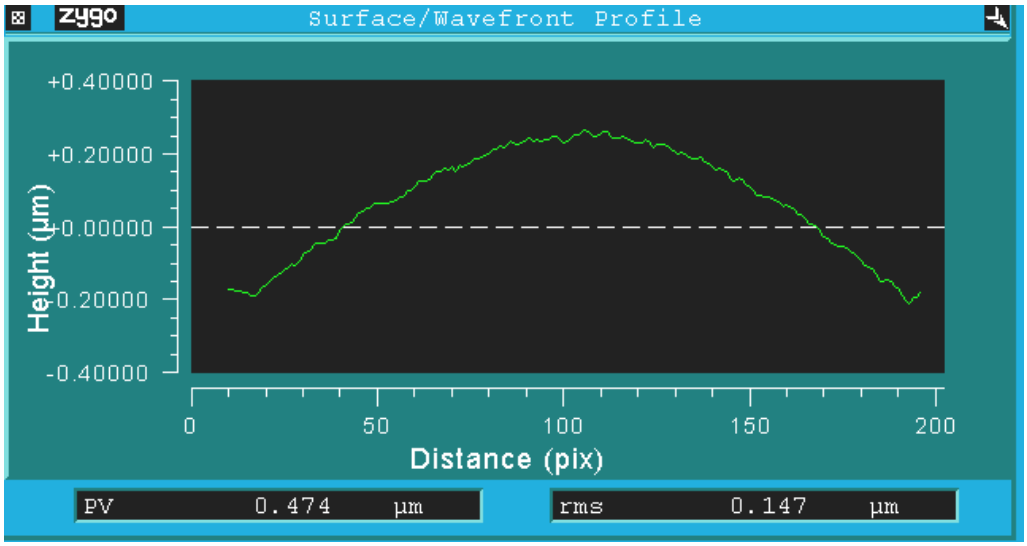

Figure 19. Surface figure measurement of 150 mm diameter aluminum flat before correcting 1.0 arcsec squareness error.

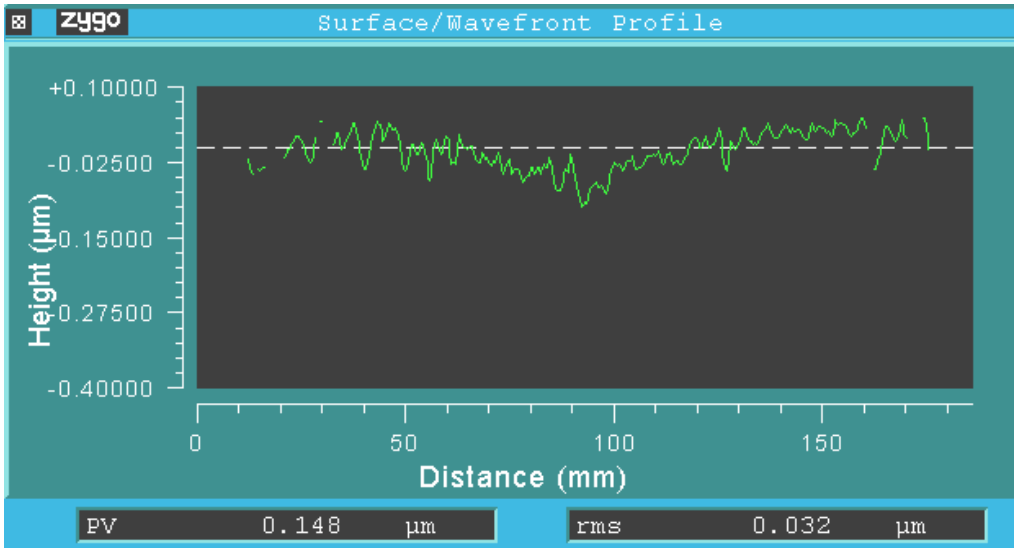

Figure 20. Surface figure of flat cut after removing for 1.0 arcsec squareness error.

5.5 CONCLUSION

The optical assembly test described here has revealed a number of challenges in fabricating a complete optical system. Fiducial design and location to reduce overconstraint but still provide a rigid mounting can be achieved through optimization of mechanical structures using finite element modeling. Fabrication considerations such as mounting components during machining are pivotal to achieving a high degree of accuracy in fabrication. Often, in complex, multicomponent systems, these considerations are obscured because of the large number of variables. As work progresses on this simplified test system, further nuances in the assembly process will be revealed.

This page intentionally left blank.

6 ELLIPTICAL VIBRATION-ASSISTED MACHINING

David Brehl
Graduate Student
Thomas Dow
Professor
Department of Mechanical and Aerospace Engineering

6.1 INTRODUCTION

In Elliptical Vibration-Assisted Machining (EVAM) a diamond tool is driven at high frequency through a tiny ellipse superimposed on the main work feed motion. EVAM avoids problems of tool deflection, chatter, runout and burring, which limit the feature resolution and tolerance achievable with other chip-making processes like micro-milling. Previously, the Ultramill EVAM tool was used to machine binary microstructures. Current work now emphasizes fabrication of microstructures with sculpted 3-D surfaces and high-aspect ratio features. To make these parts requires developing motion programming methods for producing non-planar surface profiles, being able to position the tool tip precisely at specified coordinates, and use of diamond tools with sharp-nose geometry rather than the round-nosed tools used to date.

6.1.1 PROCESS DESCRIPTION

Figure 1(a) shows the principal of operation for the Ultramill EVAM tool. Sinusoidal voltages are applied to two parallel piezoelectric actuators, causing them to change length in a cyclical manner. The toolholder acts as a linkage to convert the linear stack motion into an elliptical tool path. Figure 1(b) shows the tool motion in EVAM for two cutting cycles. During each cutting cycle, the work advances relative to the elliptical tool path. The overlapping toolpaths produce thin chips, resulting in greatly reduced tool forces compared to conventional cutting. The Ultramill is installed on a 3-axis diamond turning machine (DTM), which provides XYZ motion for raster machining.

If the depth of cut (DOC) is equal to or smaller than the length of the semi-minor axis of the toolpath ellipse, the tool exits the workpiece each cutting cycle. Small, discontinuous chips are created. This results in near-zero burr formation on the end and side edges of the cut. When DOC exceeds the semi-minor axis of the toolpath ellipse the tool still breaks contact with the uncut material during each cycle, but a long continuous chip is formed that remains attached to

the workpiece. To create features with a significant dimension in the depth direction, roughing passes can be made at a DOC larger than the semi-minor axis of the tool path ellipse. This economically achieves most of the required material removal. A finish pass is then made with DOC smaller than the ellipse semi-minor axis, to complete the part with burr free edges, excellent surface finish, and sub-micrometer feature tolerance.

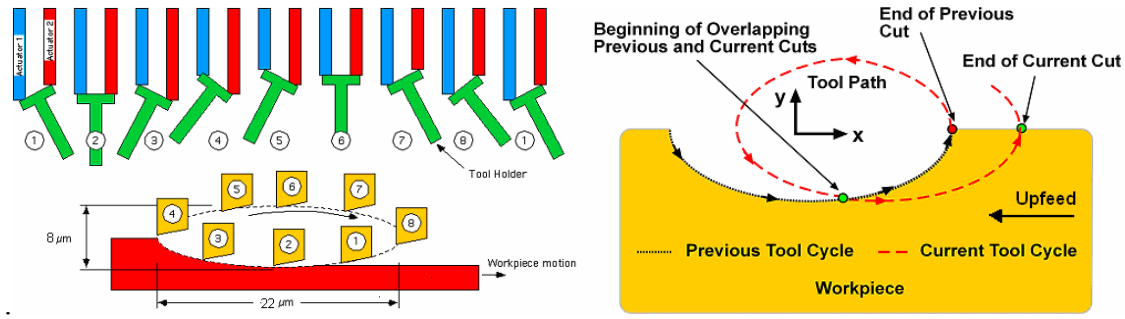

(a) (b)

Figure 1. (a) Ultramill concept. (b) EVAM showing two successive elliptical cycles.

6.2 MICROSTRUCTURE FABRICATION

6.2.1 MICROCONTACTOR PINS

Figure 2 shows the internal contactor elements of a microrelay. The contactor pins are 160 μm in diameter and made of a gold/glass matrix composite. To increase device reliability, the groove pattern depicted in Figure 3 will be machined into the pins. These grooves provide clearance for particles that could otherwise interfere with the operation of the switch. The groove pattern has a sinusoidal profile in the upfeed direction with an amplitude of 2 μm. The individual grooves are 5 μm deep with a sinusoidal section in the cross feed direction and an aspect ratio greater than 0.5. As illustrated in Figure 4(a) these small-scale, high-aspect grooves require a sharp-nosed tool with included angle of 40˚.

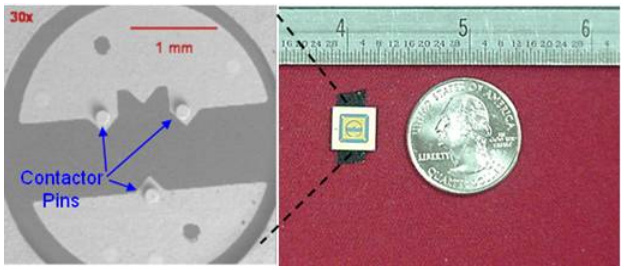

Figure 2. Contactor Element for Microrelay.

The motion program used by the DTM describes the motion of the center of the elliptical tool path. Figure 4(a) shows that in the crossfeed direction, the offset between tool path center and surface profile remains constant. In the upfeed direction, the offset between surface and toolpath

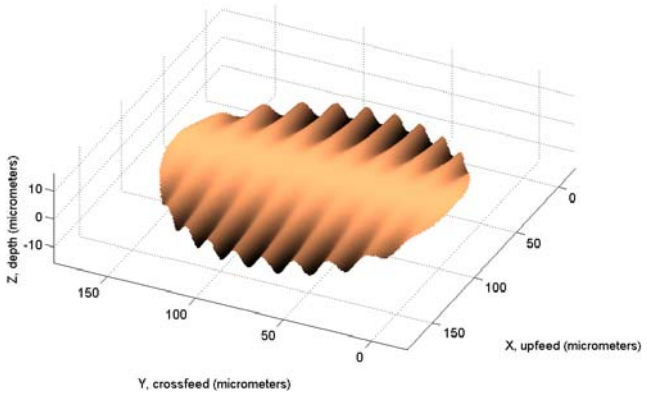

Figure 3. Groove pattern to be machined into contactor pins.

center varies, depending on the ellipse geometry and the instantaneous slope of the surface profile. Figure 4(b) depicts the contact point X, Z on the toolpath ellipse tangent, and their relationship to the surface. Offsets (ΔX, ΔZ) from the contact point and the ellipse center point location (X_E, Z_E), are calculated from the ellipse geometry and the tangent slope t:

$$\Delta X = \frac{\pm t a^2}{\sqrt{a^2 t^2 + b^2}} \qquad (1\text{-a}) \qquad\qquad \Delta Z = \frac{-b}{a} * \sqrt{a^2 - (\Delta X)^2} \qquad (1\text{-b})$$

$$X_E = X - \Delta X \qquad (2\text{-a}) \qquad\qquad Z_E = Z - \Delta Z \qquad (2\text{-b})$$

The tool path to be programmed is the locus of all such points (X_E, Z_E) for the upfeed profile. The tool tip must be accurately positioned center the groove pattern on each pin. Procedures for this are developed in the next section.

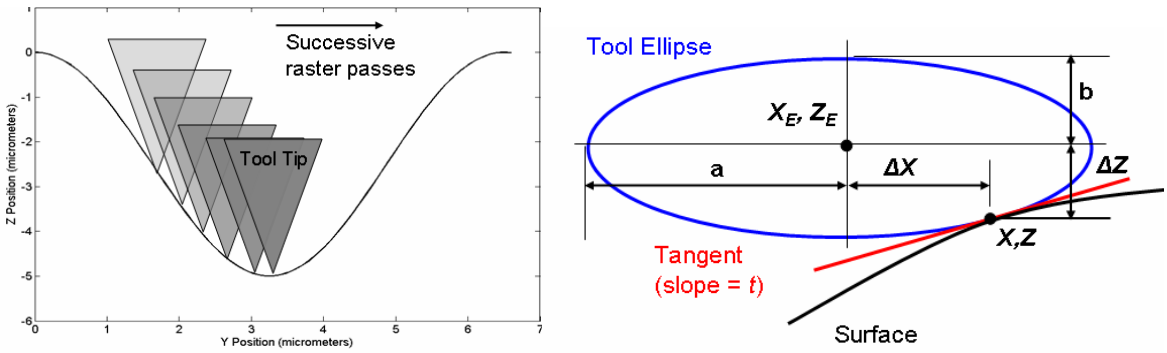

(a) (b)

Figure 4. (a) Sharp-edge tool used to make grooves with sinusoidal crossfeed profile. (b) Tool offset determination for motion programming in upfeed direction.

6.2.2 PRECISION X-Y-Z TOOL POSITIONING

A 220x video-microscope has been installed on the Y-axis to determine the position of the tool tip (Figure 5(a)). The microscope moves with the Y axis along with the Ultramill, maintaining a fixed relationship between them. Figure 5(b) shows how the video-microscope is used to position the tool tip at desired X and Y coordinates. The video-microscope camera provides a plan view of the part. The X and Y axes are moved to place the camera crosshairs at the desired location on the part image. The axes are then jogged through an offset distance ΔX and ΔY which positions the tool tip at the desired location.

These offsets between tool tip and camera fiducial are determined during setup by using the Ultramill to plunge-cut a feature at reference position X_C, Y_C as illustrated in Figure 6. The feature is brought into view on the video-microscope display. The locations X^+, X^-, Y^+ and Y^- are determined by positioning the crosshairs at the respective feature endpoints and reading the coordinates on the DTM controller display. The offsets ΔX and ΔY are then calculated using the definitions in Figure 5. Measuring the position of feature endpoints is more accurate than attempting to align the crosshairs with the estimated location of X_C and Y_C in the feature image.

Positioning the tool tip precisely in the Z (depth) coordinate ultimately reduces to accurately locating the work surface. The Y-axis video-microscope can be used to measure the width of a plunge-cut feature or short groove made at a reference point, as illustrated in Figure 7. The depth of cut *d* can be found for a sharp-nose (Equation 3) or round-nosed tool (Equation 4):

$$d = \frac{w}{2}\tan\left(90 - \frac{\psi}{2}\right) \quad (3)$$

$$d = \frac{2R - \sqrt{4R^2 - w^2}}{2} \quad (4)$$

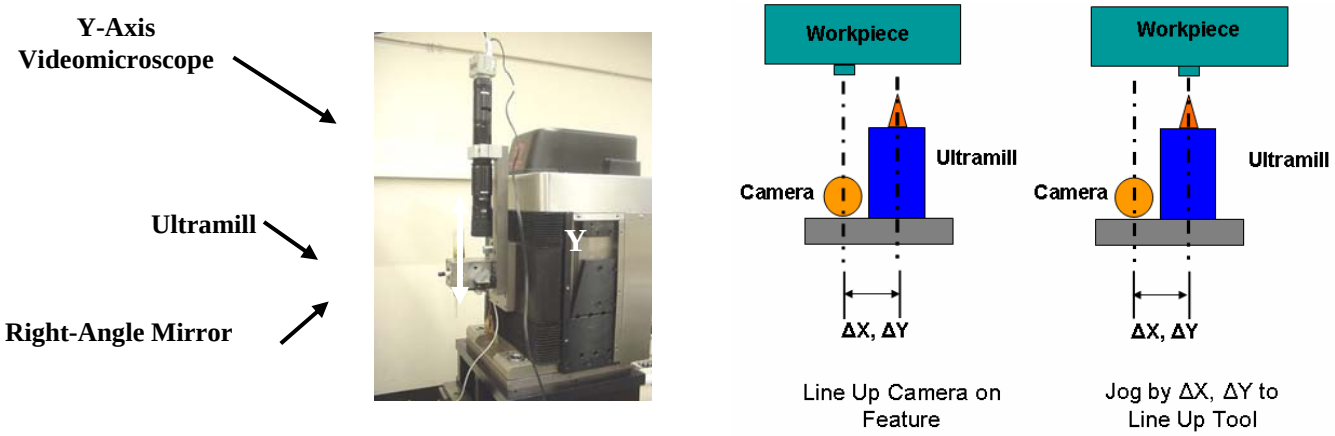

Figure 5. (a) Y-axis videomicroscope (b) Scheme of use

with *w* the measured width of the feature, ψ the included angle of a sharp-nosed tool and *R* the nose radius of a round-nosed tool. The calculated depth-of-cut can then be subtracted from the Z coordinate read from the DTM's controller, yielding the coordinate corresponding to the surface location.

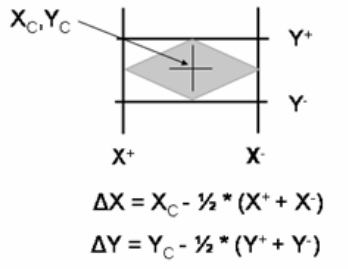

Figure 6. Determining offsets for Y-axis video-microscope. (Feature made by sharp-nosed tool is depicted.)

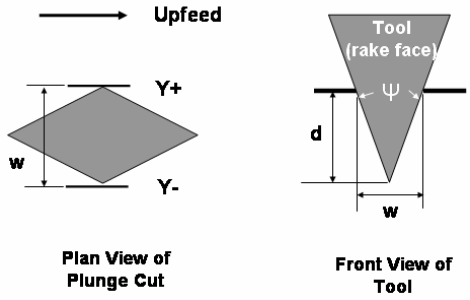

Figure 7. Determining depth-of-cut *d* width *w* of plunge-cut feature. (Feature made by sharp-nosed tool is depicted.)

6.2.3 TRIHEDRON ARRAYS

Experience with sharp-nosed tools was gained by machining trihedron arrays in hard-plated copper, oxygen-free high-conductivity (OFHC) copper, PMMA plastic, and 17-4 PH stainless steel. The features were 80 μm tall on a 112 μm side pitch. The sharp-nosed diamond tool had an included angle of 70.6˚, 0° rake angle, and 10° flank clearance angle. To make these parts, one set of parallel grooves was cut. The spindle was then manually rotated 60° and locked, using the bolt holes spaced around the circumference of the vacuum chuck. The spindle encoder (1,515,120 counts per rotation) was used to confirm the angle of rotation. The part translated in X and Y, as well as rotating, since it was located away from the spindle center. The tool was moved to compensate for this translation and a second set of parallel grooves machined. Another 60° rotation was made and the process repeated for the last set of grooves.

The accuracy of this fabrication sequence is sensitive to how precisely the spindle's center of rotation can be determined. In these experiments the Y-axis camera had a resolution of 5 μm per pixel which established the lower limit of precision for finding the spindle center. The offset caused by centering error was larger than offsets resulting from rotational positioning errors, which were usually <1.5 μm. The offsets produced small trihedrons between the main features. Figure 8 shows an extreme close-up view of one of these interstitial features. It is ~10 μm across, was machined from hard-plated copper, and shows no burrs or deformation at 4000x

magnification. The interstitial trihedrons are also visible in the wide angle images of the complete array, in Figures 9 and 10.

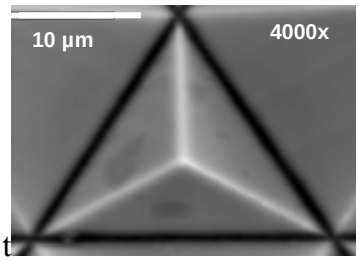

Figure 8. Interstitial trihedron caused by centering error. Hard-plated copper.

All parts were machined with an upfeed velocity of 10 mm/min, 1 KHz machining frequency, and 22 µm x 4 µm toolpath ellipse. The grooves were made using two different cutting schemes. The first, using "all deep cuts" consisted of 8 successive cuts each of 10 µm depth. The second, incorporating a "burr removal sequence", was composed of 7 cuts of 10 µm depth followed by one cut each at 4, 3, 2, and 1 µm. The last two cuts in the sequence were shallow enough to produce discontinuous chips and were intended to remove any burrs made during preceding material removal passes.

Figures 9 and 10 show wide-angle and close-up SEM images of trihedron arrays made in hard-plated and OFHC copper. The left-hand image of each pair shows the result of using "all deep cuts" while the right hand image shows the effect of the "burr removal sequence". Figure 9 shows that for hard-plated copper material (Vickers hardness = 300, measured with PEC hardness tester), slight burring occurred with "all deep cuts" but the "burr removal sequence" successfully produced burr-free features. Figures 10 shows results for OFHC copper (Vickers hardness = 111). A significant burr occurred on trihedron edges in the "all-deep cuts" case. The softness of the OFHC copper compared to hard-plated copper is believed to be the reason for burr formation in this part. The "burr removal sequence" left a small burr but is seen to be capable of a considerable degree of burr reduction.

The PMMA results were not imaged by SEM as the material blank would not fit into the microscope vacuum chamber. Under optical microscopy at up to 500x magnification, the trihedrons made in PMMA had a similar appearance to those made in plated and OFHC copper. This suggests that burring in PMMA was of the same extent as in the copper parts. Since the depth of field for the optical microscope is shallow compared to the overall height of the trihedron features, at a single focus position it is not possible to discern a full trihedron or subtle irregularities such as a burr, when it has a significant dimension in the depth direction.

Significant burring was observed in SEM images of trihedrons machined in 17-4 stainless steel (Vickers hardness=220). These were machined at the same conditions used for the copper parts, and also at a frequency of 1200 Hz with a 27 μm x 5.1 μm ellipse. An explanation has not yet been developed for the appearance of burr on these parts. By itself, workpiece hardness does not serve as an adequate predictor, since the two types of copper were harder and softer than the stainless steel, and effective burr reduction was achieved in both of them.

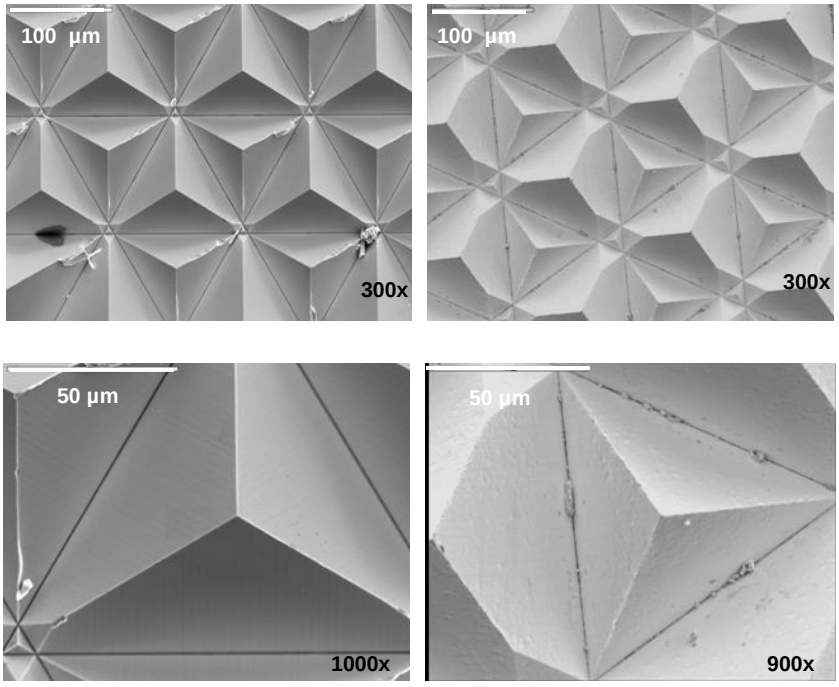

Figure 9. Trihedron arrays in hard-plated copper. *Top* Wide-angle view of array. Note interstitial features due to centering error. *Bottom* Close-up view of 80 μm feature. "All deep cuts" on left side, "Burr removal sequence" on right.

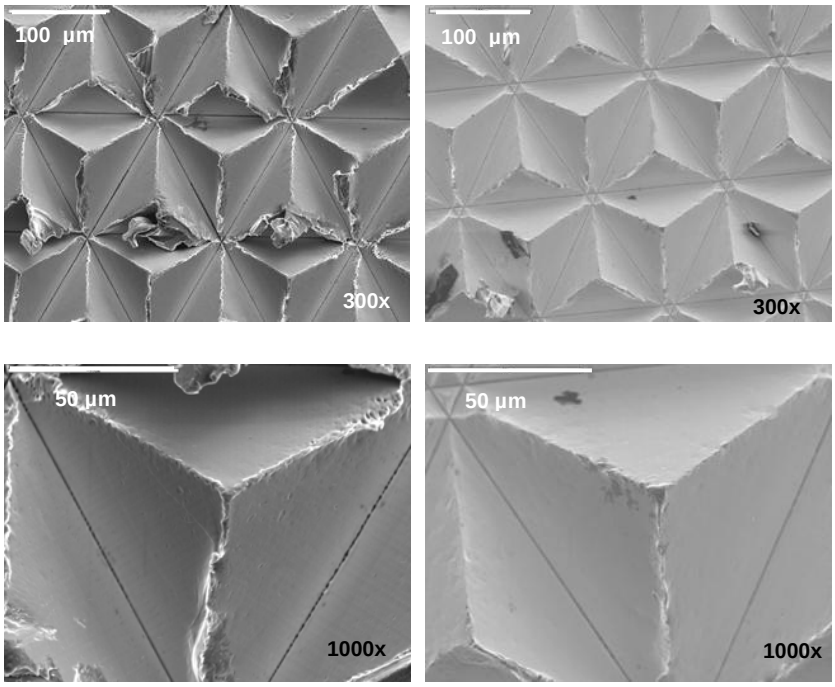

Figure 10. Trihedron arrays in OFHC copper. *Top* Wide-angle view of array *Bottom* Close-up view of 80 µm feature. "All deep cuts" on left side, with significant burr apparent. "Burr removal sequence" on right greatly reduced burr on feature edges and also at a frequency of 1200 Hz with a 27 µm x 5.1 µm ellipse. An explanation has not yet been developed for the appearance of burr on these parts. By itself, workpiece hardness does not serve as an adequate predictor, since the two types of copper were harder and softer than the stainless steel, and effective burr reduction was achieved in both of them.

6.3 CONCLUSIONS

A video-microscope camera was installed on the Y-axis, allowing accurate positioning of the tool tip at specified X and Y coordinates. Plunge-cut features made with a tool of known geometry can be measured to accurately find the work surface for precision Z-coordinate positioning. Camera resolution is presently 5 µm and must be improved in order to achieve micrometer-scale features.

Complex groove patterns are to be machined onto microcontactor pins, to demonstrate EVAM's ability to produce features with sculptured 3-D surfaces, 5 µm scale, and aspect ratios > 0.5. A

sharp-nosed tool will be used to make these features. Equations were developed for calculating toolpath center offset for machining sculpted upfeed profiles.

Trihedrons 80 μm tall and 10 μm tall were machined in hard plated copper and softer OFHC copper using a sharp-nose tool. A combination of deep roughing cuts for material removal and shallow finishing passes was effective in eliminating or reducing burrs on feature edges. Trihedrons machined in 17-4 stainless steel showed significant burr.

6.4 ACKNOWLEDGEMENTS

Principal funding for this work is by National Science Foundation grant DMI-433215, monitored by G. Hazelrigg. Additional support by Sandia National Laboratories (microcontactor project in Section 6.2.1) and Oak Ridge National Laboratory (trihedron arrays in Section 6.2.3).

This page intentionally left blank.

7 METROLOGY ARTIFACT DESIGN

Thomas Dow
Professor
Department of Mechanical and Aerospace Engineering
Kenneth Garrard
Precision Engineering Center Staff
Karalyn F. Folkert
Consolidated Diesel Corp., Whitakers, NC

7.1 BACKGROUND

An artifact has been designed and built to assess the static and dynamic performance of a Coordinate Measuring Machine (CMM). CMMs can measure a wide variety of component shapes and have accuracy and repeatability comparable with most manufacturing operations. The Y-12 National Security Complex manufactures precision parts for the government and private companies. Part acceptance is generally based on dimensional inspection and comparison with tolerance specifications. The goal of this project was to design and fabricate an artifact that can be used to expose the measurement errors in a CMM due to static (error motion of slides, control system) and dynamic sources (following error, probe dynamics). With this information, a measurement strategy for a part shape can be developed that will limit the errors to an acceptable value. If the artifact includes a broad band of excitation sources, the measurement will show how the actual gauge motion is transformed by the dynamic environment to produce a new motion with amplitude and phase errors. A ring gage was found to be the best artifact geometry for Y-12 and the addition of small sine wave features allow both static and dynamic calibration.

7.2 RING GAUGE GEOMETRY

The ring gauge has a 200 mm OD, a 150 mm ID and a thickness of 25 mm. The material was 17-4 PH stainless steel, heat treated for maximum dimensional stability and electroless nickel plated. Diamond turned flat surfaces on the top and bottom as well as circular sections on the ID and OD can be used as a standard ring gauge to measure machine geometry and the effectiveness of control systems and error correction schemes. The OD and ID have raised sections on which a sine wave features were machined to measure the dynamic response of the machine and probe.

7.2.1 SWEPT SINE WAVE

The small features on the surface of the ring are designed to create a range of excitation frequencies to evaluate the response to a dynamic environment. A number of different geometries were investigated and the best candidate was a swept sine wave with constant amplitude. A swept sine wave is a sine wave with a continuously varying wavelength; that is, each point on the swept sine wave has a different wavelength. For the ring gauge, the wave begins at a long wavelength and progresses to a short wavelength in the first 90 degrees. To produce a continuous wave, the wave is "flipped" to line up with the last wave and then the wavelength increases to the starting point as it reaches 180 degrees. From 180 to 360 degrees, the wave is a mirror image of the first 180 degrees. Four quadrants of the same wavelengths allow a smaller section to be measured. Figure 1 illustrates these features.

The allure of the swept sine wave is that it contains a wide range of wavelengths and thus excitation frequencies. Different measurement speeds change the frequency range for the transfer function while the spatial wavelength remains the same. The linear swept sine wave from 0º to 90º is given by Equation 1 where A is amplitude, t is circumferential distance, d is the modulation parameter and f is the base wavenumber. The total number of waves over length L is d+f.

$$y = A \cdot \sin\left(\frac{2\pi t}{L}\left(\frac{d}{L}t + f\right)\right) \qquad (1)$$

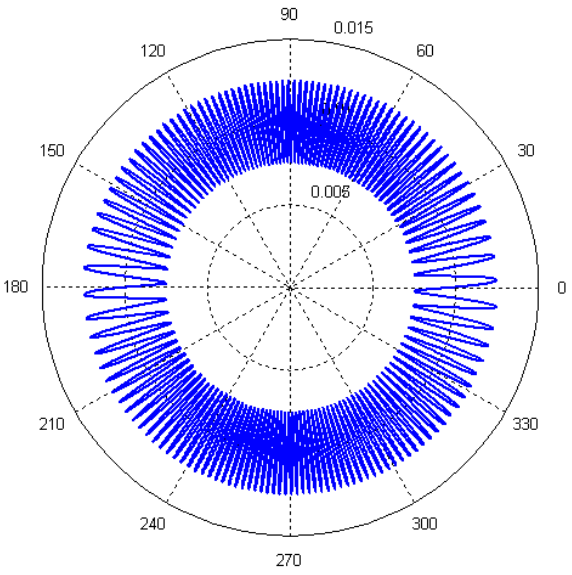

Figure 1. A continuous swept sine wave in polar coordinates.

7.2.2 SWEPT SINE WAVE EXCITATION

The swept sine wave creates a frequency-rich environment that reveals the dynamics of the CMM, its ability to respond to small surface anomalies and the performance of the CMM as it traverses the varying wavelength features. The values of the swept sine wave were selected based on desired minimum and maximum spatial wavelength. Because the wavelengths can be considered as individual frequencies, a Fourier transform can be performed on the data set. With sampled data, the units on the frequency spectrum plot are in terms of Hertz.

However, with the generated spatial data, it ismore useful to plot the results in terms of wave number1. The wave number is the reciprocal of the normalized spatial wavelength. Figure 2 shows the FFT of the first quadrant of the ideal wave for the ID. The magnitude is largest near the shortest wavelength at wave number 223/λ which translates to a wavelength of 0.537µm. The phase values accumulate for half of the wavelengths and then returns to zero.

The FFT of the swept sine wave is more difficult to interpret than a single frequency sine wave due to the constantly varying nature of the wavelength. Rather than strictly interpreting the ideal FFT and directly comparing it to an FFT of an actual measurement, the data analysis may be simplified. A CMM has dynamic characteristics that will influence the overall measurement of the artifact and the ability of the probe to detect small perturbations changes with the radius of the probe, measurement speed, radius of the part and size of the feature.

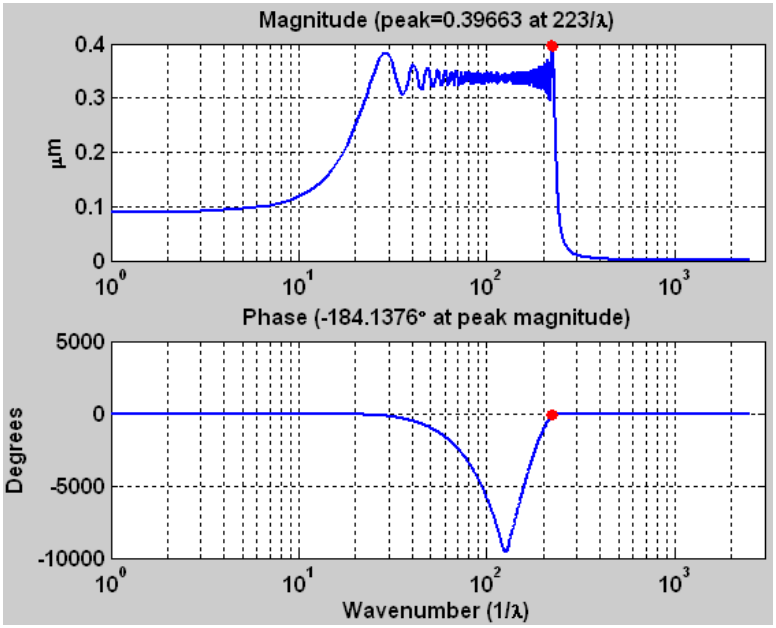

Figure 2. Spatial frequency spectrum of the first quadrant of the swept sine wave in Figure 1.

Since the swept sine wave on the surface of the ring has an 'accepted' value[2] and the CMM measurement will generate another data set, the CMM's dynamics, or transfer function, may be found by comparing these measurements using a form of deconvolution. Convolution in the time domain is the multiplication of the swept sine wave and the impulse response of the dynamic system to construct an output that shows the influence of these dynamics. Since the dynamics of the CMM are not known, the inverse of convolution, or deconvolution, is used; the

[1] The number of waves per unit distance (one quarter of the ring circumference).

[2] The actual swept sine wave may not be exactly equal to the designed shape.

CMM measurement is divided by the accepted swept sine wave. To expedite calculations, deconvolution may be executed in the frequency domain. The magnitude and phase components in the frequency domain are separated to create a Bode plot of the CMM's dynamics. Multiple measurements with different speeds can be used to create the desired frequency range of the Bode plot to determine the dynamics of the system. The transfer function of the CMM provides a significant amount of information about the machine. It specifies the natural frequency as well as the machine's performance within a frequency range. If a measurement speed is specified, the speed may be converted to frequencies present in the swept sine wave data and an appropriate CMM operating speed determined based on the transfer function and an acceptable amount of error.

7.3 ARTIFACT FABRICATION

A Fast Tool Servo (FTS) was used to machine the swept sine wave on the ring3. The piezoelectric stacks of the FTS are excited by the signal from a high voltage amplifier. The frequency and voltage signal affect the movement of the tool on the FTS. Feedback control from the built in cap gauge can correct for position error at low frequency. The closed loop controller uses position feedback with a proportional-integral control algorithm to correct position error. Gains are selected to shape the response of the system, to prevent overshoot and to correct for the following error. Although the system dynamics of the FTS are improved with closed loop control, there is still significant phase error in the system at higher frequencies. Since the FTS will operate at close to 600 Hz when machining at 20 rpm, deconvolution is applied to the swept sine wave before it is input into the controller. Deconvolution uses the magnitude and phase characteristics of the FTS with the information of the desired wave output to adjust the amplitude, phase and shape of the command signal; that is, it alters the input to produce an expected output4. This technique greatly decreases the error to about 300 nm in the fabrication of the swept sine wave.

7.4 CONTACTING PROBE MEASUREMENTS

7.4.1 DETERMINING PROBE DYNAMICS

The dynamic transfer function of the air-bearing probe depends on the dynamics of the probe/gauge interface contact and any filtering built into the cap gauge electronics. Typical air-

[3] K. Folkert, T. Dow, K. Garrard. Metrology Artifact Design. ASPE Proceedings, 34, 462-465 (2004).

[4] W. Panusittikorn. Error Compensation Using Inverse Actuator Dynamics. PhD Dissertation, North Carolina State University, (2004).

bearing probes capture some of the exhaust air and use it to preload the probe against the surface. This preload is a constant force independent of the deflection of the probe.

When confronted with the dynamic forces from the ring gauge motion, the probe will follow the surface until the dynamic forces exceed the preload and then it will leave the surface. The initial conditions, mass and damping will determine its motion and it will bounce when it returns to the surface depending on the relative speed and interface.

Electronic filtering will change the apparent position of the probe by reducing the amplitude and introducing phase lag. An example of the probe response when excited with a sine wave motion with and without the electronic filtering is shown in Figure 3. A preload of 3.4 grams keeps the 7.4 gram mass of the probe in contact until about 150 Hz. The filtered amplitude ratio (air-bearing probe motion divided by excitation) drops as expected and is down about 3 dB (0.707) and lags the input by 64° at 113 Hz due to the filter. If the filter is removed the bandwidth is 20,000 Hz and the probe measures the motion up to the acceleration limit of 150 Hz after which it 'bounces' and contacts the surface sporadically.

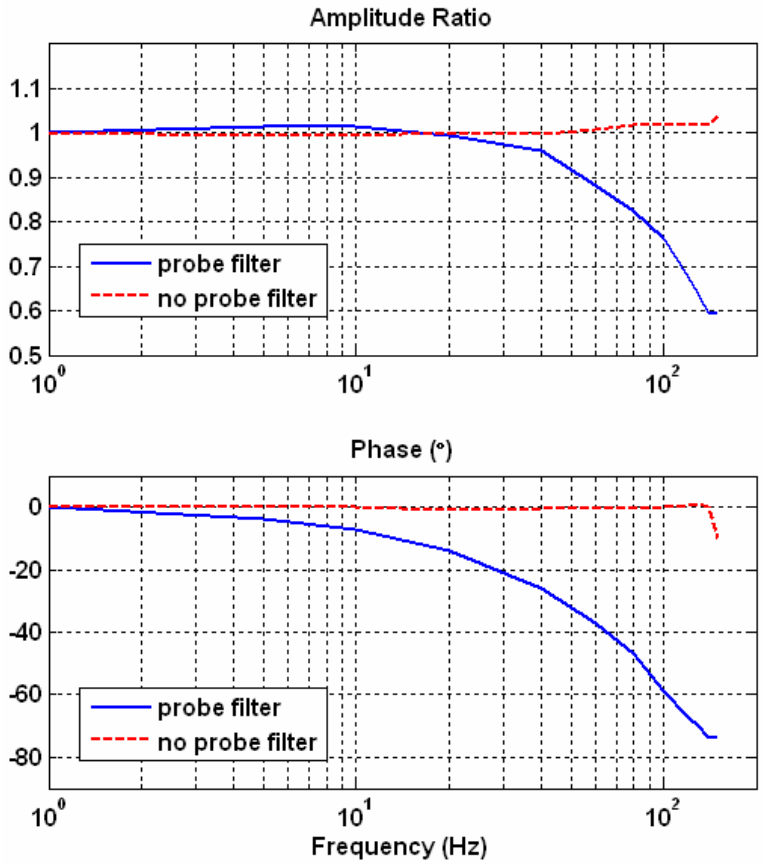

Figure 3. Transfer function of the air-bearing capacitance gauge with and without filtering.

The motion of the probe when it exceeds its acceleration limit will become a part of the dynamic measurement. This motion will depend on the dynamics of the probe (the friction, damping and spring constant) but not the shape of the part. A model of the motion of an air-bearing cap gauge was developed and corroborated by experimental measurements.

An example of the probe motion is shown in Figure 4 from an oscilloscope measuring probe and excitation motion at a constant 50 Hz. The preload was reduced in the right to allow bouncing. Because of the range of the cap gauge, there is a 2.5x gain difference in the two signals. Notice that the amplitude of the probe motion grows significantly when bouncing occurs but the frequency is much lower than the excitation. The response changes depending on the gauge velocity and direction when the probe contacts it.

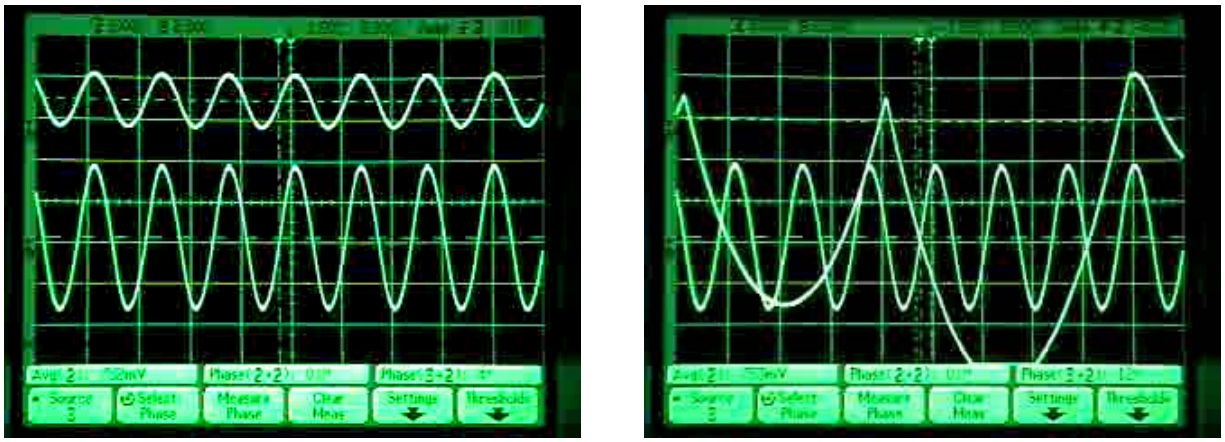

Figure 4. Motion of the probe (top) and gauge (bottom) in contact (left) and bouncing (right).

7.5 RING GAUGE MEASUREMENT

Measurement of the swept sine wave on the ring gauge (Figure 5) provides a rich dynamic input to assess the response of the structure, controller and probe of the CMM. The advantage of the ring gauge is that the entire CMM structural loop is included. This is also a problem because any bouncing behavior of the probe is measured.

As the probe moves from the low frequency region to higher frequencies, the magnitude and phase of the measured shape will be modified by the dynamics of the CMM. This change can be quantified by comparing the measured shape to the 'accepted' shape of the surface. However, the data must be modified before analysis to eliminate the non-contact regions. If the probe leaves the surface the observed system behavior will not be LTI (linear time invariant).

Figure 5. Setup of a CMM probe measurement of the swept sine waves.

An algorithm has been developed to compute the CMM/probe transfer function given the gauge shape, a measurement data set and the circumferential speed of the measurement. The algorithm detects probe bounce in the measurement signal and windows the data appropriately before performing a transfer function calculation in the frequency domain.

To demonstrate the capability of this measurement technique, the air bearing probe with and without the electronic filter was used to measure the ring gauge shape. The air-bearing preload was set for contact up to about 80 Hz and a linear sine sweep was sent through a FTS to the probe. The data was collected using XPC Target and a National Instruments 6052E multifunction board at a 20 kHz sample rate. The results are shown in Figure 6 and can be compared to the probe transfer function in Figure 3. Without the filter the probe behaves as expected with unity gain and flat phase response until it loses contact. Attenuation and phase lag with the probe filter are in good agreement up to about 50 Hz.

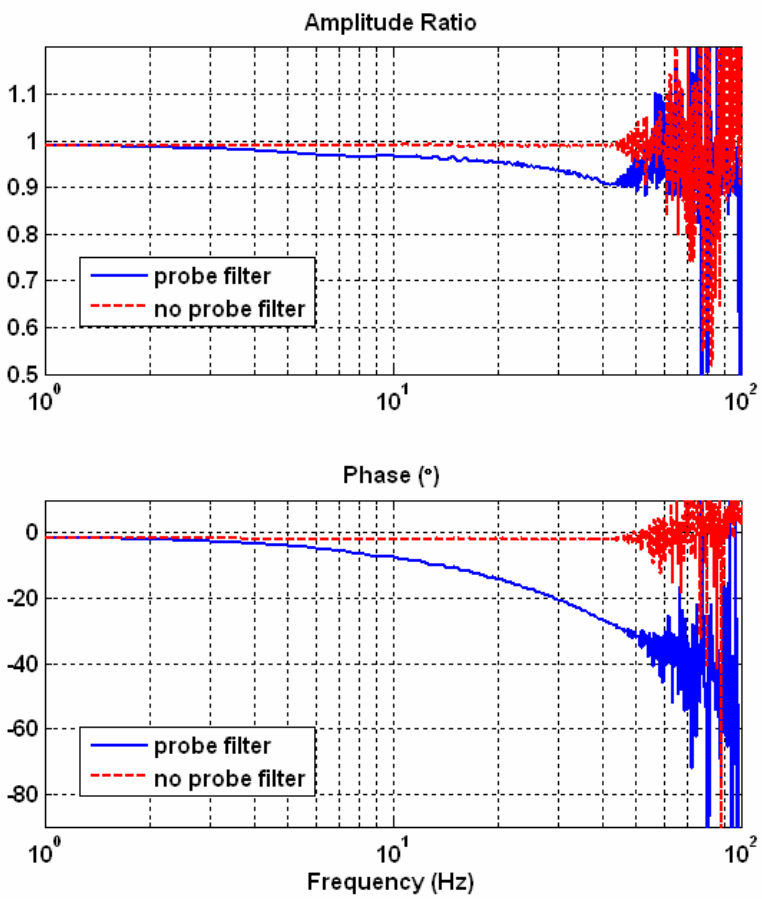

Figure 6. Probe transfer function derived from measurement data with and without probe filter.

7.6 CONCLUSIONS

A ring gauge artifact with cylindrical and cylindrical with swept sine wave features has been designed and fabricated.

- Error of the ± 5 µm amplitude features is 300 nm PV and the ring is round to 120 nm PV with a surface roughness of 37 nm RMS. The swept sine wave contains spatial frequencies on the OD from 6.384 mm to 0.383 mm corresponding to 1.6 to 27 Hz at 1 rpm.
- Changing the transfer function of an air-bearing cap probe was used to demonstrate the effectiveness of the swept sine wave to measure dynamic performance.
- Algorithms were developed to extract the dynamics of the probe from the swept wave measurement. Dynamic errors change the shape and add uncertainty to the result.
- Probe dynamic response from the ring gauge measurement will allow a CMM operator to devise a measurement strategy to limit dynamic errors to a specified range.

8 METROLOGY OF THREE MIRROR CONIC OPTICAL SYSTEMS

Robert Woodside, Jr.
Graduate Student
Thomas Dow
Professor
Department of Mechanical and Aerospace Engineering

8.1 INTRODUCTION

Three mirror anistigmat optical systems can almost eliminate low order aberrations. They also allow for a more compact and lightweight optical system. However, three mirror anistigmats utilize off-axis conic mirrors and unique assembly relationships that require high tolerance fiducial features. These qualities make increase the measurement complexity over a comparable two mirror system. Measuring the off-axis conics and the assembled optical system involves unique setups of a Fizeau interferometer; for example, the Zygo GPI. Off-axis conics add a degree of freedom to interferometric measurements as opposed to a rotationally symmetric conic. These mirrors must either be measured off-axis with an on-axis secondary reference element, or vice versa. Typical three mirror system setups place the detector on the same face as the system aperture which complicates the standard dual-pass measurement.

8.2 MEASURING OPTICAL SURFACES

Off-axis conics provide new challenges for optical metrology. On-axis rotationally symmetric conics can be measured using known techniques. Some of these techniques can be modified for use on off-axis conics. On-axis hyperboloids can be measured in a dual-pass setup on a Fizeau-type interferometer, such as the Zygo GPI, by using intermediary reference elements, as shown in Figure 1 a) and b) [1].

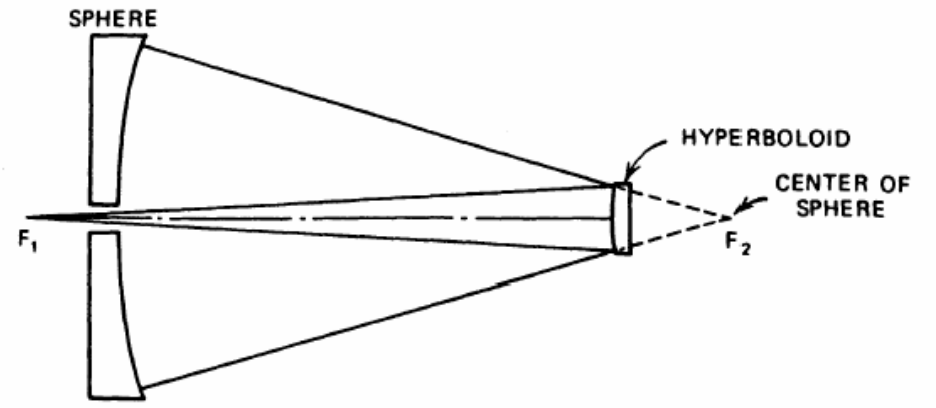

a) Hindle Test for Measuring Convex Hyperboloid Optics

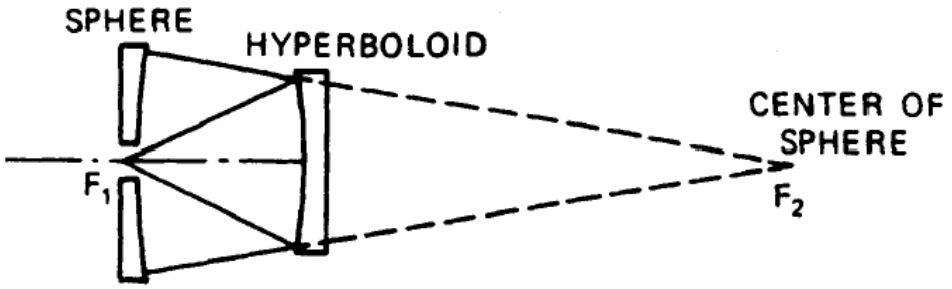

b) Silvertooth Test for Measuring Concave Hyperboloid Mirrors

Figure 1. Common Setups for Measuring Hyperboloid Mirrors

This process can be modified for off-axis hyperboloids by either moving the measured element off-axis or moving the secondary reference element off-axis. Each of these measurements require a more difficult location alignment than in the Hindle and Silvertooth tests and an added clocking alignment since the optic is not rotationally symmetric about the center of its aperture. Fiducial surfaces will need to be utilized to ensure proper orientation on the interferometer. Moving the hyperboloid off-axis, as shown in Figure 2, requires the focal point of the Zygo spherical reference lens to coincide with the front focus, f1, of the full hyperbola and the focal point of the secondary spherical mirror must coincide with the rear focus, f2, of the full hyperbola. Because all of these foci are on-axis, the setup only requires properly aligning the hyperboloid mirror. However, measuring the optic in this setup uses only a small portion of the interferometer's aperture reducing the horizontal resolution of the measurement. This setup would not use all of the available pixels to view the surface.

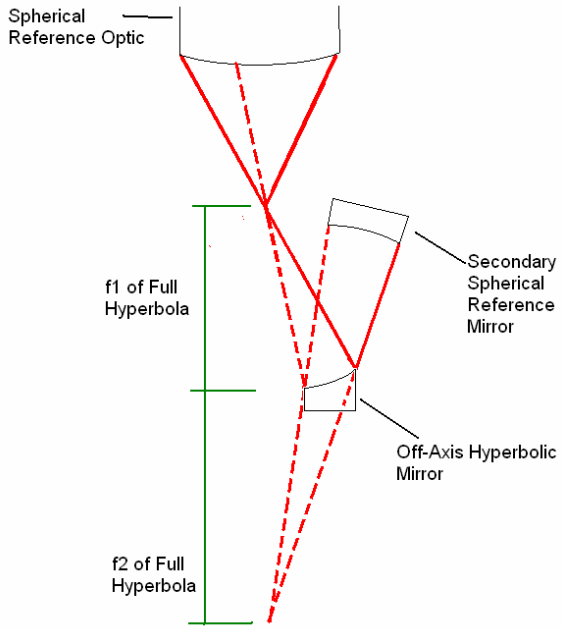

Figure 2. Off-Axis Hyperbolic Mirror Interferometer Setup with Off-Axis Measurement 1

Moving the secondary reference element off-axis is a more difficult setup but allows for the use of the interferometer's full aperture. There are two possible setups which can be used depending on the available optical elements and range of travel. In the first setup, shown in Figure 3, the focus of the spherical reference optic must coincide with the rear focus, f2, of the full hyperbola while the secondary spherical mirror's focus must be coincident with the front focus, f1. The secondary reference element in this setup can be either a precision bearing ball, shown in Figure 3-a, or a spherical mirror, shown in Figure 3 (b). A precision ball has the advantage of being compatible for any off-axis hyperbola measured in this setup. If the center of the ball and the front focus of the hyperbola coincide, then the radius of the ball is arbitrary. However, a spherical mirror must be designed for a specific off-axis hyperbola to have the correct f-# and must still be aligned so that its focus coincides with the front focus of the hyperbola. The advantages of this setup are that the area of measurement is more compact and that a precision ball can be used in place of a large mirror. However, in many cases the long focal length of the spherical reference optic needed for the setup is prohibitive. Also, a special mount would have to be designed for the hyperbolic mirror to align it with respect to the primary reference element.

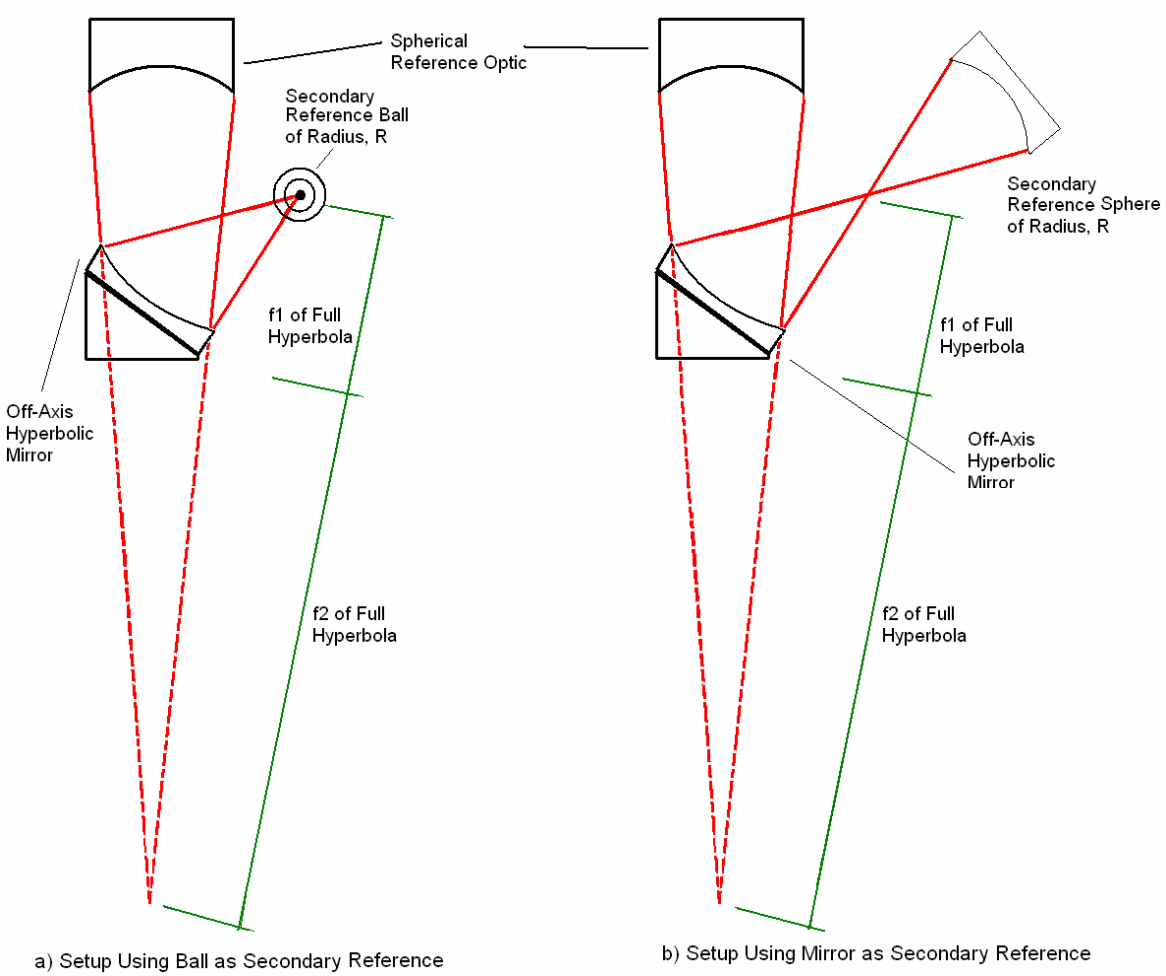

Figure 3. Off-Axis Hyperbolic Mirror Interferometer Setup with On-Axis Measurement 1

To reduce the focal length of the primary spherical reference, a second setup, shown in Figure 4, reverses the focus pairing. It pairs the Zygo reference lens with the front focus and the secondary reference mirror with the rear focus. This setup is more likely to be compatible with an available Zygo reference lens but requires much more vertical space and a secondary reference at least as large in aperture as the hyperboloid. The secondary sphere must have a large aperture and a long focal length to account for the light spread from the hyperbola and the large distance to the rear focus, respectively. This mirror would have to be custom made for each individual hyperbolic mirror.

An advantage of this setup is the possibility of using the flats on the mirror's fiducial surface to obtain the correct tilt by using a planar reference element. The user could level the fiducial flats by viewing their interference with a planar reference lens. If the flats are not part of a continuous surface, they would need to be checked on a CMM to ensure that they are coplanar. Each pad would have to probed with more than three points so that a plane will be established. Then, it

can be determined if the plane of each pad is coplanar with the other two. Placing the hyperboloid on-axis allows for the full use of the interferometer, however, it involves a much more difficult alignment process. When the hyperboloid is on-axis, the Zygo reference lens, hyperboloid mirror and secondary reference mirror do not share a common optical axis. Aligning the hyperboloid will be as difficult as in the off-axis setup. The alignment of the secondary mirror with the measured optic will be much more difficult as the mirror must be placed beyond the range of the GPI three rod part mounting stage yet must still be precisely translated. This requires an alignment method on the GPI.

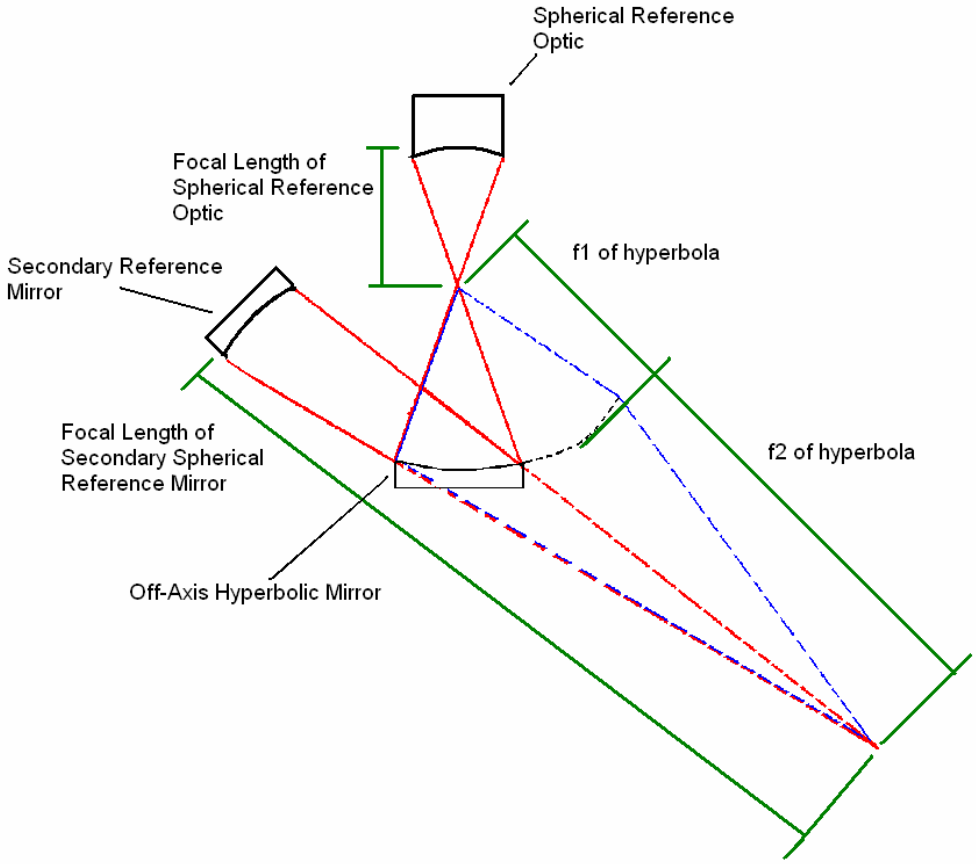

Figure 4. Off-Axis Hyperbolic Mirror Interferometer Setup with On-Axis Measurement 2

A technique that could allow for on-axis measurements and ensure proper alignment is the use of computer generated holograms (CGH) in the GPI. A CGH puts out a wavefront that matches the theoretical shape of the measured element so that it can be analyzed in a single-pass setup. A CGH could be developed that matches both the mirror's optical surface and its fiducial elements. If the outer edges of the CGH match the fiducial surfaces and the inner portion matches the optical surface, the measurement would need no other reference lens. This would allow the CGH to assist in aligning the optic, measure the optical surface and determine if the relationship

between the fiducial and optical surfaces is correct. However, this method is prohibitive based on the need to have a different CGH for every unique off-axis conic mirror.

8.3 OPTICAL SYSTEM PERFORMANCE

The process to measure an off-axis conic three mirror system would be much the same as the process to measure a rotationally symmetric on-axis two mirror system. To measure wavefront error and MTF, the system can be placed on the Zygo GPI, or any Fizeau interferometer, using one of the two setups shown in Figure 5. In the first setup, shown in 5a), collimated light would be sent in through the system collection aperture and a ball or spherical mirror would be placed so that the center of the ball or focus of the spherical mirror coincides with the focus location of the optical system. The ball or mirror must also have an *f/#* greater than or equal to that of the system. This would send the light back through the system and give twice the wavefront error of the system at the interferometer. The second setup, shown in 5b), is similar but a spherical wavefront with an *f/#* less than or, preferably, equal to the *f/#* of the system would be sent through the detector aperture and a flat mirror would be placed at the collection aperture.

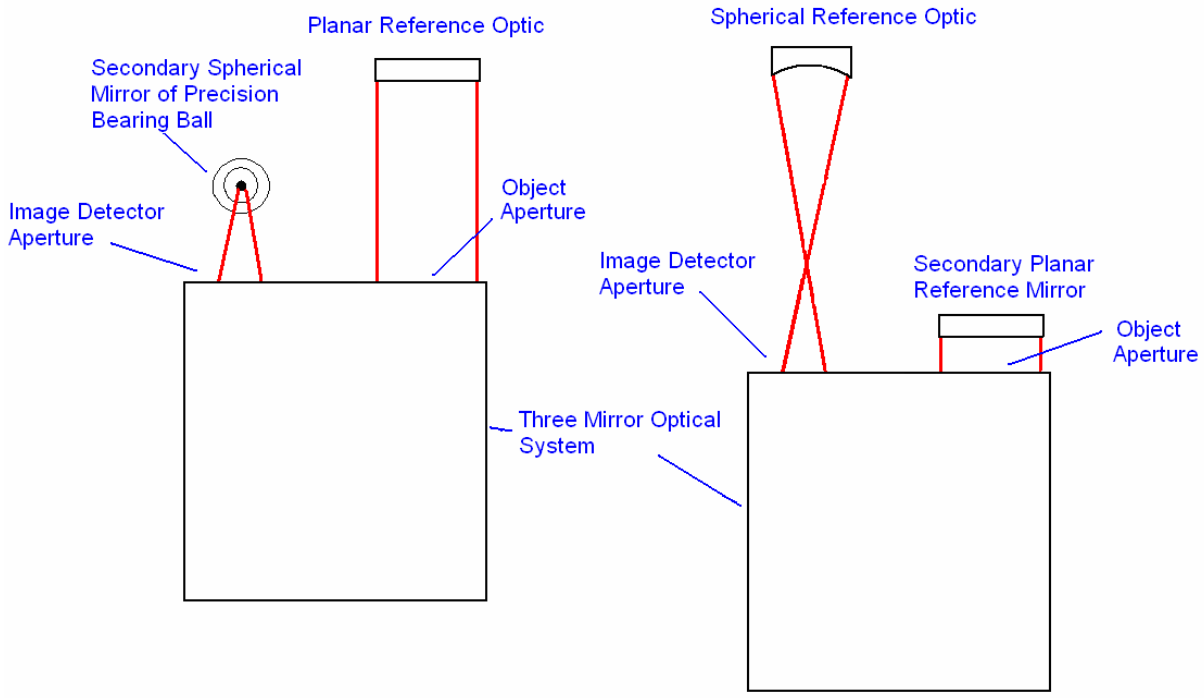

a) Planar Primary, Spherical Secondary b) Spherical Primary, Planar Secondary

Figure 5. Interferometer Setups for Optical System Measurement

The second setup involves easier alignment. The secondary reference element alignment would be the most difficult process of each setup. In the case of Setup 2, the secondary planar element

only needs to be adjusted for tip/tilt whereas the ball or spherical mirror must be adjusted in x, y and z. However, Setup 2 also requires a primary reference sphere with an *f/#* close to that of the system so that a large percentage of the interferometer's aperture and the system's full aperture are included in the measurement. In this manner, Setup 2 may require a different primary reference element for each different system whereas Setup 1, if the ball is used for the secondary reference, would have interchangeable components regardless of the system being measured.

Each of these setups would output wavefront error and MTF data and allows measurement with off-axis rays. The process for measuring off-axis rays in Setup 2 would be easier than that of Setup 1 because the only necessary adjustment would be to tilt the flat and translate the system. Conversely, producing off-axis rays in Setup 1 requires tilting and translating the system as well as translating the secondary spherical reference.

Deviation from a null fringe pattern indicates the wavefront error in the system. This wavefront error will be compared to the expected wavefront error for the designed system produced by Code V. The Zygo GPI also has the ability to determine MTF values from the wavefront error measurements. These values will be compared against expected values from Code V. Code V produces on-axis rays as well as off-axis rays and generates wavefront error, MTF and spot size plots at each of these locations. The off-axis simulations will be compared to those produced by the actual system.

8.4 CONCLUSIONS

Measuring off-axis conic systems and their components require complex, yet feasible, interferometry setups. The best setup to measure the individual off-axis conic optical surfaces is the on-axis setup 2, shown in Figure 4. This setup allows Zygo primary reference optics to be used and the conic mirror can be placed flat on the measuring surface. A secondary reference sphere would have to be custom made, however, the process for fabricating and measuring spheres is much less susceptible to error than the process for off-axis conics. For most systems, a setup with a spherical primary reference optic and a planar secondary optic would be the most feasible option. The planar reference alignment step would be minor compared to the alignment necessary with a reference sphere.

The shape of conic mirrors and configuration of three-mirror anistigmats can each vary greatly depending on the application. For this reason, the user would have to evaluate the advantages and disadvantages of each setup for the optical surface or system in question.

REFERENCES

1. Malacara, Daniel, “Optical Shop Testing”, John Wiley & Sons, 2nd Edition, New York, 1992.

9 HIGH PRESSURE PHASE TRANSFORMATION OF SILICON

Timothy Kennedy
Graduate Student
Ron Scattergood
Professor
Department of Materials Science and Engineering

9.1 INTRODUCTION

Diamond cubic silicon (Si-I) is a brittle material under standard temperature and pressure, but when exposed to a high pressure environment the crystal structure transforms into a ductile β-Sn metallic phase (Si-II). Once the Si-II is unconstrained it back transforms into multiple forms of Si. The transformation schedule of silicon depends on loading, unloading, and temperature, Figure 1. This transformation allows silicon to be machined without brittle fracture occurring, but the back transformation alters the subsurface (5 nm to 400 nm in depth). This alteration can be divided into two layers: an amorphous layer and a damage layer. The amorphous layer extends from the surface down as far as 100 nm; this is the byproduct of the back transformation process which creates amorphous silicon (a-Si). Below the amorphous layer a damage layer extends another 400 nm; this layer is comprised of dislocation structures. Recently it has been shown through transmission electron microscopy (TEM) that depending on the machining technique and other parameters the damage layer can be eliminated.

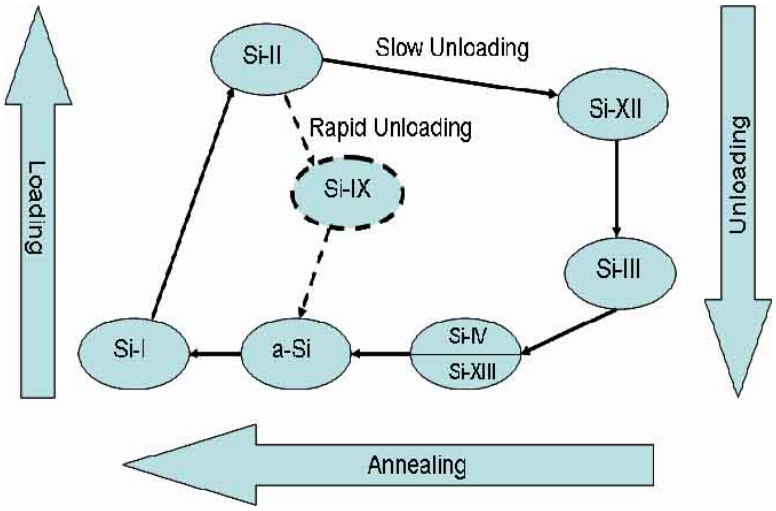

Figure 1. Silicon transformation schedule.

9.2 SILICON SAMPLE PREPERATION

Starting with an as received (100) oriented silicon wafer that had been chemically mechanically polished (CMP), a 10 mm by 20 mm rectangle is cut out of the wafer so that the <110> type direction is along the 10 mm width. Different crystal orientations are available but it has been shown that (100) oriented silicon along the <110> directions provides the best ductility. The tools used were 3 mm round nose diamond with -30° and -45° rake angles, from two different vendors (IMT and Edge Tech). Samples are machined using a traditional t-lathe setup and a parallel fly cutting setup. Only the fly cutting used both vendors' tools, and it is important to note that when the samples were fly cut that all the tools were freshly sharpened.

9.3 TEM RESULTS

9.3.1 T-LATHE SET UP

Previous TEM results from t-lathe machining showed the existence of a damage layer below the a-Si layer. Lathe machined samples used an IMT tools at 1 µm/rev and 5 µm/rev. Figure 2 was machined at 5 µm/rev and is a representation of lathe machined silicon with IMT tools showing dislocations and slip planes.

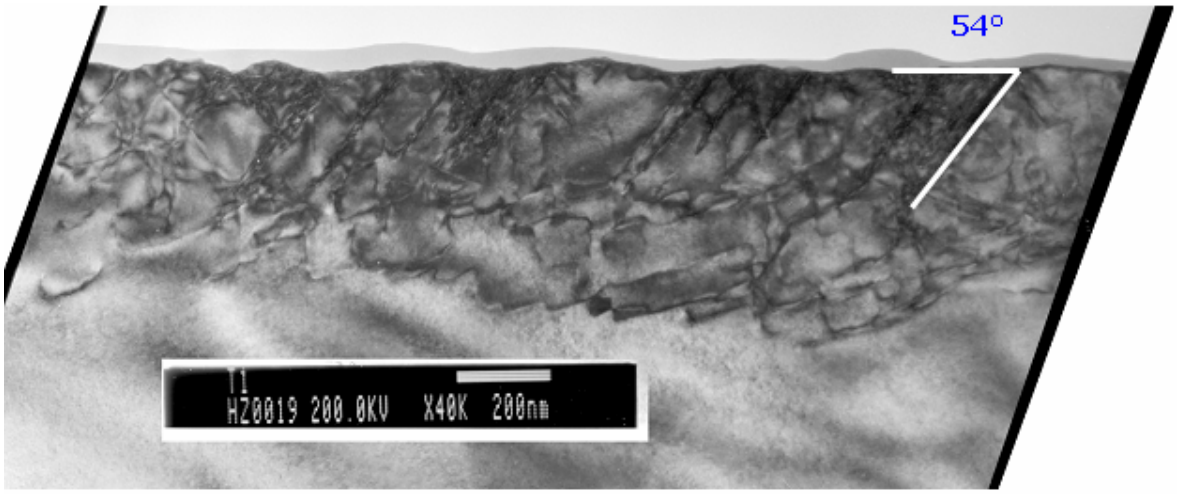

Figure 2. TEM micrograph at 5 µm/rev with an IMT -30° tool. The (111) slip system angle is shown along with the a-Si layer and the dislocation microstructure.

9.3.2 FLY CUTTING SET UP

When the machining technique is switched to parallel fly cutting a change in the subsurface was evident. Figures 3 and 4 were fly cut at 5 μm/rev with an IMT -30° tool, and there is no damage layer beneath the a-Si layer when compared to Figure 2. Even the a-Si layer is dramatically thinner than previously measured. When the tool vendor is changed to Edge Tech the same microstructure is seen. Figures 5 and 6 were fly cut at 5 μm/rev with an Edge Tech -30° tool, and the same lack of dislocations and a thin a-Si layer is apparent.

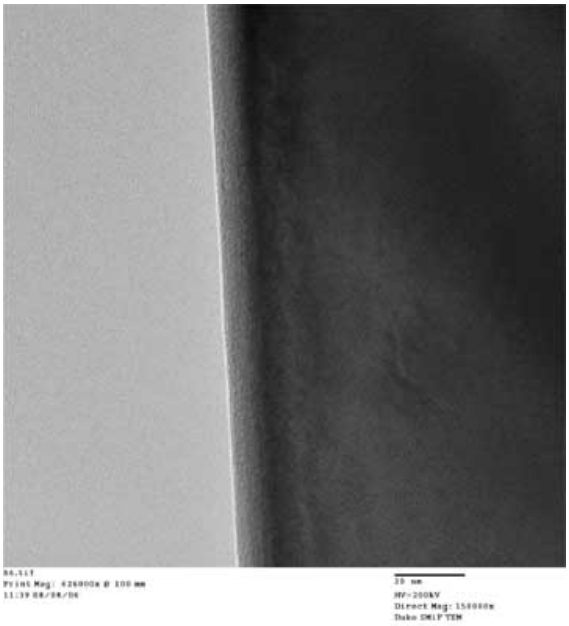

Figure 3. TEM micrograph fly cut at 5 μm/rev with an IMT -30° tool. Notice the lack of a damage layer.

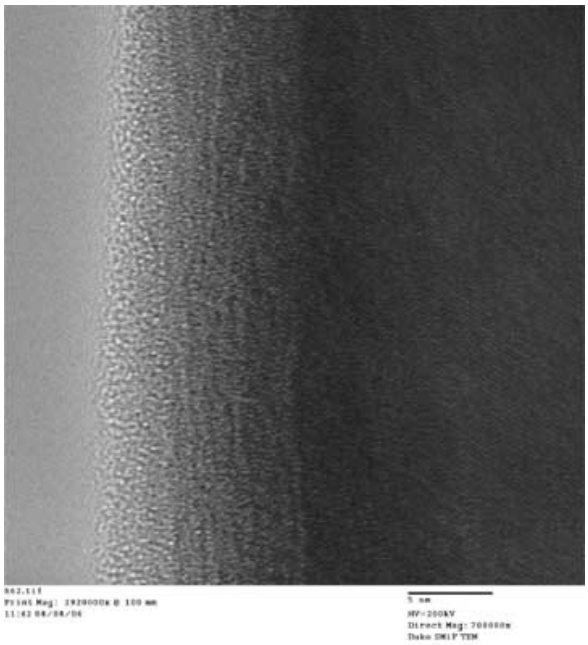

Figure 4. TEM micrograph fly cut at 5 μm/rev with an IMT -30° tool showing a higher magnification of the a-Si layer at the surface.

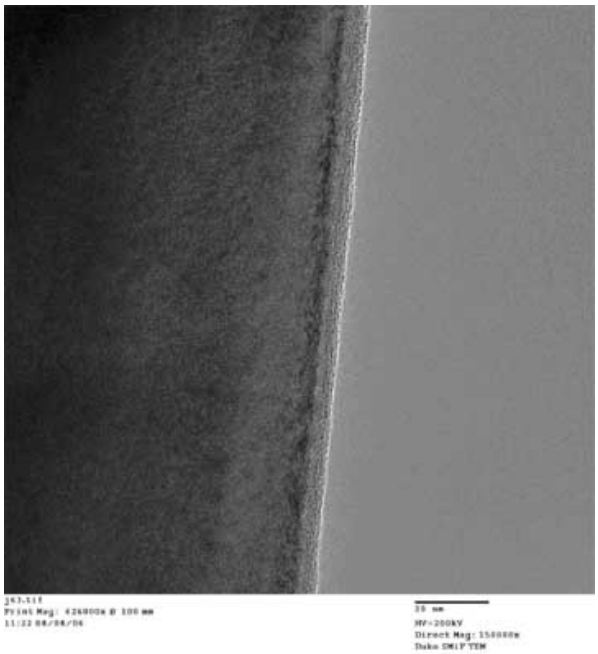

Figure 5. TEM micrograph fly cut at 5 μm/rev with an Edge Tech -30° tool. Notice the lack of a damage layer.

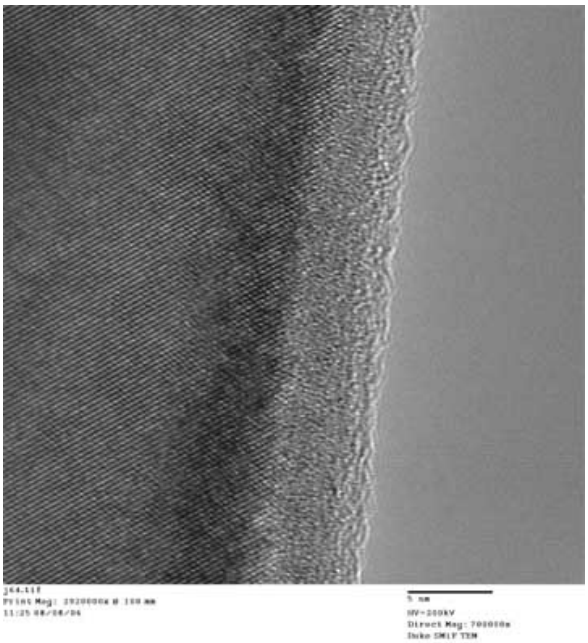

Figure 6. TEM micrograph fly cut at 5 μm/rev with an Edge Tech -30° tool showing a higher magnification of the a-Si layer at the surface.

When the feed rate is lowered to 1 μm/rev with an Edge Tech -30° tool nanocrystals appear below the a-Si layer, Figure 7.

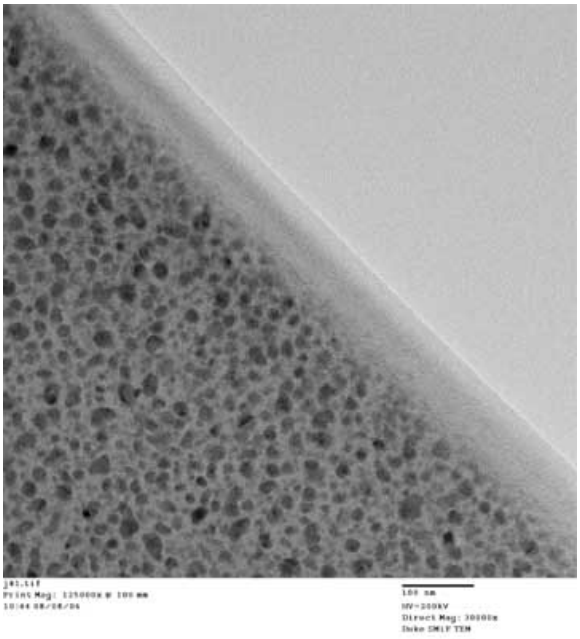

Figure 7. TEM micrograph fly cut at 1 μm/rev with an Edge Tech -30° tool. Notice the existence of nanocrystals.

It is unclear how these nanocrystals were formed in the sample, since the same piece of silicon was used for the 5 μm/rev samples shown in Figures 5 and 6. As of now it is believed to be an anomaly. But if more samples at this cutting condition, both with the Edge Tech and/or IMT tool, show this phenomena then it will need further study.

9.4 MACHING TECHNIQUE COMPARISON

Beyond comparing t-lathe machining and fly cutting it is important to compare these results with the results found from CMP processing. It is interesting to compare these new TEM results to the as received CMP silicon wafer in Figure 8, which shows a nominal a-Si layer thickness of around 2 nm. It was previously thought that CMP was the only way to achieve optical surface finish with very little subsurface damage, but that has been proven not to be the case.

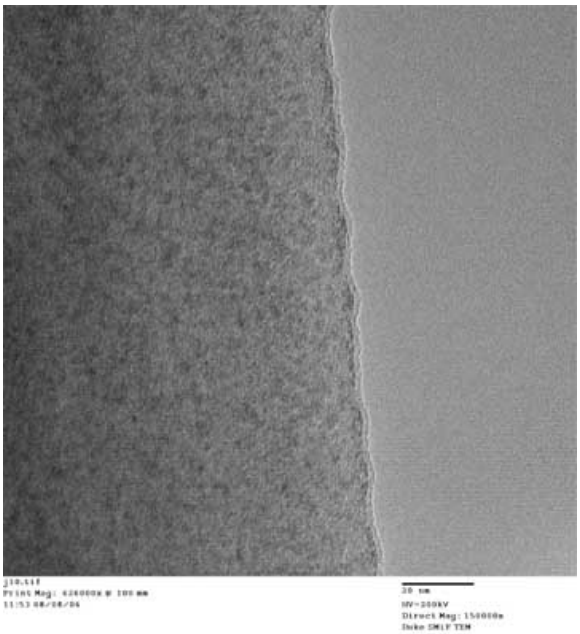

Figure 8. TEM micrograph of as received CMP polished silicon wafer.

Figure 9 shows the comparison of a-Si layer depth versus the machining feed rate and technique. Due to the fact that lathe machining and fly cutting are equivalent machining techniques, the only comparison that can be made is that tool sharpness is the contributing factor to the change in a-Si layer depth.

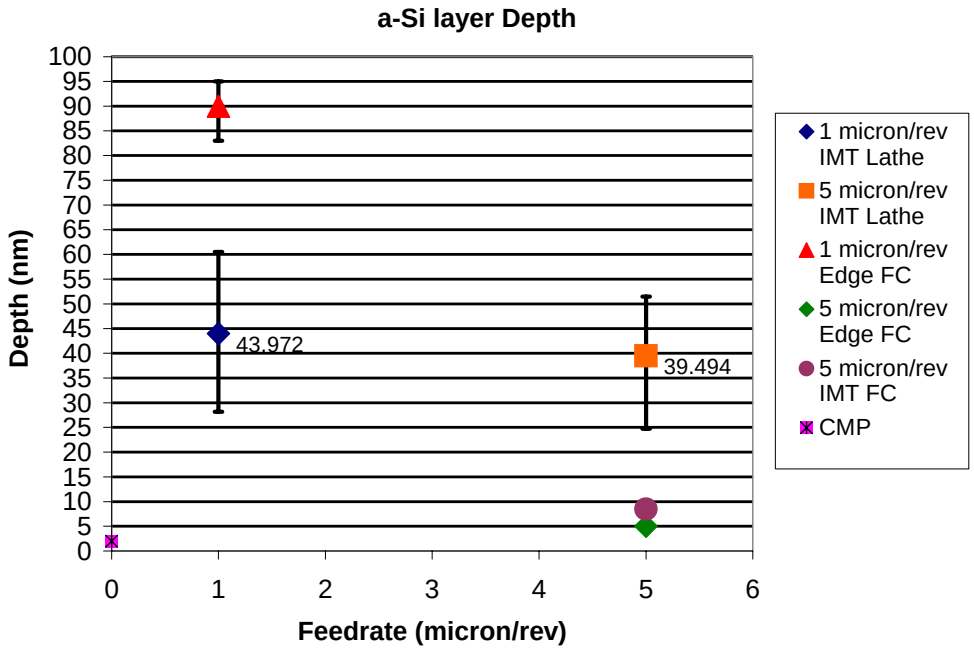

Figure 9. TEM micrograph fly cut at 5 μm/rev with an Edge Tech -30° tool. Notice the lack of a damage layer.

9.5 CONCLUSIONS AND FUTURE WORK

It is highly unlikely that there is enough of a difference in machining techniques to produce the results in Figure 9. Since the samples that were t-lathe machined were done so with "dull" IMT tools, and the samples that were fly cut were machined with newly sharpened IMT and Edge Tech tools it seems that as of now tool sharpness plays a critical roll in the production of subsurface structures in machined silicon.

These new results also help to understand the deformation mechanism in machined silicon. There had been some doubt to whether a high pressure phase transformation (HPPT) occurred in the t-lathe machined samples due to the size of the damage layer. But using sharp tools and fly cutting it appears that an HPPT did occur due to the lack of a damage layer and the uniformity of the back transformed a-Si layer.

More TEM samples need to be made and viewed to complete the graph in Figure 9. It is also important to pay close attention to the lower feed rate to see if the nanocrystals seen were an anomaly or if the machining actually was able produced the nanocrystals.

This page intentionally left blank.

10 MODULE-TO-MODULE PARTS TRANSFER USING NON-CONTACT ACOUSTIC LEVITATION

Yanbo Yin
Graduate student
Paul Ro
Professor
Department of Mechanical and Aerospace Engineering

10.1 INTRODUCTION

In this paper, a long-distance contact-less transfer of light and flat objects using Near-Field Acoustic Levitation (NFAL) is addressed. The transfer device utilizes acoustic levitation generated from a vibrating beam actuated by a set of piezo-electric drives. Each drive module contains a straight beam driven by two PZT actuators at the ultrasonic resonant frequency of the actuators. When a light and flat object is put on the vibrating beam, the acoustic pressure lifts and carries the object in the direction of the traveling waves generated on the beam. This kind of system can be used to transfer various precision products such as silicon wafer, compact disc and liquid crystal devices (LCD). These products must be protected from contamination and scratches during handling and processing. In case of long-distance transfer, two or more modules can be connected in series. Though the long module is possible to realize the transportation, the length of each module is limited in practice to about two feet due to power consumption and other manufacturing limitation.

When an object moves from one module to another module, the gap between the two beams becomes a main design issue that involves the size of the floating plate, the vibration mode, and the levitation force. In this paper, the gap is analyzed using Comsol-Finite Element Method software to investigate the velocity and the pressure distributions. Also, an experiment is set up to investigate the transportation performance in and around the gap area. It is observed that there is a velocity threshold, above which the motion of the object is smooth.

10.2 THEORETICAL ANALYSIS ON THE GAP

Based on the fluid dynamics, the dynamic performance of the air in the gap is analyzed. The contour plot of the velocity is shown in Figure 1. The gap position is defined in the middle of the fluid. The legend on the right of the plot demonstrates the fluid velocity distribution. In this case the fluid bottom boundary condition is applied with the traveling waves of a flexural beam. The figure shows the x-velocity plot at time =3.8e-5. One can see that the x-velocity in the gap has smaller value than those above the beam.

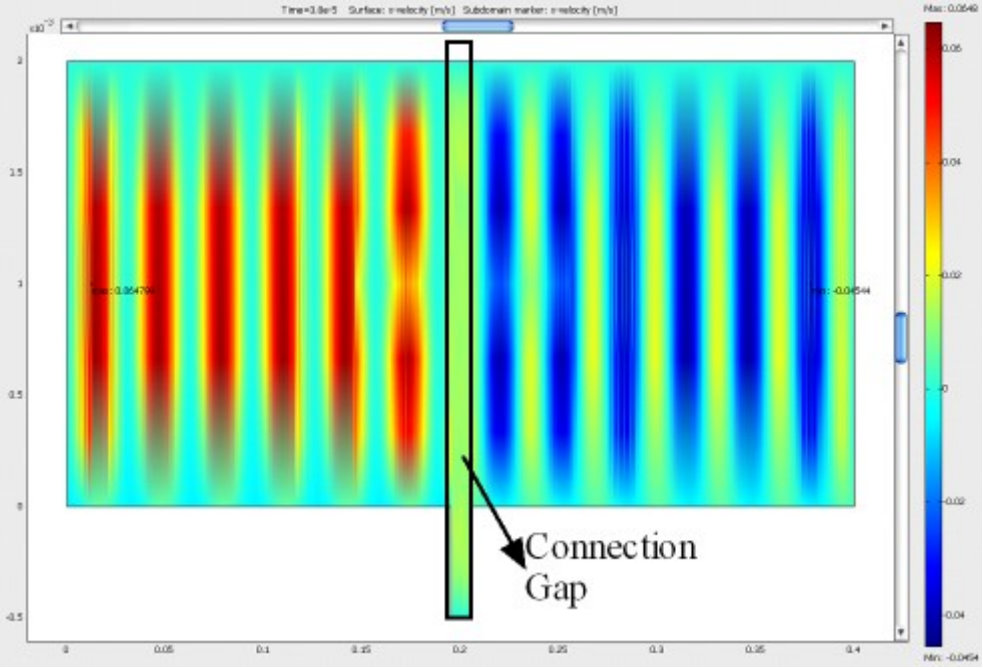

Figure 1. The simulation result

Figure 2 shows the line plot of x-velocity distribution in the gap and on the beam, respectively. The maximum velocity in the gap is only 0.014m/s while on the top of the beam is 0.07m/s.

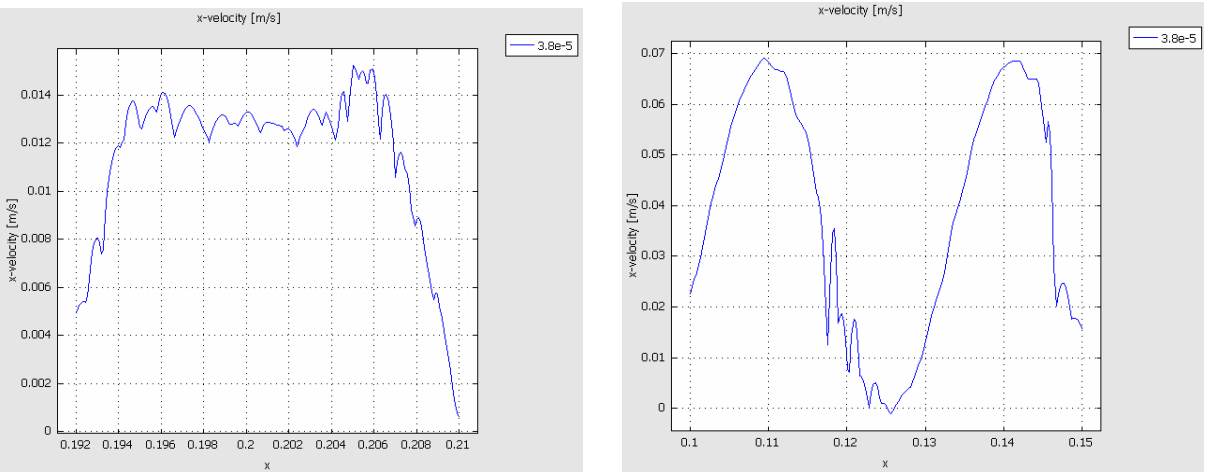

(a) in the gap (b) on the beam

Figure 2. The x-velocity distribution along x-direction at time=3.8e-5s

Figure 3 shows the maximum x-velocity for various gap sizes when the vibration amplitude is 3 micrometers. The plot shows that the maximum x-velocity is achieved at 5mm gap. But, this value is still small, compared to the maximum x-velocity elsewhere on the beam.

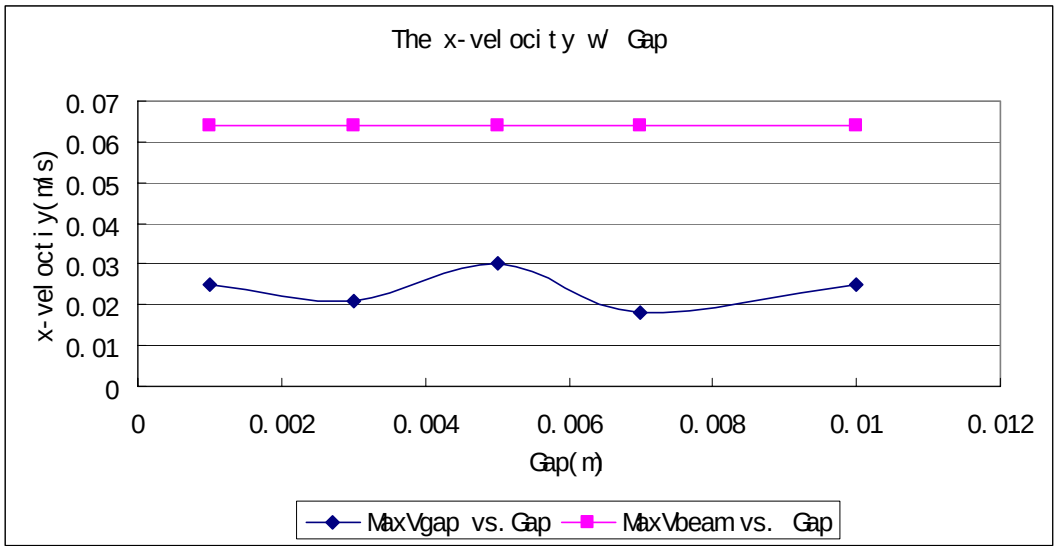

Figure 3. The x-velocity vs. Gap

Figure 4 shows the maximum velocity with respect to the gap size at different vibration amplitudes. It can be seen that the maximum velocity is constant at 0.005 m for all three amplitudes. So, empirically, the optimal gap between two adjacent modules would be 0.005 m.

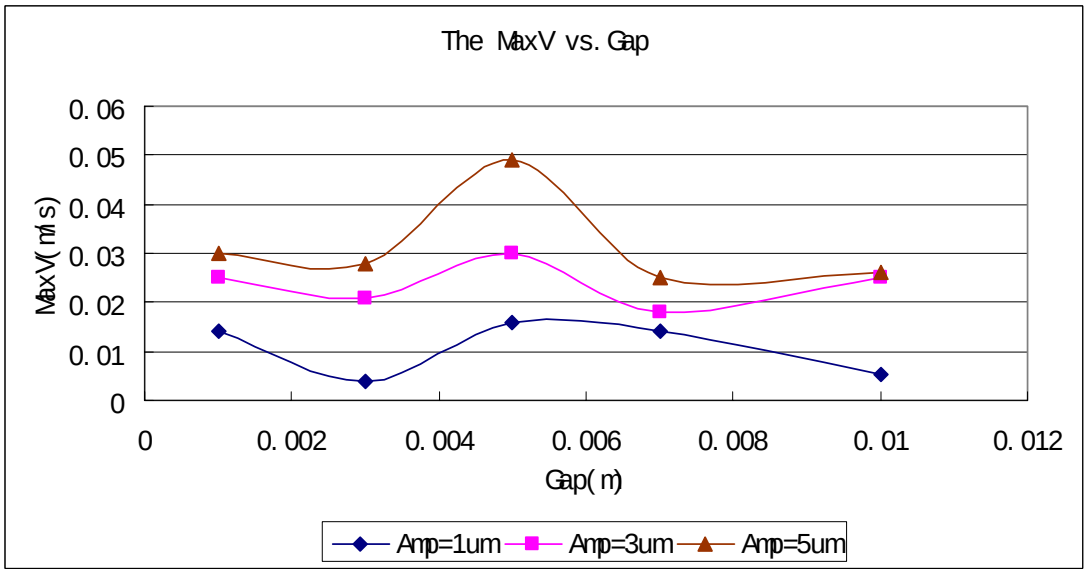

Figure 4. The maximum velocity vs. Gap and vibration amplitude

Figure 5 shows the relationship between the maximum velocity and vibration amplitude at the optimum gap size of 0.005 meters. When the beam vibration amplitude increases, the max velocity in the gap increases linearly.

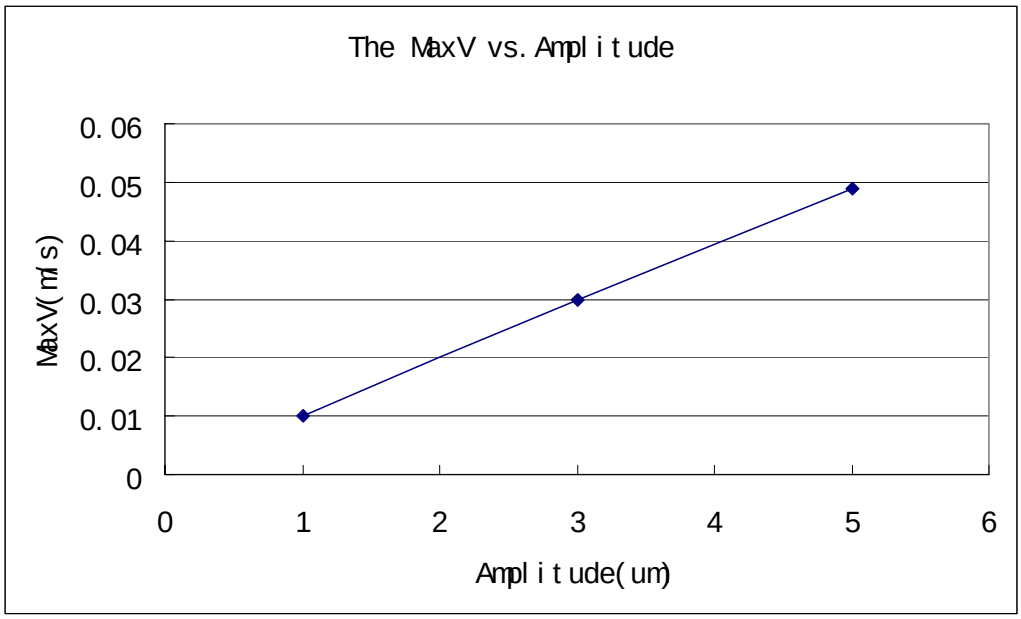

Figure 5. The maximum velocity vs. amplitude

10.3 EXPERIMENT SETUP

The schematic of the experiment setup is shown in Figure 6. Two modules are serially aligned along the same direction as shown in (a). Each transportation system consists of one Aluminum beam, two Langevin type Transducers (BLT), and two mechanical horns. Each drive is power by a Trek PZD350 amplifier. A video camera is placed directly above the gap (as shown in (b)) to capture the motion above the gap. The measured area is between the two actuators where the gap lies in the middle of the range. The resolution of the video camera is 0.0004 m/pixel, and the speed is 30fps.

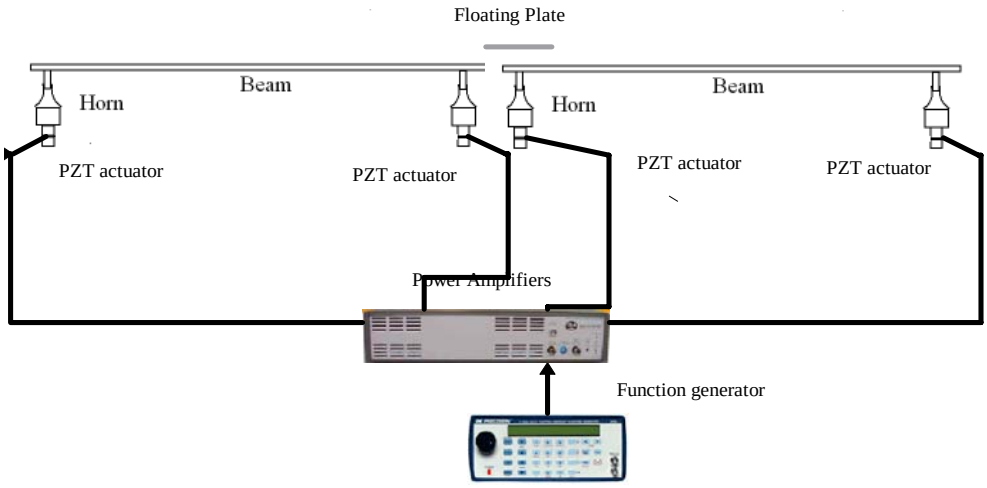

(a) The experiment setup

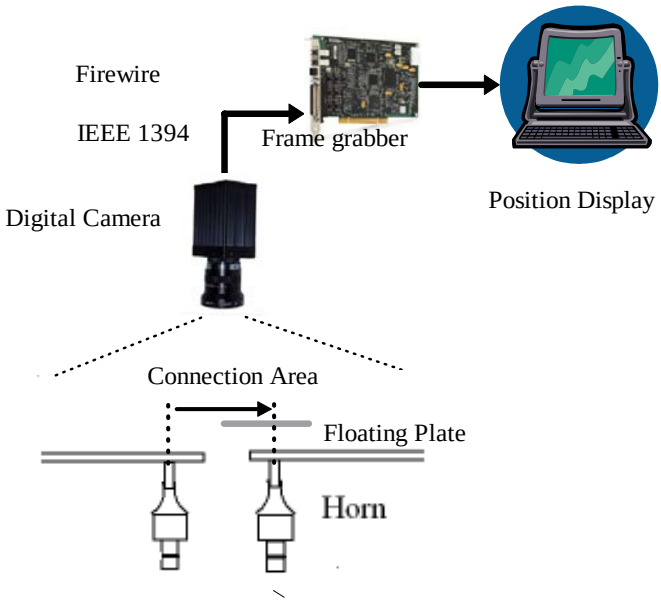

(b) The connection area measurement

Figure 6. The M2M Transportation systems

The captured video is processed in Labview to derive the position and velocity of the moving plate. To facilitate the video tracking and capture, the plate is marked with a circular dot which can be recognized by Labview. The image from the video is firstly cropped to a small region where only the interested area is kept. Figure 7 shows this process where the bright area is kept and other is cropped.

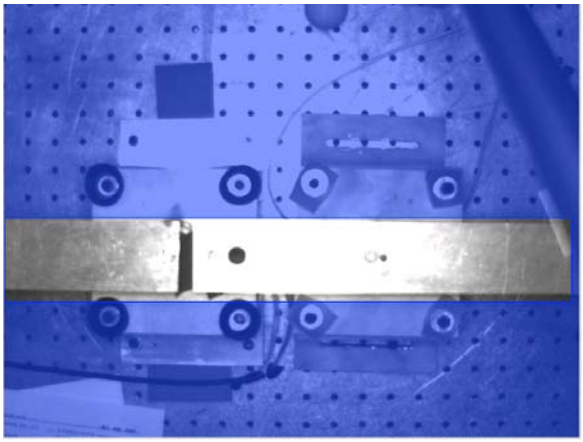

Figure 7. Image crop

After cropping, the image is then processed by adjusting the quality. The brightness, contrast, and the Gamma gain are set to be 167, 55.5 and 0.63, respectively. After this step, there is only one circular black dot in the image. The black dot is then be detected by Labview to get the position in the unit of pixels. Figure 8 shows the parameter setup and the derived data from this procedure. The marked dot is positioned in the image, and the parameter of the circle is expressed as radius, center X and center Y position.

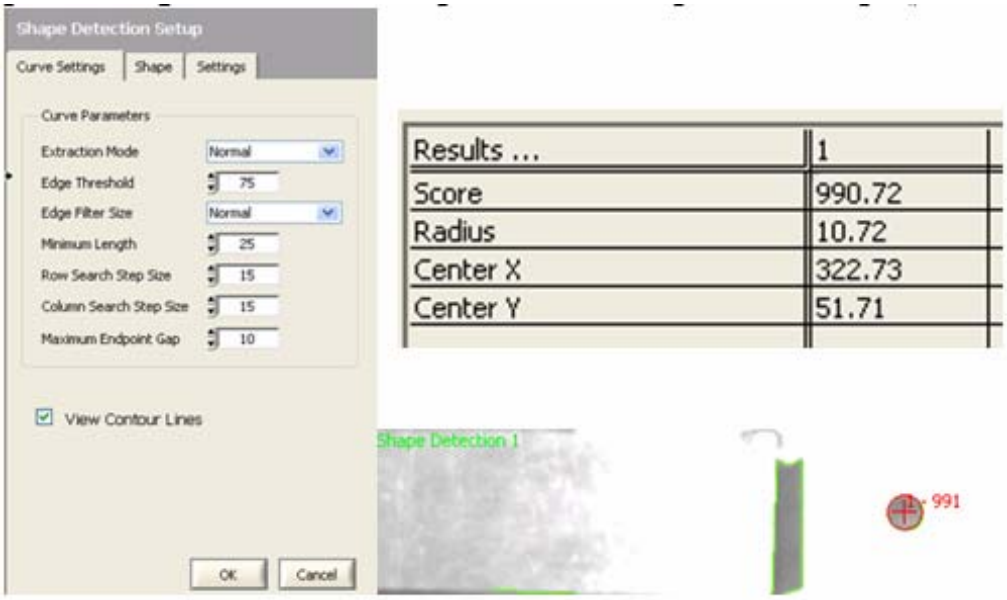

Figure 8. The position derivation

10.4 THE EXPERIMENT RESULTS

The transportation performance in the gap is investigated. Three plates with different size are used in this experiment. Figure 9 shows a series of position and velocity plots where the gap is set to be 0.5mm. The size of the plate is 24.8×24.8mm. In Figure 9(a), the area between the dashed lines is the connection area. The position curves which pass through the dashed area show the smooth motion through the connection area, while those that stop in the dashed area represent the cases that could not pass the area. Figure 9(b) is the corresponding velocity plot where the velocity threshold under such condition can be found to be 0.15 m/s.

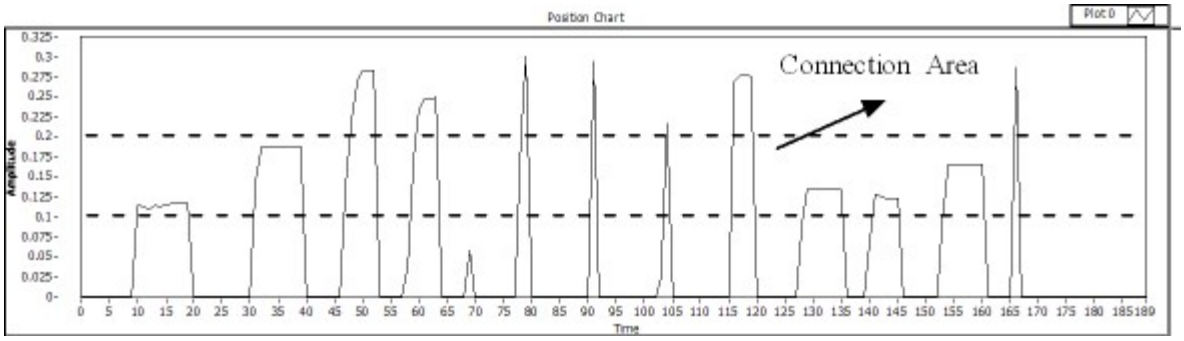

(a) Position vs. time

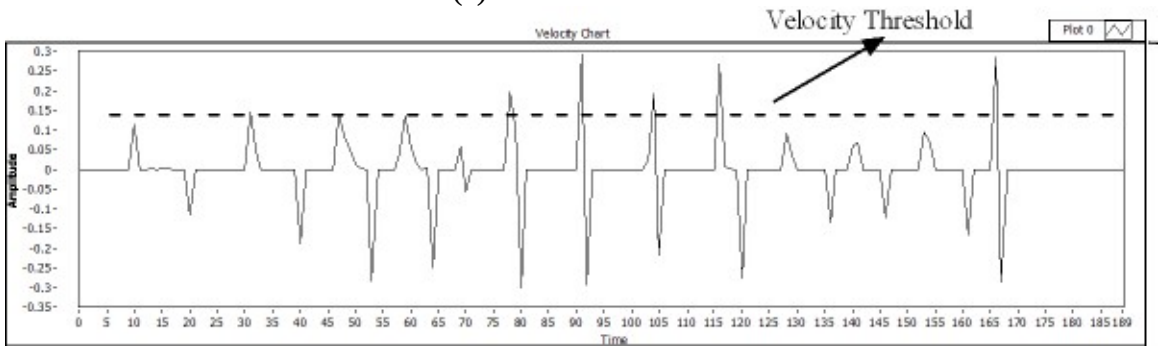

(b) Velocity vs. time

Figure 9. The Speed distribution through the gap

Figure 10 shows three typical motions of the plate where the gap size is set to 15mm. the velocity threshold in this case is 0.09 m/s. When the speed of the plate is below the threshold, the plate will stop right at the connection position as shown by the first curve in the Figure. While the speed is above the threshold, the plate can move through the gap smoothly as in the third curve. When the speed of the plate is near the threshold, the speed will reduce a little and then continue to pass through the connection area as the second curve shows.

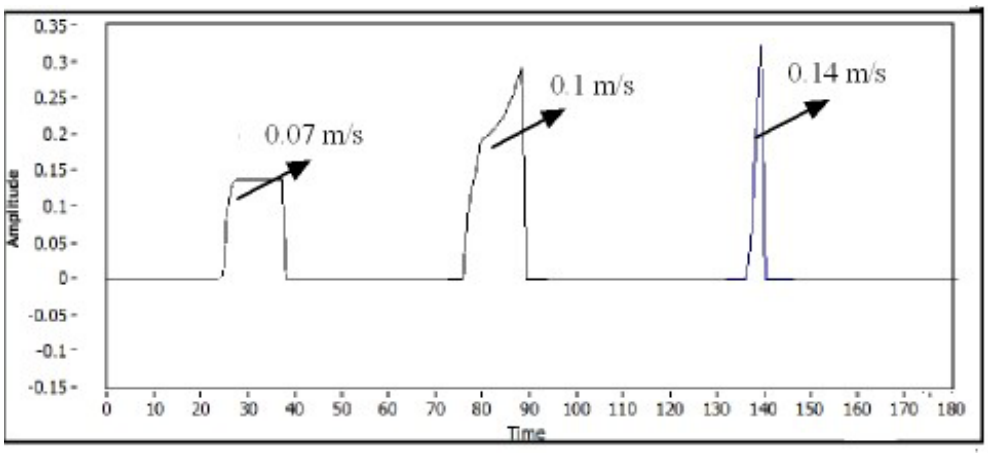

Figure 10. The motion of the plate

Figure 11 shows the speed threshold with different gap distance where the plate size is 32× 32mm. In Figure 11(a), when the gap size is smaller than 5mm, the speed threshold will rise to a relatively high rate as the gap size increases. In this case, the plate only has to overcome its momentum to continue travel on the beam. When the gap is larger than 5mm, the speed threshold will rise relatively slowly compared to the ones below 5mm. As the gap continues to grow, the size of the plate will become another issue that determines the threshold speed.

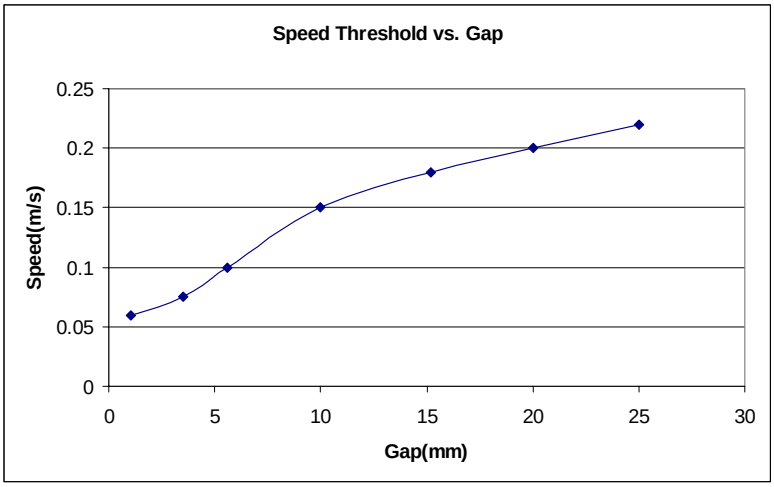

(a) Threshold for plate 32x32

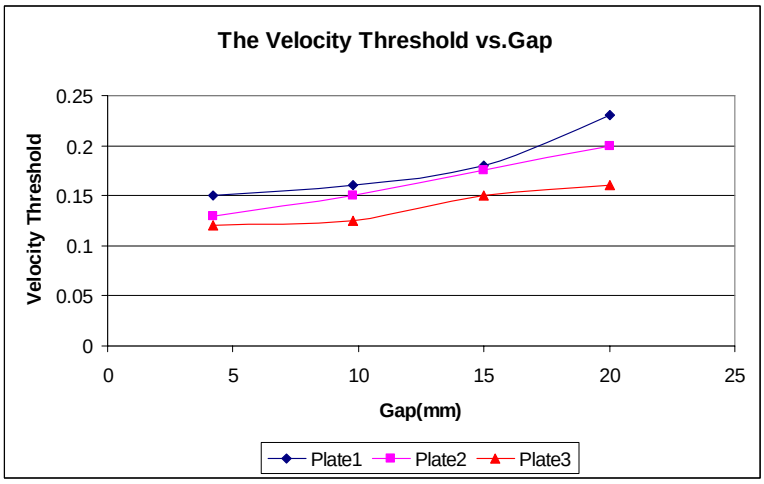

(b) Threshold with different plates

Figure 11. Speed threshold

The module-to-module (M2M) transportation performance also depends on the plate size. Table 1 is the speed threshold where the gap size is 5.6mm. When the plate size is small, it will require a larger speed to pass through the gap, while the larger plate requires smaller speed to pass it.

Table 1. Speed threshold

Plate No.	Plate size(mm × mm)	Speed threshold(m/s)
1	24.8×24.8	0.114
2	32×32	0.1
3	35×35	0.07

10.5 CONCLUSION

The feasibility of M2M transportation is investigated along with preliminary performances. It is shown that:

- A plate can pass through the gap smoothly above threshold speeds.
- The speed threshold is a function of the plate size, and the smaller the size, the larger speed required to pass through the gap.
- The optimum gap size is 0.005 m for different amplitudes.

A mathematical model will be developed to investigate various performance issues analytically.